QUANTITATIVE CHARACTERIZATION OF BILLOWED STRUCTURES

ALONG THE MARGINS OF BASALTIC INTRUSIONS TO DETERMINE PROCESS

AND TIMING OF FORMATION: CASE STUDIES FROM BIG BEND NATIONAL

PARK, TEXAS AND 71 GULCH, IDAHO

A THESIS IN
Environmental and Urban Geosciences

Presented to the Faculty of the University of
Missouri-Kansas City in partial fulfillment of
the requirements for the degree

MASTER OF SCIENCE

by
AARON JAMES GALLETLY
B.S., University of Missouri-Kansas City, 2017

Kansas City, Missouri
2021

QUANTITATIVE CHARACTERIZATION OF BILLOWED STRUCTURES

ALONG THE MARGINS OF BASALTIC INTRUSIONS TO DETERMINE PROCESS

AND TIMING OF FORMATION: CASE STUDIES FROM BIG BEND NATIONAL

PARK, TEXAS AND 71 GULCH, IDAHO

Aaron J. Galletly, Candidate for the Master of Science Degree

University of Missouri-Kansas City, 2021

ABSTRACT

By constraining the conditions in which billowed structures form, the conditions of explosive vs. non-explosive magma-water interaction can be further revealed, improving our understanding of how magma propagates and interacts with water in the subsurface. Billowed structures are likely formed at the arrival of the intrusion due to cooling of intruding magma while experiencing Kelvin-Helmholtz instabilities. Aligned plagioclase laths and stretched vesicles along margins are evidence that the formation of billowed structures occurred while the margins were fluid, deformable, and flowing. Linear billow crests in BBNP were commonly subvertical in orientation, while at the shallower system of 71 Gulch, no organization of billow orientations was observed. The inclusion of sedimentary particles in the glassy margins of the intrusion support the claim that the magma experienced Kelvin-Helmholtz instabilities, as external sediment was able to be transmitted through the magma-sediment interface and become incorporated into the magma.

Basaltic intrusions exhibiting unique billowed structures that record magma and water-bearing sediment interaction have been examined and reconstructed in three

dimensions using structure for motion (SfM) in Big Bend National Park, Texas (BBNP) and 71 Gulch, Idaho. Exposures in this study formed at approx. 400-500 m below the pre-eruptive surface at BBNP and at ≤24 m below the pre-eruptive surface at 71 Gulch. Evidence that the host sediment was wet and unconsolidated at the time of formation include nearby desiccation cracks in sediment, peperites and phreatomagmatic deposits, as well as the transitioning of glass from sideromelane to tachylyte along the exterior margins of intrusions, resembling quench margins of pillow lavas.

To characterize the diversity of the billowed structures, a classification system has been developed utilizing 21 SfM-derived high-resolution three-dimensional models of exposed billowed intrusions across both locations. Seven structure types were recognized: linear, sinuous, teardrop, bulbous, circular, transitional, and overprinted. The scale of identified structures is similar between the two localities with insignificant variation in mean wavelength and amplitude of crests and troughs (≤6 cm). Relative abundances of each structure type are also similar, varying by <7% for each structure type between the two localities.

Each site hosts at least three structure types, no one billowed structure type is dependent on another, and dimensions of the structure types are similar at both sites, suggesting that depth is not a major influence in the occurrence of different structure types. Because billowed structures are evidence of non-explosive magma-water interaction, they serve as a platform to study the conditions in which the interaction can become explosive. Future research could involve a more detailed investigation into host-sediment water content, hydrostatic pressure, and the thermodynamics of the system.

APPROVAL PAGE

The faculty listed below, appointed by the Dean of the College of Arts and Sciences, have examined a thesis titled "Quantitative Characterization of Billowed Structures Along the Margins of Basaltic Intrusions to Determine Process and Timing of Formation: Case Studies from Big Bend National Park, Texas and 71 Gulch, Idaho," presented by Aaron J. Galletly, candidate for the Master of Science degree, and certify that in their opinion it is worth of acceptance.

Supervisory Committee

Alison H. Graettinger, Ph.D., Committee Chair
Department of Earth & Environmental Sciences

Tina M. Niemi, Ph.D.
Department of Earth & Environmental Sciences

Jejung Lee, Ph.D.
Department of Earth & Environmental Sciences

CONTENTS

ILLUSTRATIONS

TABLES

ACKNOWLEDGEMENTS

CHAPTER 1: INTRODUCTION

As magma travels through the subsurface it can interact with unconsolidated water-bearing sediment, reacting either explosively or non-explosively. The conditions that lead to explosive interaction are not well constrained due to explosive behavior disrupting the pre-existing conditions leading to the event. This study examines the products of non-explosive interaction and investigates the formation conditions of billowed structures preserved with the glassy margins of basaltic intrusions at Big Bend National Park (BBNP), Texas and 71 Gulch, Idaho. Billowed structures are defined as curved, ellipsoid, or elongate centimeter- to meter-scale undulations that crest outward perpendicular from intrusive margins separated by a trough and form from non-explosive interaction of magma and water-bearing sediment. By studying the chemical composition, depth of formation, and geometry of the billowed structures as well as understanding the characteristics of the host-sediment and other natural occurrences of complex, non-explosive interactions, such as peperites, we can better understand the conditions leading to an explosive event.

Phreatomagmatic Eruptions

Phreatomagmatic eruptions are a complex explosive eruption style derived from the interaction of magma and external water, such as, groundwater, surface water, or wet sediment (Zimanowski et al., 1991; White, 1996; Befus et al, 2008; Bennis and Graettinger, 2020; DeBone, 2020; Nemeth and Kosik, 2020). They differ from other forms of hydrovolcanism in that phreatomagmatic eruptions are triggered by ascending magma directly interacting with a water source (Nemeth and Koisik, 2020). Hydrothermal and phreatic eruptions result from indirect interaction with magma, where heat from magma

vaporizes groundwater and the resulting eruption does not expel juvenile material (Stearns and Macdonald, 1946; Nemeth and Kosik, 2020).

The compositions of host-material and magma, the hydrostatic and lithostatic pressures of the system, and the magma discharge rate are key variables to consider when evaluating the degree of explosivity from magma-water interactions (White et al, 2003; Casas et al., 2018). The constraints of each variable related to the degree of explosivity are not yet well understood.

Molten Fuel-Coolant Interaction

The primary source of energy that drives phreatomagmatic explosions is the transfer of heat between magma and water (Valentine et al., 2014). Explosive reactions do not always occur between the two interfaces because of the formation of a vapor film layer (Leidenfrost effect) preventing direct contact and the rapid transfer of heat (White et al., 1996; Zimanowski et al., 1997). In experimental work by Moitra et al. (2020), stable vapor films with a thickness of 1-2 millimeters formed at temperatures higher than the Leidenfrost temperature (675-950°C), about 50-250°C below the temperature of liquid basalt in nature. The vapor film remained stable for a short time (≤5 seconds for magma samples ~3.2 cm in diameter) before entering a nucleate boiling regime, where bubbles form at the magma sample surface, and then a free convection regime as the magma surface temperature decreased (Miotra et al., 2020). It was also found that with increasing water temperature a lower Leidenfrost temperature was achieved, and the stable vapor film was sustained for a longer period of time (Miotra et al., 2020). Such a short vapor film stability time scale may provide constraints on the time available for sufficient magma-water mixing required for

energetic explosions in nature (Miotra et al., 2020), where magma is many more times abundant and temperatures above Leidenfrost temperature are sustained for longer periods of time.

The method of rapid heat transfer which triggers phreatomagmatic explosions is described as molten fuel-coolant interaction (MFCI) (Figure 1.1) (Wohletz, 1986; Zimanowski et al., 1997; Buttner et al., 2002; Sonder et al., 2018; Nemeth and Kosik, 2020). MFCI is described by Zimanowski et al. (1997) in four phases which occur in a matter of microseconds: 1) a hydrodynamic mixing phase, 2) a trigger phase, 3) a fine fragmentation phase, and 4) a vaporization and expansion phase. As the vapor film provides a thermal insulating barrier between the magma water, the boiling interface gradually fragments the magma and mixing of the magma and water occurs (Wohletz, 1986). As fragmentation and mixing continues, a weak shockwave (<10 J) occurs (Zimanowski et al., 1997) triggering a rapid and complete condensation of the vapor film (Buttner et al., 2002). Contact between the two interfaces ensues and the melt is suddenly cooled and quenched as the water is simultaneously heated and expands, increasing the heat transfer rate (Zimanowski et al., 1997; Buttner et al., 2002). Further fracturing of the melt occurs, rapidly increasing the area of heat transfer, and, therefore, increasing the heat flux (Wohletz, 1986; Buttner et al., 2002). The water then becomes superheated to the point of spontaneous homogeneous nucleation (Wohletz, 1986), resulting in rapid vaporization and expansion, and thus an explosion (Zimanowski et al, 1997; Buttner and Zimanowski, 1998).

Specific conditions are still not fully understood for vapor film destabilization relating to phreatomagmatic eruptions. Research, including this study, continues to

investigate constraints, such as, the composition, permeability, porosity, and particle size of
sediments and the composition, flux, and heat transfer rate of intruding magma.
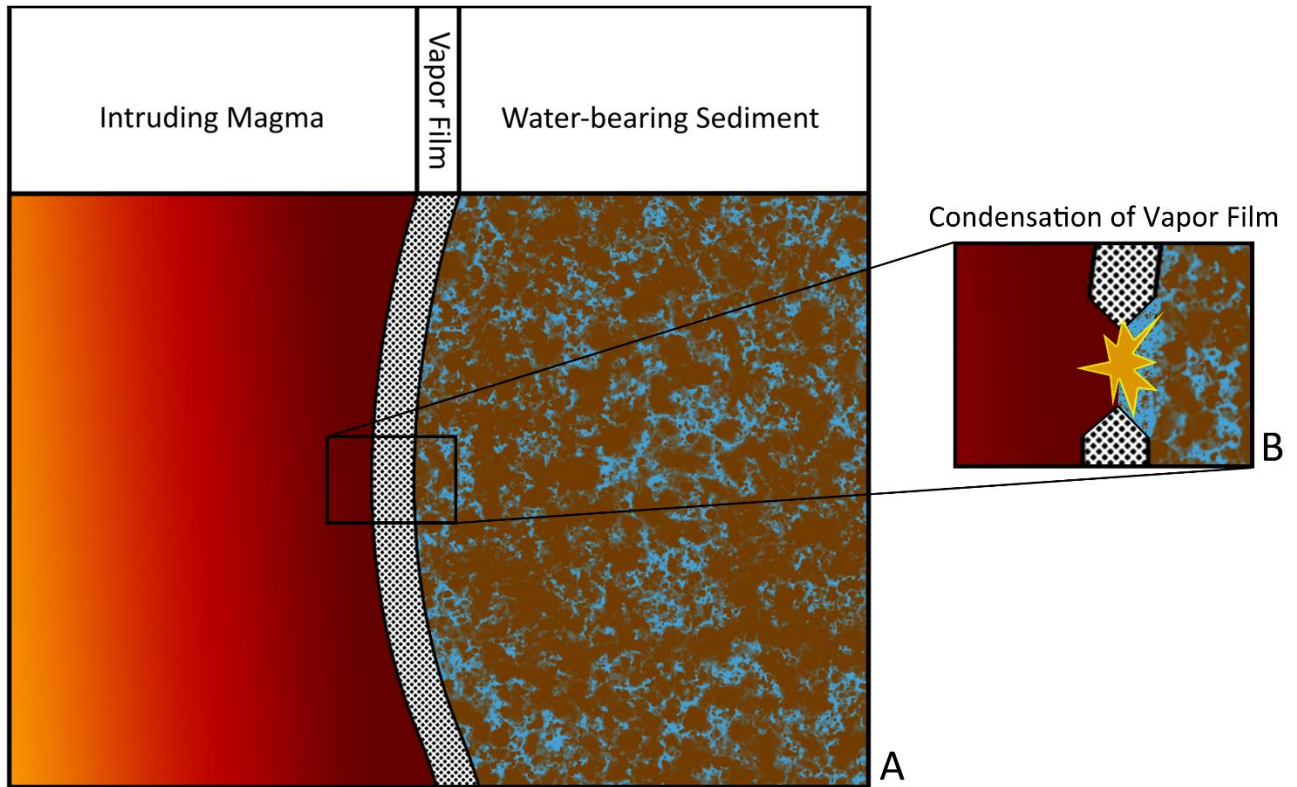
Figure 1.1 – A simplified representation of an MFCI. A and B occur sequentially in a matter
of microseconds, not simultaneously. A) A vapor film provides an insulating barrier between
the magma and water-bearing sediment. The boiling interface gradually fragments the
magma and mixing of the magma and water occurs. B) A weak shockwave triggers the
condensing of the vapor film allowing magma and water to make contact. Rapid heat transfer
occurs and the water becomes superheated, producing an explosion.

Non-Explosive Interaction and Billowed Intrusions

Due to explosive activity disrupting the pre-existing conditions leading up to a

phreatomagmatic eruption, features preserving evidence of non-explosive magma-water

interaction become a focal point for study. Exposed billowed intrusions and peperites present

an opportunity to study the paleo-conditions in which they formed, supporting our understanding of the constraints that result in either non-explosive or explosive interaction.

Billowed intrusions preserve billowed structures on the margins of basaltic intrusions which represent evidence of non-explosive interaction between magma and water-bearing sediment (Figure 1.2). Billowed structures are the curved, ellipsoid, or elongate centimeter- to meter- scale undulations that crest outward perpendicular from intrusive margins, separated by a trough (Befus et al., 2009), and have measurable wavelengths and amplitudes. Structures formed in basalt resembling the billows investigated in this study have been described in other publications but have not yet been examined in detail (Hanson and Hargrove, 1999; Kano, 2002; Lavine and Aalto, 2002; Befus et al., 2009; Bennis and Graettinger, 2020). Small-scale experimental models of intrusions have been created to examine the solidification and flux effects on the propagation of magma and sub-aqueous lava (Gregg and Fink, 1995; Gregg and Fink, 2000; Taisne and Tait, 2011), which have generated billow-like structures. Some billowed structure types, discussed later in this study, resemble the lobate textures described by Gregg and Fink (1995). Peperites, formed from the mingling of magma and sediment (Skilling et al., 2002), calcite, likely formed through secondary mineralization from hydrothermal pore fluids during the intrusion event (Poppe et al., 2020), and host-sediment are common fillers of the billow troughs.

Peperites are clastic rocks comprised of both igneous and sedimentary components generated by intrusive processes, or along the contacts of lava flows or hot volcaniclastic deposits with unconsolidated, typically wet, sediments (Skilling et al., 2002). They are important because they provide direct field evidence for magma and water-bearing sediment interaction (Skilling et al., 2002), including the magma-sediment mixing that precede

explosive eruptions corresponding to fuel-coolant interaction (Zimanowski et al., 1997). Their presence along billowed margins in both BBNP and 71 Gulch is further evidence of a water-saturated host environment at the time of intrusion.

50 centimeters

Figure 1.2 – Field photograph of billowed structures preserved along the margin of an intrusion.

Field Site Geologic Setting

Field campaigns to BBNP, Texas and 71 Gulch, Idaho were carried out to collect photographs for photogrammetric model generation, rock samples collection, and to conduct field measurements and interpretations. Both sites were selected because of the unique, well-preserved features formed from the interaction of magma and water-bearing sediment. The sites were also selected because of the differing depths below the pre-eruptive surface at which the examined outcrops were formed. Exposures examined in this study were formed at

approximately 400-500 m below the pre-eruptive surface at BBNP (Befus et al., 2009) and at <12 m below the pre-eruptive surface at 71 Gulch (Bennis and Graettinger, 2020).

Big Bend National Park Field Site

Big Bend National Park (BBNP), residing within the Trans-Pecos Magmatic Province in southwest Texas (Figure 1.3), contains an abundance of Cenozoic igneous rock derived from arc magmatism (Henry, 1986; Barker, 1987). Basaltic magma and water-bearing unconsolidated sediment interacted to form a variety of intrusive features, such as billowed intrusions and peperites, at field sites located in the western portion of BBNP. Eocene basaltic intrusions (~47-42 Ma) examined for this research formed at 400-500 m below the pre-eruptive surface and are now exposed at the ground surface, intruding into the Upper-Cretaceous Aguja and Javelina Formations and the Cretaceous-to-Eocene Black Peaks Formation (Figure 1.4) (Lehmen, 1991; Befus et al., 2008; Befus et al., 2009; Turner et al, 2011). The Aguja Formation is comprised of shallow-marine and coastal plain deposits of lenticular sandstone interbedded with carbonaceous shale, mudstone, and lignite (Lehman, 1991). The Javelina and Black Peaks Formations deposited as the seas regressed, depositing fluvial and basin-fill sediments of lenticular sandstones, flood-plain mudstones, and paleosol (Lehman, 1991).

A 4-km-long exposure of a N-S trending, Eocene (~47-42 Ma) (Befus et al., 2009), alkali-basaltic intrusion is located just north of mile marker 18 along Highway 118 (29°19'15.94"N, 103°27'5.21"W). The dike itself is herein described in two sections: the southern section and northern section. The southern section extends for 1.6 km, from just north of mile marker 18 on Highway 118, before becoming discontinued. A 1.3 km gap is

present between the southern section and the northern section. A 1.1 km exposure deemed

the northern section of the intrusion, then continues with a N-S trend. This intrusion hosts

nine of the eleven field sites in BBNP.

Two field sites are along an intrusion in the Study Butte area, near the Maverick Road

entrance station (29°17'42.14"N, 103°30'33.67"W). One of the two sites (AJG-007) is a dike

and the other (AJG-008) is the only sill observed in this study.
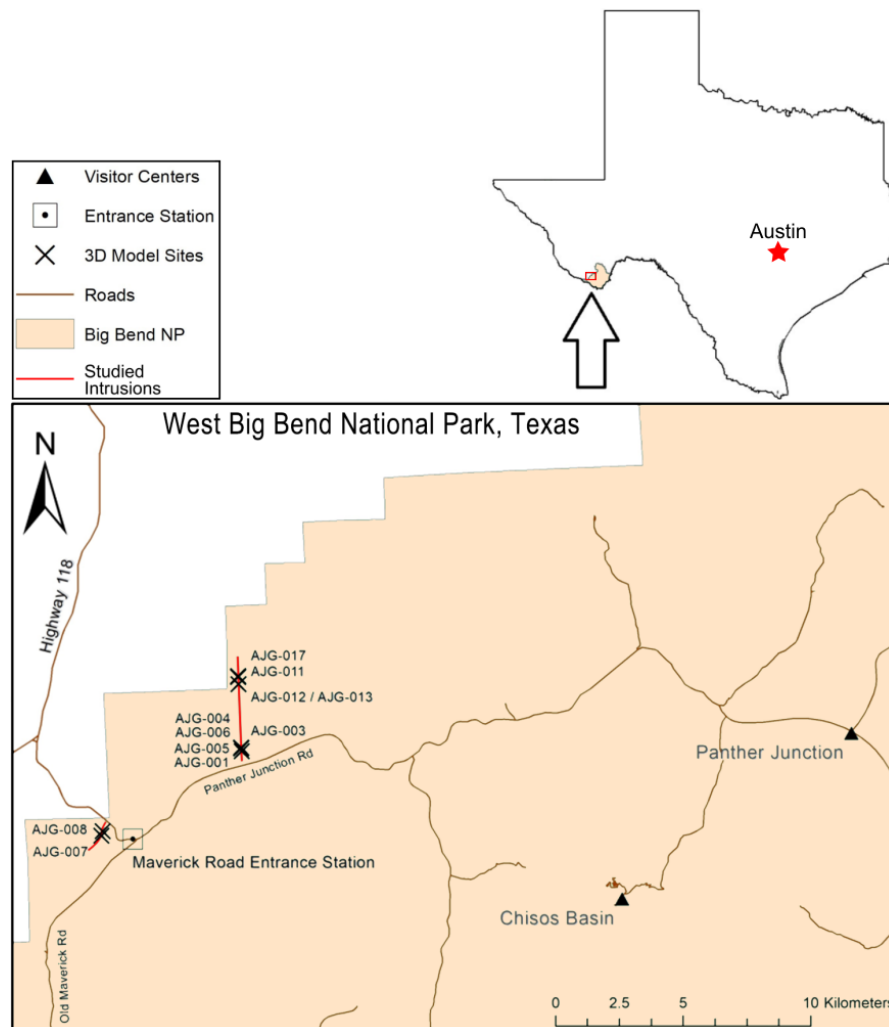
Figure 1.3 – Location map of the Big Bend National Park, Texas field site. The green color
represents the extent of Big Bend National Park boundaries. Brown lines are roads, main
roads are labelled. Red lines indicate studied intrusions. Black crosses indicate individual

field sites in their location along the studied intrusions. Maverick Road entrance station and park visitor centers are also marked.
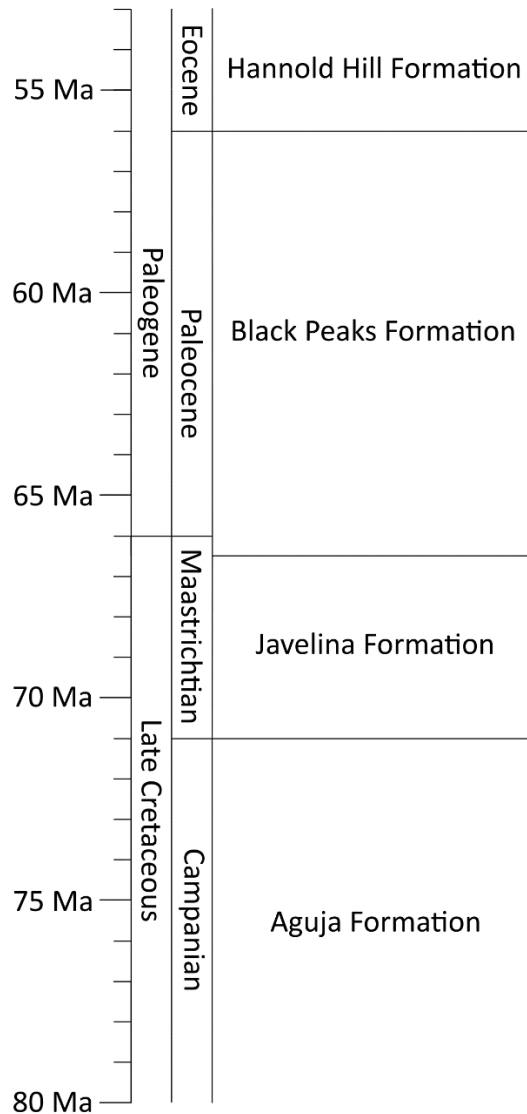
Figure 1.4 – Stratigraphic column of relevant Late Cretaceous to Early Eocene rock in the Big Bend National Park region. Modified from Lehman (1991) and Turner et al. (2011). The N-S trending, north of Panther Junction Road, is exposed intruding through the Black Peaks Formation. The intrusion near the Maverick Road entrance station is exposed intruding through Aguja and Javelina Formations.

71 Gulch Field Site

        71 Gulch is a 2 km long, ~0.15 km wide basaltic subaqueous phreatomagmatic fissure system located ~15 km southeast of the town Bruneau in Owyhee County, Idaho within the Western Snake River Plain (WSRP) (Figure 1.5). Erosion has revealed an ideal location to study exposures features exhibiting explosive and non-explosive magma-sediment interaction formed in a shallow-lacustrine environment. Examples of billowed intrusions, blocky and fluidal peperites, and pillow lavas are located across the field site, providing evidence of a water-saturated environment at the time of volcanic activity (Nemeth and White, 2009; Bennis and Graettinger, 2020). Previous K-Ar whole rock analysis of 71 Gulch basalt yields an age of 4.17 ± 0.72 Ma and is found interrupting the fluvio-lacustrine sediments of the Miocene-aged Chalk Hills and the Pliocene-aged Glenn Ferry Formations (Figure 1.6) (Nemeth and White, 2009; Bennis and Graettinger, 2020). The transition between the two formations is visible at 71 Gulch, indicated by layer of well-rounded quartzite cobbles in a sandstone matrix (Swirydczuk et al., 1981, Nemeth and White, 2009; Bennis and Graettinger, 2020).
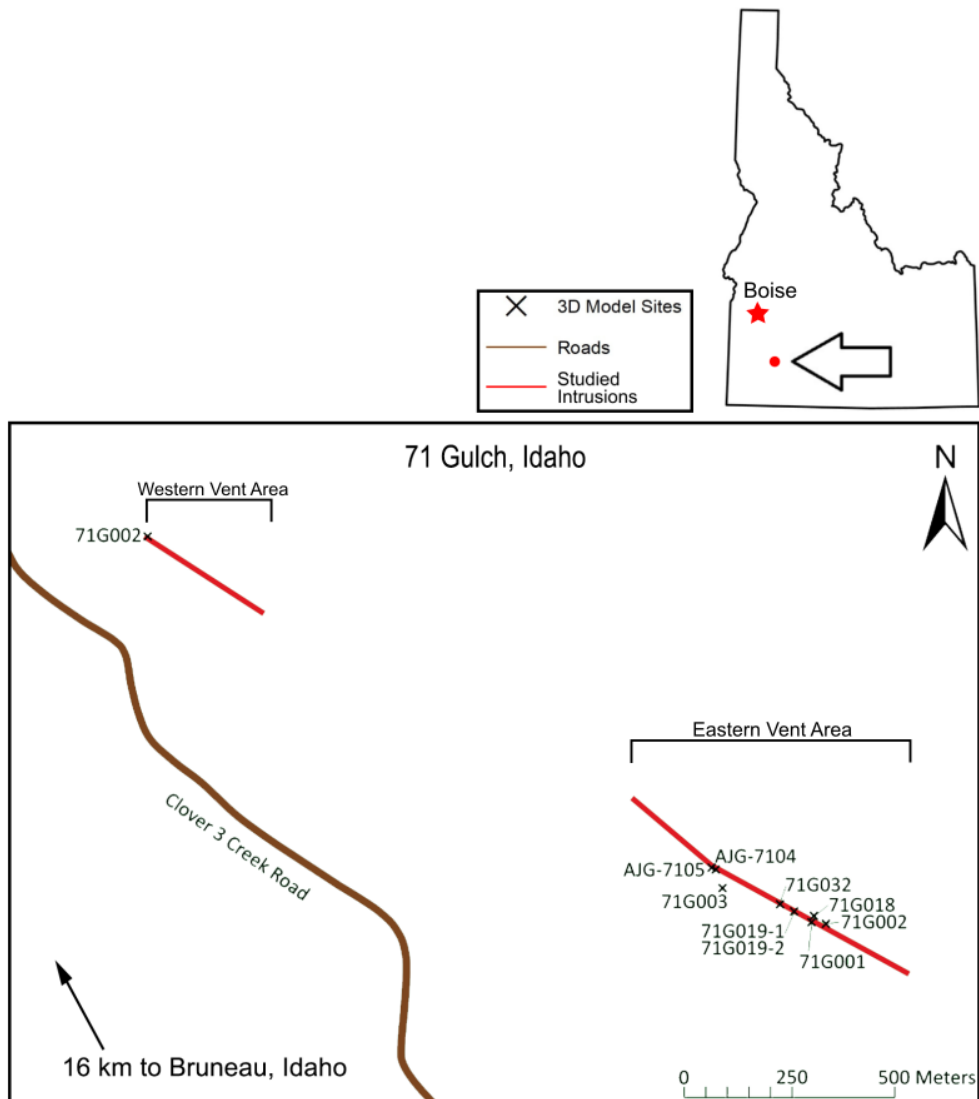
Figure 1.5 – Location map of the 71 Gulch, Idaho field site (N 42.77515, W 115.687 WGS 1984). The brown line represents the main road of the area, Clover 3 Creek Road. Red lines indicate the general trend of the studied intrusions. Black crosses indicate individual field sites in their location along the studied intrusions.
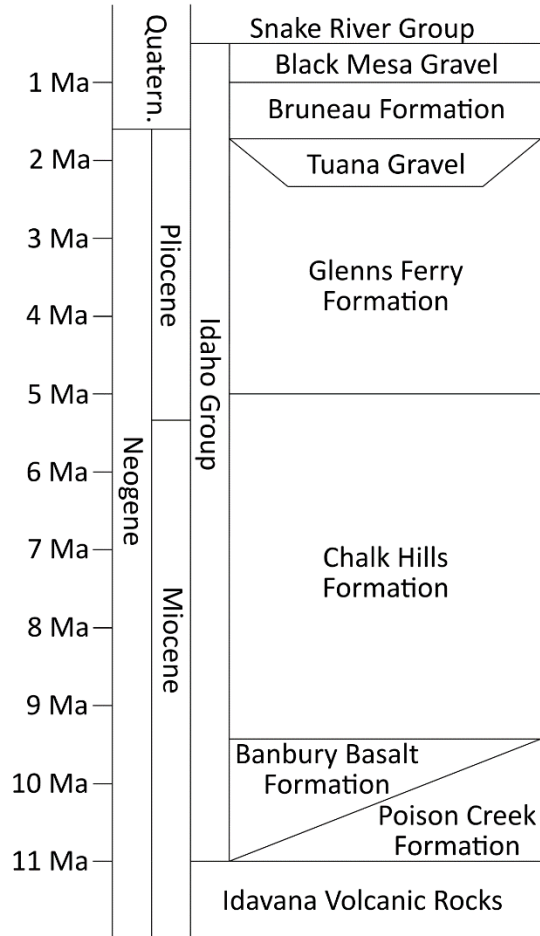
Figure 1.6 – Stratigraphic column of relevant Miocene to Quaternary rock in the Western Snake River Plain region. Modified after Malde (1991). Intrusions are exposed intruding through Chalk Hills and Glenns Ferry Formations.

Big Bend National Park Regional Geologic Setting

Big Bend National Park (BBNP) resides within the southern-most region of the Trans-Pecos Igneous Province (TPIP) in west Texas, bordering Mexico (Figure 1.3). The TPIP is bound by the Pecos River to the east, the south and west by the Rio Grande, and to the north by an east-west line 12 km north of the New Mexico-Texas border (Barker, 1987). Products of structural changes and volcanism found in the TPIP are the result of a long

geologic history from the Marathon orogeny event (~330 Ma) to the Basin-and-Range faulting of the Pleistocene (~2 Ma) (Poole et al. 2005).

The Marathon-Ouachita-Sonora orogeny event took place from the Mid-Mississippian to Early Permian (~330-285 Ma), spanning approximately 3000 km from Chihuahua and Sonora, eastward through Texas, northeast through Arkansas, and arcing southeastward to Mississippi (Poole et al., 2005). The event is signified by the subduction of the Laurentian plate (North American plate) beneath the Gondwanan plate (South American plate), resulting in the closing of the Rheic Ocean and the creation of the Marathon orogenic belt in BBNP (Hickman et al., 2009; Poole et al., 2005; Turner et al., 2011).

The Late-Triassic to Late-Cretaceous (~200-85 Ma) brought with it the breakup of Pangea (Page et al., 2008). Rifting caused the Gulf of Mexico to begin expanding and the area became an area of shallow-marine deposition (Lehman, 1991). The Late-Cretaceous introduced the deposition of the Aguja Formation (Figure 1.4) consisting of lenticular sandstone interbedded with carbonaceous shale, mudstone, and lignite deposited in a coastal plain environment (Lehman, 1991; Rowe et al., 1992; Turner et al., 2011).

A period of phreatomagmatic volcanism began within the boundaries of BBNP and the surrounding area during the Campanian (83-72 Ma), erupting along the Marathon-Ouachita structural front (Barker et al., 1987; Breyer et al., 2007; Befus et al., 2008). This Upper Cretaceous volcanism is interpreted as part of the western extension of the Balcones igneous province which reached its peak activity at this time (Byerly, 1991; Breyer et al, 2007). To the east, the province experienced subaqueous and Surtseyan eruptive activity as vents opened along the structural front; whereas the BBNP area, to the west, experienced

phreatomagmatic interactions between basaltic magma and water-saturated, unconsolidated sediment of the Aguja formation (Lehman, 1991; Breyer et al., 2007; Befus et al., 2008; Griffin et al., 2010, Hill, 2014).

The Laramide orogeny began affecting BBNP and the surrounding Trans-Pecos region from the Late Cretaceous through Early Tertiary (~70-50 Ma), post-dating the Aguja deposition (Lehman, 1991). The Laramide deformation resulted in the formation of the Tornillo Basin, bounded by the Sierra del Carmen-Santiago Mountains to the east and Mesa de Anguila to the west (Page et al., 2008, Turner et al., 2011). Sea level regression yielded a new depositional environment generating fluvial and basin-fill sediments, ultimately depositing the Javelina, Black Peaks, and Hannold Hill formations (the Tornillo group) (Figure 1.4) (Lehman, 1991; Page et al., 2008). The Javelina formation coincides with the beginning of the Laramide deformation which continues throughout the deposition of the Black Peaks and Hannold Hill formations (Lehman, 1991). The overlying Black Peaks formation consists of similar deposits of fluvial lenticular sandstones, flood-plain mudstones, and paleosol (Lehman, 1991). The Hannold Hill formation, consisting of conglomerate, conglomerate sandstone, and mudstone layering (Lehman, 1991), and indicates final deposition during the Laramide deformation which comes to an end at ~50 Ma (Page et al., 2008).

Typically, in a convergent tectonic setting, the volcanic arc would be ~100-150 km from the subduction zone. Arc magmatism occurred in TPIP, >700 km from the subduction zone, due to a phenomenon called flat-slab subduction, where the subducting Farallon plate did not descend directly into the mantle, but instead remained in contact with the upper plate before penetrating the asthenosphere (English et al., 2003). The resulting volcanic arc due to

14

the Farallon flat-slab subduction was the Cordilleran magmatic arc, which migrated across much of the southwestern U.S as it moved eastward, inevitably affecting the Trans-Pecos region at its eastern-most fringe (Henry and McDowell, 1986; Barker, 1987; Henry et al., 1991; English et al., 2003; Gilmer et al., 2003).

The primary volcanic activity that affected the TPIP occurred between 48-39 Ma (Price et al., 1987; Henry et al. 1991); although, the earliest described example of Tertiary magmatism in the TPIP is the quartz monzonite Red Hills intrusion, yielding an age of ~64 Ma (Gilmer et al., 2003). It was during this time that numerous small intrusions, including those focused on in this study, were emplaced. The Alamo Creek Basalt and the Ash Spring Basalt members of the Chisos formation were deposited (Lehman, 1991), and small instances of phreatomagmatic activity between basaltic magma and shallow groundwater occurred (Befus, et al., 2008; Befus, et al., 2009; Tuner et al., 2011; Hill, 2014; DeBone, 2020).

Roll-back or break-off of the Farallon plate resulted in partial melting of the lithosphere from 45- 36 Ma, producing the primary TPIP silicic volcanic activity (White et al., 2006; Parker et al., 2012). The region began to undergo an extensional phase due to continental rifting from 36-27 Ma as the broken Farallon plate sank, causing delamination of the lithosphere and generating bimodal and peralkaline volcanism as its interaction increased with the asthenosphere (White at al., 2006). Magmatism related to the subducting Farallon plate continued until 32 Ma, resulting in caldera eruptions and the emplacement of the intrusive and extrusive members of the Chisos Formation: The Bee Mountain Basalt (33-34 Ma), the Mule Ear Spring Tuff (34 Ma), and the Tule Mountain Trachyandesite (32-33 Ma) (Henry et al., 1991; Miggins et al., 2008; Turner et al., 2011).

Extension due to rifting across the Basin-and-Range Province of western North America continued, as did magmatism in the TPIP region, as Basin-and-Range normal faulting began 25 Ma (White et al., 2006; Page et al., 2008). Smaller volumes of mafic magma, almost exclusively alkali basalt and hawaiite, were emplaced mostly as dikes and some lavas (Henry et al., 1991). Basin-and-Range faulting is the most recent major tectonic event to affect the TPIP region, continuing activity until ~2 Ma, while magmatism came to an end in the TPIP ~17 Ma (Henry et al., 1991; Price et al., 1987; Page et al., 2008).

Western Snake River Plain and 71 Gulch Regional Geologic Setting

The Snake River Plain as a whole is comprised of three defined regions: The WSRP, the Eastern Snake River Plain and the Central Snake River Plain; each with their own unique geographical and tectonic settings (Woods and Clemens, 2002). Their combined boundaries cover much of southern Idaho and extend into eastern Oregon, northern Nevada, and Yellowstone National Park in eastern Wyoming (Figure 1.7) (Bonnichsen et al., 2008). The WSRP is a normal-fault bounded, intercontinental rift basin formed by northeast-southwest crustal extension from 12-7 Ma triggered by magmatism generated by the Yellowstone hotspot (Woods and Clemens, 2002; Bonnichsen et al., 2008). The Basin-and-Range structure, measuring approximately 70 km wide, 300 km long, and 2-3 km in depth, became inundated with the waters of a large lake, Lake Idaho, between 9.5-1.7 Ma (Shervais et al., 2002; Woods and Clemens, 2002). The presence of Lake Idaho resulted in the deposition of lacustrine and fluvial sediments, filling the basin with the 1.7 km thick, Miocene-to-Quaternary-aged Idaho Group (Malde and Powers; 1962; Leeman, 1982; Shervais et al, 2002; Bennis and Graettinger, 2020).
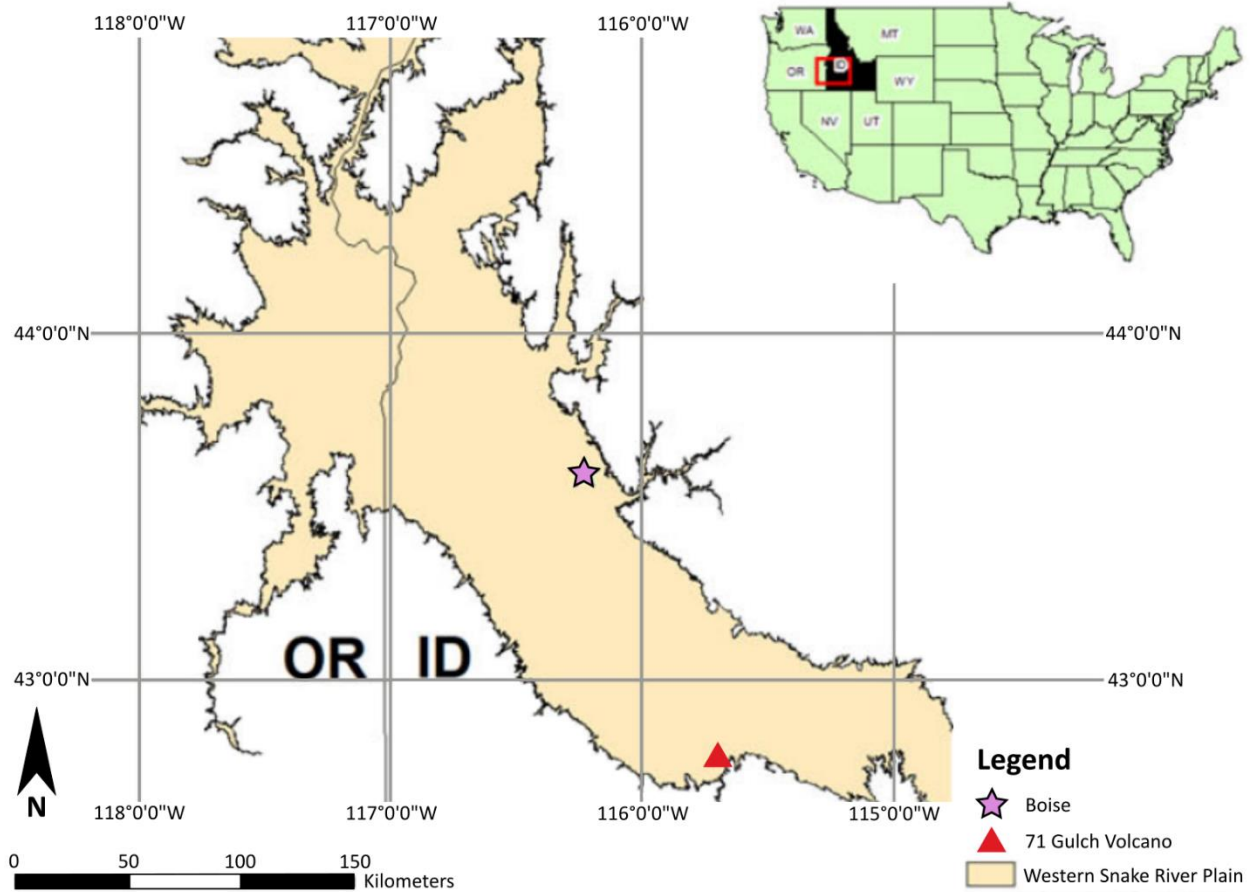
Figure 1.7 – Location map of 71 Gulch within context of the Snake River Plain and the Idaho-Oregon border. The red triangle represents the 71 Gulch volcano location. The purple star represents the location of Boise, Idaho. The tan color represents the extent of the Snake River Plain. Modified from Bennis and Graettinger, (2020).

Two formations within the Idaho Group are important to this investigation as they host the volcanic features examined in this study: The Chalk Hills Formation and the Glenns Ferry Formation. The Chalk Hills Formation underlies the Glenn Ferry Formation and overlies the Bandury Basalt (Figure 1.6) (Malde and Powers, 1962; Malde, 1991). It has exposures of up to 91 m thick and resembles typical lacustrine environments, consisting of laterally continuous consolidated silts and sands, as well as, large amounts of siliceous volcanic ash, fossils of three clam and six snail species, and secondary gypsum (Malde and

17

Powers, 1962). Separated by an upper sequence of quartzite cobble, the Glenns Ferry Formation overlies the Chalk Hills Formation and underlies the Tuana Gravel and Bruneau Formation (Malde and Powers, 1962). The Glenns Ferry Formation, reaching up to 610 m thick, consists of three primary interfingered facies of lacustrine, fluvial and floodplain deposits and minor volcanic material (Malde and Powers, 1962). The largest facies, based upon area and volume, is the lacustrine facies, consisting largely of tan silt, thin beds of ripple-marked sand and silt, and pale-yellow silt overlying a basal carbonate oolite or limestone bed (Malde and Powers, 1962). The fluvial facies consists of thick, parallel-bedded, unevenly layered pale brownish-gray sand and silt with some layers of crossbedding and ripple marks (Malde and Powers, 1962). Some beds of olive silt, dark-olive clay, and paper shale are present among the fluvial layers which are indicative of the flood-plain facies (Malde and Powers, 1962). Arkose sandstones, siltstones, and the previously mentioned quartzite cobbles are also present within the Glenns Ferry Formation (Malde and Powers, 1962).

Evidence of more than 400 eruptive vents and various types magmatic, phreatic, and phreatomagmatic eruption deposits have been recognized across the WSRP (Malde and Powers, 1962; Godchaux et al., 1992; Brand and White 2007; Bonnichsen et al., 2008; Nementh and White, 2009; Bonnichsen et al., 2016). Volcanic activity in the WSRP began about 11 Ma, prior to the formation of Lake Idaho, with the emplacement of a local rhyolitic basement created by fissure lavas along the basin's range-front faults (Malde and Powers; 1962; Bonnichsen, 1982). Basaltic activity in WSRP occurred in two main episodes, between which Lake Idaho sedimentation continued (Shervais et al., 2002; Bonnichsen et al., 2016). The first is suggested to be related to the plume-source mantle from the Columbia River

Plateau about 9 Ma, generating the lavas which rest atop the rhyolitic basement and underlie Lake Idaho sediments (Malde and Powers, 1962; Shervais et al., 2002). Volcanism and Lake Idaho sedimentation began overlapping in the Early-Pliocene through Late-Pleistocene introducing instances of phreatomagmatic eruptions, such as, those seen at 71 Gulch (Shervais et al., 2002; Nemeth and White, 2009; Bennis and Graettinger, 2020). Due to younger crustal extension and the migration of the Yellowstone hotspot, the second episode of basaltic activity occurred throughout the Pleistocene (2.2-0.4 Ma), overlaying lavas atop the Lake Idaho sediments (Shervais et al, 2002; White et al., 2002; Bonnichsen et al., 2016). Throughout this time, phreatomagmatic eruptions became the dominant eruption style as Lake Idaho began to drain and the region's lacustrine and volcaniclastic sediments became exposed (Bonnichsen and Godchaux, 2002; Shervais; 2002).

Evidence of Water-Bearing Sediment at the Time of Intrusion

Both BBNP and 71 Gulch host features that exhibit evidence for the presence of water at the time magma intruded into sediment. Desiccation cracks in sediment, peperites, pillow lavas, phreatomagmatic deposits, and transitional glassy margins reminiscent of quench margins of pillow lavas are evident at one or both localities, at or near the studied intrusions.

Desiccation cracks, formed from the drying of fine-grained soils in host sediment (Tang et al., 2010) were observed adjacent to several of the studied intrusions of BBNP (Figure 1.8), but are absent at 71 Gulch. Pillow lavas were observed at 71 Gulch, but not at BBNP, however, margins of glass from intrusions at both localities resemble the quench

19

margins of pillow lavas (Melson and Thompson, 1973; Kawachi and Pringle, 1988). These margins will be discussed in more detail in later sections.

Peperites, as previously discussed, form from the mixing of magma and water-bearing sediment. Peperites were observed at both localities but are more abundant across 71 Gulch (Bennis and Graettinger, 2020). Only a single peperite was noted along the N-S trending dike at BBNP. Phreatomagmatic vents and deposits were also evident across both localities. Subaerial and effusive phreatomagmatic deposits were evident across the 71 Gulch field site (Bennis and Graettinger, 2020). Remnants of phreatomagmatic slurry filling two diatreme feeders to small maars are also preserved in the vicinity of the Study Butte intrusions (Hill, 2014).

Figure 1.8 – Desiccation cracks in sediment adjacent to the intrusion at AJG-008 in BBNP.

CHAPTER 2: METHODOLOGY

This project utilizes a field component, a digital component, and a laboratory component. A week-long field campaign was conducted at two field locations, Big Bend National Park, Texas (BBNP) and 71 Gulch, Idaho, to collect imagery of billowed intrusions, perform field measurements, and collect samples. At each of the 21 field sites across both locations digital photos were captured and used to construct high-resolution three-dimensional models. Billow trough wavelength and amplitude measurements were recorded, as well as intrusion thickness, intrusion orientation, and host rock lithologic descriptions. Rock samples from intrusion margins, intrusion interior, and surrounding sediment were collected for geochemical and petrographic analysis from BBNP. Existing geochemistry data and rock samples for petrographic analysis from BBNP and 71 Gulch were also used for this investigation.

Field Work

Site Selection

Two field locations were selected for comparison: Big Bend National Park, Texas and 71 Gulch, Idaho. The two locations were selected because of previously identified exposures of preserved billowed structures in literature (Befus et al., 2008, 2009; Bennis, 2019); evidence of interaction between magma and water-bearing sediment; similar magma compositions, basaltic (71 Gulch) to alkali-basaltic (BBNP); and varying formation depths.

At least 7 field sites at BBNP and 71 Gulch exhibited billowed structure characteristics but could not be assessed. Issues with accessibility, safety during image capture, and weathering of an outcrop would exempt a field site. Vegetation, steep

topography leading to the outcrop, or unsafe conditions due to unstable rock or overhangs would create inaccessible or unsafe conditions. Glassy margins of the intrusion must have been at least partially intact to be considered. Glassy margins preserving billowed characteristics maintained smooth, curved glassy rinds as billows transitioned from trough to crest. Glassy margins were also typically lighter in color due to alteration and some lingering sediment adhered to the exterior (Figure 2.1).

Figure 2.1 – A visual representation, utilizing the AJG-007 model from BBNP, of well-preserved glassy margins versus poorly-preserved, weathered non-glassy margins of an intrusion. Note the darker coloration of the more weathered, non-glassy region.

Image Capture

The photogrammetry process involved a collection of photographs from each field site. Photographs were collected from the ground or portable step stool using a digital camera attached to an extendable monopod. Generally, approximately 60-120 photos were taken at each field site. A larger number of photos would be required for larger scale sites. Photographs were captured laterally along each vertical outcrop and the height of the camera could be adjusted up to 4 m above ground surface at each capture position. At each position, the viewing angle of the camera was adjusted appropriately multiple times to ensure that the entire area of interest would be captured from every possible viewpoint.

Three to six control points would be placed across the area of interest, dependent on the size of the area of interest, and their spatial locations were measured relative to the origin control point. Control points were added to the scene to constrain the dimensions of an outcrop in three dimensions and improve the accuracy of quantitative measurements of billowed margins.

An origin control point would first be positioned along the outcrop before positioning a second control point horizontally aligned with the origin control point to form an x-axis. The relative distances between control points were measured from the top-right, front-facing corner of each cube. The 7.5 cm-wide cubic wooden control points were attached to the rock faces using disposable wall hangers, which were easily removed and left no trace on the rock surface. The control points were painted identically so that each face and edge of the cube could be easily identified (Figure 2.2).
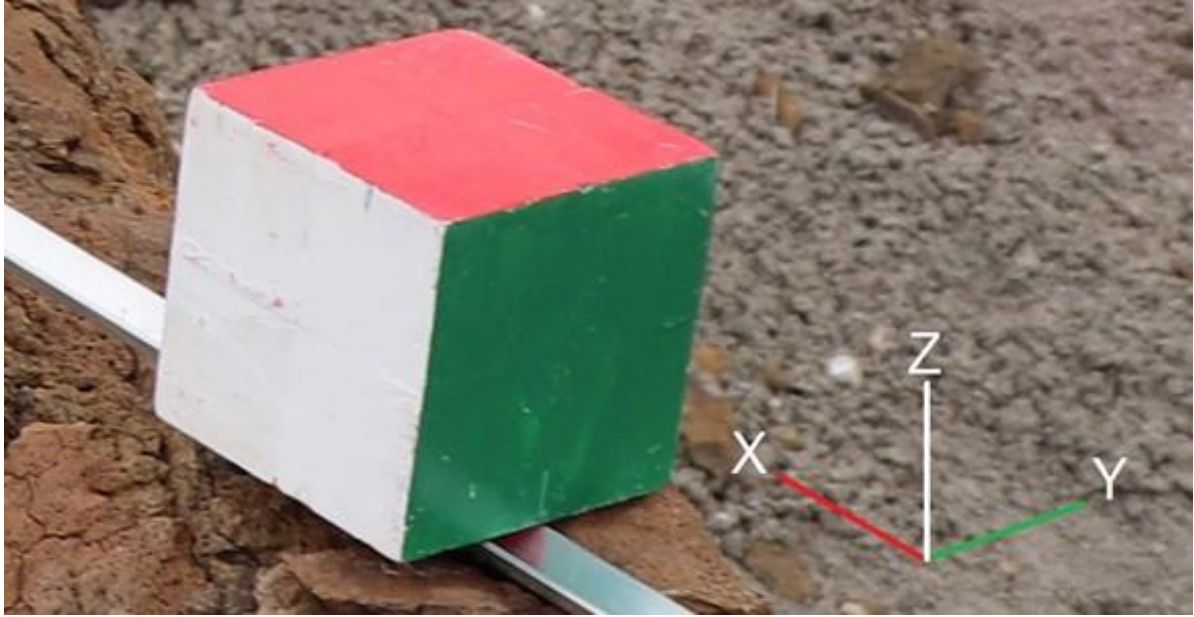
Figure 2.2 – A single control point cube, used to constrain the dimensions of the outcrops. An "origin cube" would be used as an origin point (0 m, 0 m, 0 m) and all other cubes would be measured relative to it. Measurements would be made from the top-front-right corner of each cube.

Manual Field Measurements and Sampling

At each site, 2-5 manual measurements of billow trough wavelengths and amplitudes were recorded. A total of 72 trough measurements were recorded in the field across both localities. Intrusion thickness and orientation, as well as host rock lithologic descriptions were recorded in the field. To measure the wavelength distance, a flat measuring stick would be placed on a billowed surface across a trough. The distance between the two locations where the measuring stick would contact the billowed surface was recorded as the wavelength distance. The amplitude would be measured to the deepest part of the trough, perpendicular to the plane of the wavelength measurement. The thickness of the intrusion was also measured in locations where both sides of the intrusion were exposed and could be

accurately and safely measured. Lithologic descriptions of the host sediment, the intrusion, and any alteration were also recorded.

Six rock samples were collected in BBNP for petrographic analysis as permitted by the National Park Service. Collected samples were roughly the size of a grapefruit or smaller and were targeted to minimize the visual impact in accordance with the research permit in BBNP. Constraints of density and viscosity of the intruding magma were calculated utilizing XRF and ICP-MS whole rock bulk and trace elemental analysis.

Model Processing and Assessment

After a field campaign, photographs were compiled to create high-resolution three-dimensional models of outcrops in AgiSoft Metashape Pro v1.6 software. The models were used to digitally revisit individual field sites for qualitative and quantitative information, such as billow geometries and dimensional measurements. Digital elevation models (DEMs) were be exported from AgiSoft Metashape Pro and imported into QGIS v3.14 software to quantitatively measure billowed structures for each individual field site. Google Earth Pro was used in conjunction with GPS location data (latitude, longitude, and elevation) utilizing a WGS 84 Geographic System and ArcMap 10.5 to spatially map field site locations, sample locations, and other sites of interest.

Structure from Motion (SfM) Photogrammetry and Model Processing

High-resolution three-dimensional models of 21 field locations were generated using AgiSoft Metashape Pro software. The software reconstructs the geometry of the field sites from a collection of overlapping photographs by triangulating the locations of individual features found in multiple images (Figure 2.3). Accurately produced models are useful for

identifying geologic structures and making quantitative measurements at a centimeter scale

without revisiting the field area.
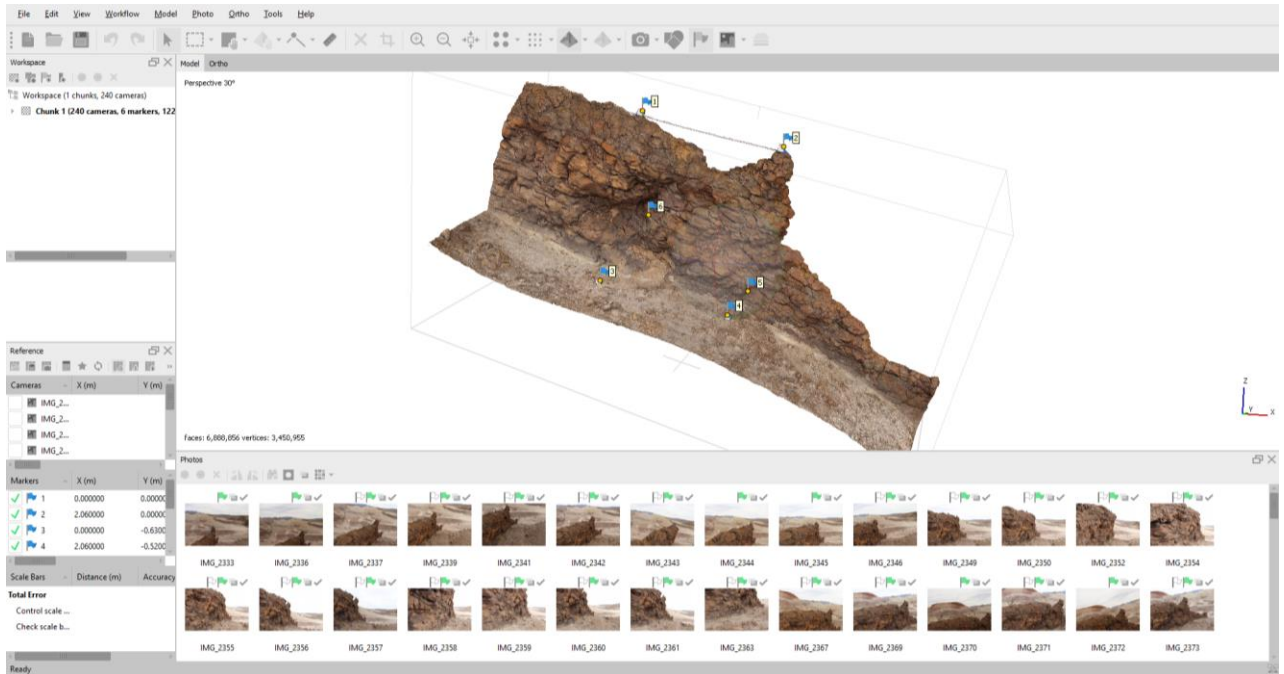
Figure 2.3 – A SfM three-dimensional model of AJG-017 of BBNP in the AgiSoft
Metashape interface. Blue flags on the model are control point locations correlating with
their coordinates recorded in the field and their location in relevant photos.

Control point markers within the software were manually positioned to correspond

with their actual positions in each photo, aiding the software in constraining the dimensions

of the site. AgiSoft Metashape Pro then aligns the photographs using a feature-matching

algorithm called Scale Invariant Feature Transform to triangulate groups of pixels that can be

identified in multiple photographs, correcting for the differing camera orientations and

positions, and generating a sparse point cloud (Lowe, 2004). Photo alignment was performed

with the "highest" accuracy setting selected; other setting remained default. After a sparse

point cloud was created, the positions of the control point markers were verified and

corrected if adjustment was needed. Then, a dense point cloud was created, generating a

visualization of calculated depth information based upon the camera position of each photo. Dense cloud settings were set to "high" for general quality and "aggressive" for depth filtering; other settings remained default. After a dense cloud is produced, a mesh would be generated by fitting polygons to the dense cloud and stitching them together. Default settings were used for this process. Once a mesh was created, a texture model would be generated using default settings, essentially overlaying the overlapping photographs onto the generated mesh. The results of a texture model are a completed three-dimensional reconstruction of the field site.

To collect quantitative information from the model, a digital elevation model (DEM) was generated, viewed from the front-facing X-Z planar projection. The DEM data was sourced from the dense cloud, utilizing the coordinate system of relative control point measurements. For some models, the angle at which the DEM was captured needed to be slightly adjusted to account for the dip of the outcrop. The DEM was then exported as an .asc raster file and imported into QGIS v3.14 software for quantitative analysis.

Model Validation and Measurements

Field measurements of billow trough wavelength and amplitude were compared to digital measurements to assess the accuracy and validity of the 3D model surface using DEMs of each 3D model. After DEMs were imported into QGIS software, the profile tool plugin was utilized to digitally reconstruct our field method for trough measurements (Figure 2.4).
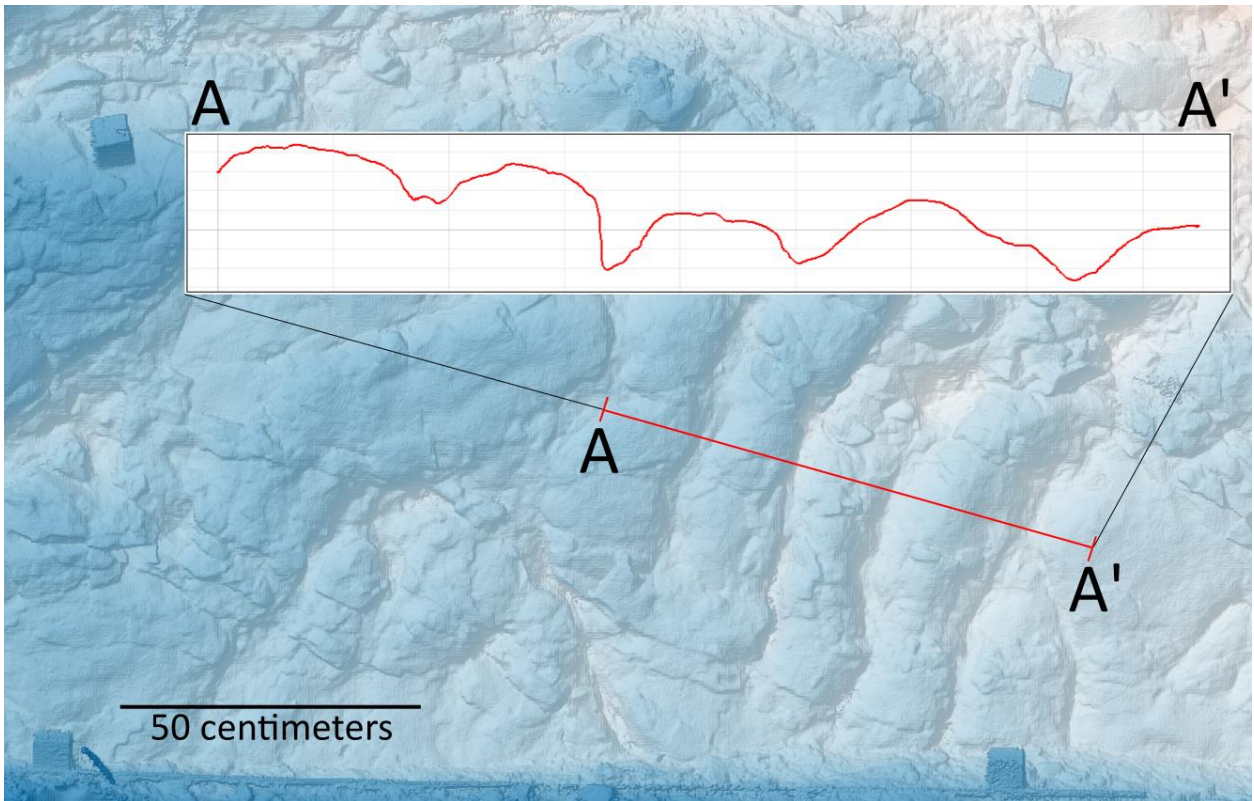
Figure 2.4 – A DEM model with a profile line drawn across several billowed structures, highlighting the repeating crests and troughs of billow.

A digital profile line would be drawn across the DEM at the location of a field measurement. A flat digital line, used to imitate a measuring stick in the field, could then be placed across the profile and the distance between crests could be measured and recorded as a trough wavelength. Perpendicular to the wavelength plane, a line would be measured to the deepest portion of the trough. The distance of this line between the plane of the wavelength measurement and the base of the trough would be recorded as the trough amplitude. The digital measurements were then compared to the field measurements to assess the accuracy of each mode. If a digital measurement was $\leq\pm2$ cm of the field measurement, the model measurement was deemed valid. Any measurement $>\pm2$ cm would be deemed invalid. Additional measurements from sites deemed as invalid were still recorded and considered.

While precise measurements of structures are useful, model accuracy is adequate to understand the general scale of these structures.

Classification of Billowed Structures

Based upon the geometry of a billowed structure, the structure would fall into one of seven classifications: linear, sinuous, bulbous, teardrop, circular, transitional, or overprinted (Figures 2.5 and 2.6). The anatomy of a billow herein is described in terms of general wave anatomy. Crests represent the upper, curved portions of a billow with the highest elevation values. Troughs represent the lower, curved portion of a billow with the lowest elevation values. The geometry of the billowed structure is defined by the character of the trough or troughs, which affect the behavior of the billow crest.

Each of the 21 models was visually examined for features falling into each classification. Linear crest structures exhibit parallel or sub-parallel troughs on either side of the crest, aligned in similar orientation (Figure 2.6A). Sinuous crest structures exhibit troughs on either side of the crest, maintaining a parallel to sub-parallel characteristic and have a gentle to sharp curve (Figure 2.6B). Bulbous crest structures exhibit troughs on either side of a crest which do not resemble the behavior of each other (Figure 2.6C). Teardrop trough structures exhibit a circular depression with a single elongated trough extending out from the point depression, resembling the shape of a teardrop (Figure 2.6D). Circular trough structures are indicated by a circular to oval depression that resembles a bowl-like shape without an elongated trough extending from it (Figure 2.6E). Transitional troughs are any elongate trough between two crests which do not have an apparent point-depression. Transitional troughs have sub-categories based upon the surrounding crest type (linear-linear, sinuous-

sinuous, bulbous-bulbous linear-bulbous, linear-sinuous, and bulbous-sinuous), but are compiled into a single classification due to their similar geometry. Overprinted structures are an interplay of the previously mentioned structure classifications which appear to interrupt a sequence of repeated billowed structures, resembling an unconformity.
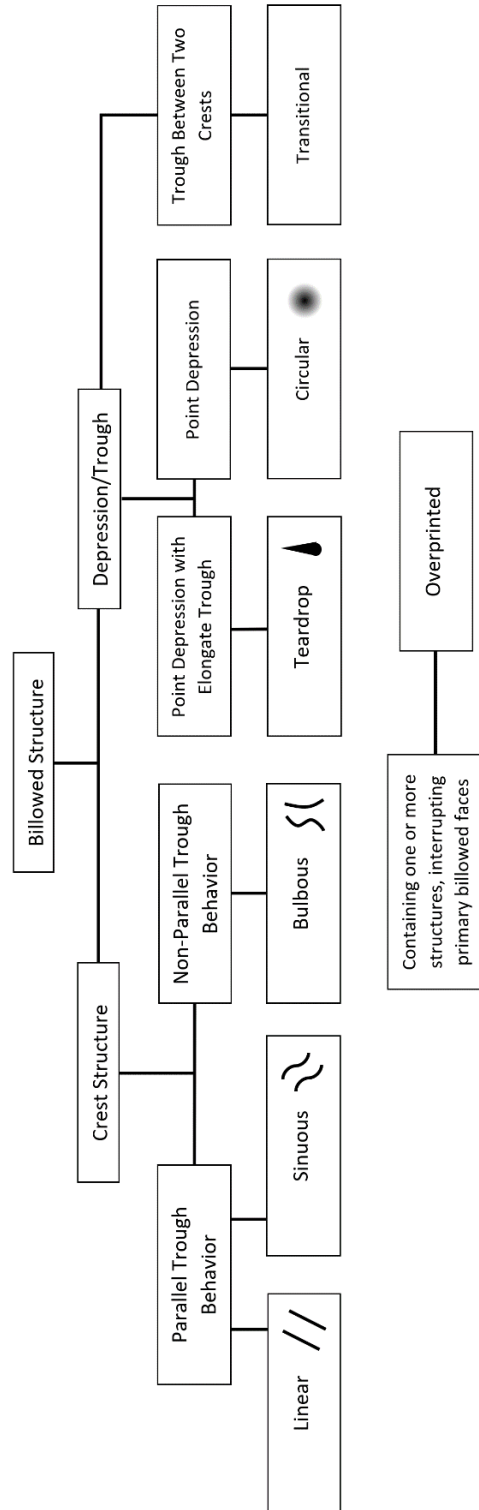
Figure 2.5 – A flow chart representing the logic for classifying identified billowed structures. Crest structures include: Linear, sinuous, and bulbous classifications. Trough structures include: Teardrop circular, and transitional classifications. Overprinted structures are an aggregate of any of the other structure classifications that appear to interrupt a repeating segment of another class.
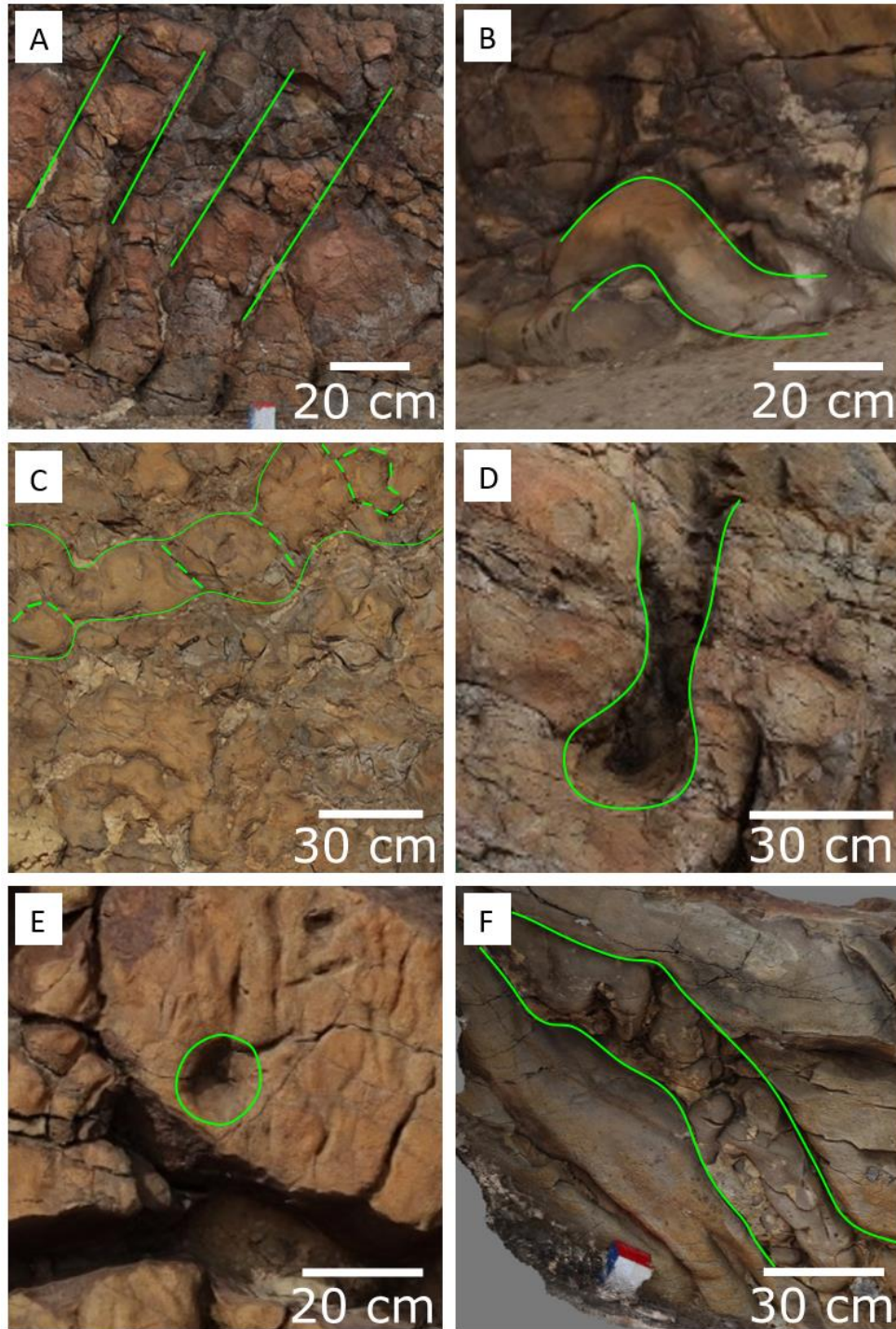
Figure 2.6 – Representations of each structure classification. A) Linear structures exhibiting linear-parallel trough behavior; B) A sinuous structure exhibiting curved-parallel trough behavior; C) Bulbous structures exhibiting non-parallel trough behavior, dashed lines are additional, more subtle troughs; D) A teardrop structure, exhibiting a single trough leading outwards from a depression; E) A circular structure, exhibiting a single depression without a trough leading outwards; and F) an overprinted structure, exhibiting an aggregate of smaller-scale linear, sinuous, and bulbous structures interrupting a larger-scale linear sequence.

Linear Crest Orientations

The orientations of groups of linear crest structures were measured from DEMs. The angle measurement tool in QGIS software was utilized to take the orientation measurements on model DEMs relative to the x direction in the modern orientation (Figure 2.7). A 90° measurement would have the linear structure oriented skyward, perpendicular to the X-axis surface. A 180° measurement would have the linear structure oriented parallel to the X-axis surface.
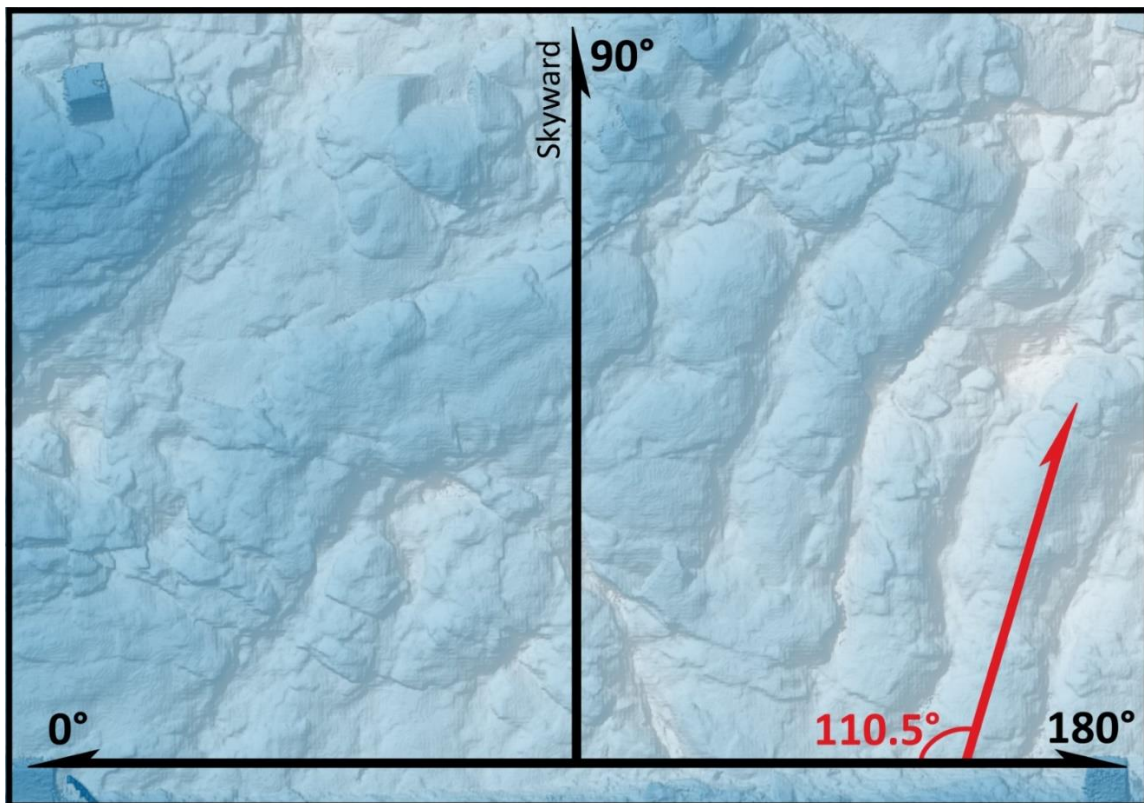
Figure 2.7 – A representation of linear crest orientation measurements utilizing a DEM of AJG-001 from BBNP. 0° represents north along the N-S trending dike at BBNP, and west in 71 Gulch. 180° represents south along the N-S trending dike at BBNP, and east in 71 Gulch. In both localities, 90° represents present day skywards, perpendicular from the level plane between control points along the base of the outcrop. The red arrow and angle represent the generally orientation of a linear crest.

Viscosity Calculations

Calculations of magma viscosity were conducted utilizing temperature (°C) and whole rock oxide weight percent data of three existing samples from BBNP and five existing samples from 71 Gulch. The Magma Viscosity Calculator spreadsheet developed at Whitman College was used after the methods of Shaw (1972). A range of possible viscosities was calculated by using varying temperatures (900°C, 1000°C, 1100°C, and 1200°C) and varying percentages of H_2O (1%, 2%, and 3%).

Density and Lithostatic Pressure Estimate Calculations

Estimates of host sediment and magma density were calculated using available data for each locality. The Javelina and Black Peaks formations correlate with basalt geochemistry samples used for magma density estimation at BBNP. Unsaturated density estimates for the two formations were derived from Martin (2007) based on modern conditions of exposed stratigraphy at the Grapevine Hills area of BBNP. Because porosity, and therefore the saturated densities, of the sediment is unknown, 15% and 30% porosity were used to calculate density estimates of saturated sediment from BBNP to observe a range of potential saturation densities. 30% porosity is presumed to be extreme due to confining pressure and compaction but was established to evaluate a high-order saturated sediment density to compare to magma density.

The Glenns Ferry formation correlates with basalt geochemistry samples used for magma density estimation at 71 Gulch. Host sediment density estimates of the Glenns Ferry formation were calculated utilizing three sediment samples from the field and equation (1) to calculate density:

$\rho=m/v$ (1)

where, ρ is the density of the rock, m is the mass of the rock, and v is the volume of the rock. Volume was recorded by measuring the difference in water volume (mL) after submerging a 71 Gulch sample in a graduated cylinder filled with 150 mL of water. Before submerging the sample, the sample was wrapped tightly with parafilm wax to obtain an unsaturated volume and was later unwrapped to obtain a saturated volume. Mass (g) was recorded to the hundredths decimal place before and after the parafilm wax was applied using a digital scale. Porosity of 71 Gulch samples were estimated by comparing the saturated and unsaturated volumes of the samples. The density of a water saturated sample was then estimated by adding the percent porosity as water to the unsaturated density, using 1.00 g/cm^3 as the density of water. Because small pockets of air could develop between the sample and the parafilm wax, porosity could exceed realistic percentages (>30%). To account for this, a sample with a calculated porosity estimate >30% would be adjusted to 30% before calculating its saturated density.

Unnormalized whole rock oxide weight percent data from three samples from BBNP and five samples from 71 Gulch were input into the Magma Density Calculator spreadsheet, developed at Whitman College after methods of Bottinga and Weill (1970). The calculator also utilizes the input of temperature (°C) and pressure (MPa). For temperature, 1100°C was used for all samples as this was found to be the most suitable natural temperature regime at which the magma intruded based on thin section observations and viscosity calculations. Pressure was calculated utilizing equation (2) from Turcotte and Schubert (2002), assuming an unconsolidated rock section the lithostatic load P_L is:

$P_L = \rho g t,$ (2)

where, ρ is the density of the rock, g is the acceleration due to gravity (9.81 m/sec^2), and t

height of the rock column.

Thin Section and Geochemical Analysis

Petrographic descriptions and photomicrographs were documented for each thin

section. Characteristics of the glassy intrusive margins were analyzed, including glass type,

vesicle characteristics, preferred orientation of crystals, the size of crystals, and the

mineralogy.

Six samples from BBNP were collected and cut for the preparation of 13 thin

sections. The samples were cut and then shipped to the National Petrographic Service in

Rosenberg, Texas for thin section production. Two samples for geochemistry originating

from BBNP had been cut and shipped to Washington State University GeoAnalytical Lab,

but due to delays related to COVID-19, will not be available before the completion of this

investigation. X-ray fluorescence (XRF) analysis and inductively coupled plasma mass

spectrometry (ICP-MS) for whole rock bulk and trace elemental analysis data for BBNP

samples was performed by Washington State University GeoAnalytical Lab and shared by

Dr. Richard Hanson and colleagues at Texas Christian University.

51 samples of different lithologies from 71 Gulch had been previously prepared by

Burnham Petrographics in Rathdrum, Idaho (Bennis, 2019). Five relevant thin sections from

intrusions at 71 Gulch were utilized in this investigation. Petrologic descriptions and

photomicrographs of the thin sections were collected. XRF analysis and ICP-MS for whole

rock bulk and trace elemental analysis data for 71 Gulch samples was performed by

Washington State University GeoAnalytical Lab and shared by Dr. Alison Graettinger and

Kadie Bennis.

CHAPTER 3: RESULTS

Model Validity

Multiple measurements from each individual field site were used to evaluate DEM-derived measurements of billowed structures. All 21 DEM models were deemed acceptable for use. Errors between field and digital measurements were considered minimal and are not on a scale to significantly affect the resulting data. 13 of the 21 DEM models created contained at least one measurement, wavelength and/or amplitude, with an error of ±2 cm when compared to field measurements. Of those 13 models, 8 models contained only one error >±2 cm: 7 with an error of ±3 cm and 1 with an error of ±4 cm.

Of 144 total measurements (72 of wavelength, 72 of amplitude) across both localities, only 22 measurements exceeded a 2 cm difference between field and digital measurement; 42 measurements saw no change between field and digital measurement. The maximum error measured for wavelength is 8 cm (model AJG-7101) and the maximum error measured for amplitude is 9 cm (model AJG-001). The maximum number of errors at a site was 4 of 6 measurements (AJG-7101).

Billow Structure Population

337 billowed structures were identified and measured in models from 11 field sites at BBNP (Figure 3.1, Table 3.1.). These features were divided into trough (n = 132) and crest (n = 205) structures. Bulbous crest structures (n = 123, 36.5%) are the most abundant classification at BBNP. Next most abundant are transitional trough structures (n = 108, 32.0%) and linear crest structures (n = 66, 19.6%), respectively. Sinuous crest (n = 16, 4.7%) teardrop trough (n = 14, 4.2%) and circular trough structures (n = 10, 3.0%) are present at most field sites, but are fewer in number. Two overprinted structures were identified at

BBNP. Overprinted structures are recognized but are not accounted for in population statistics.
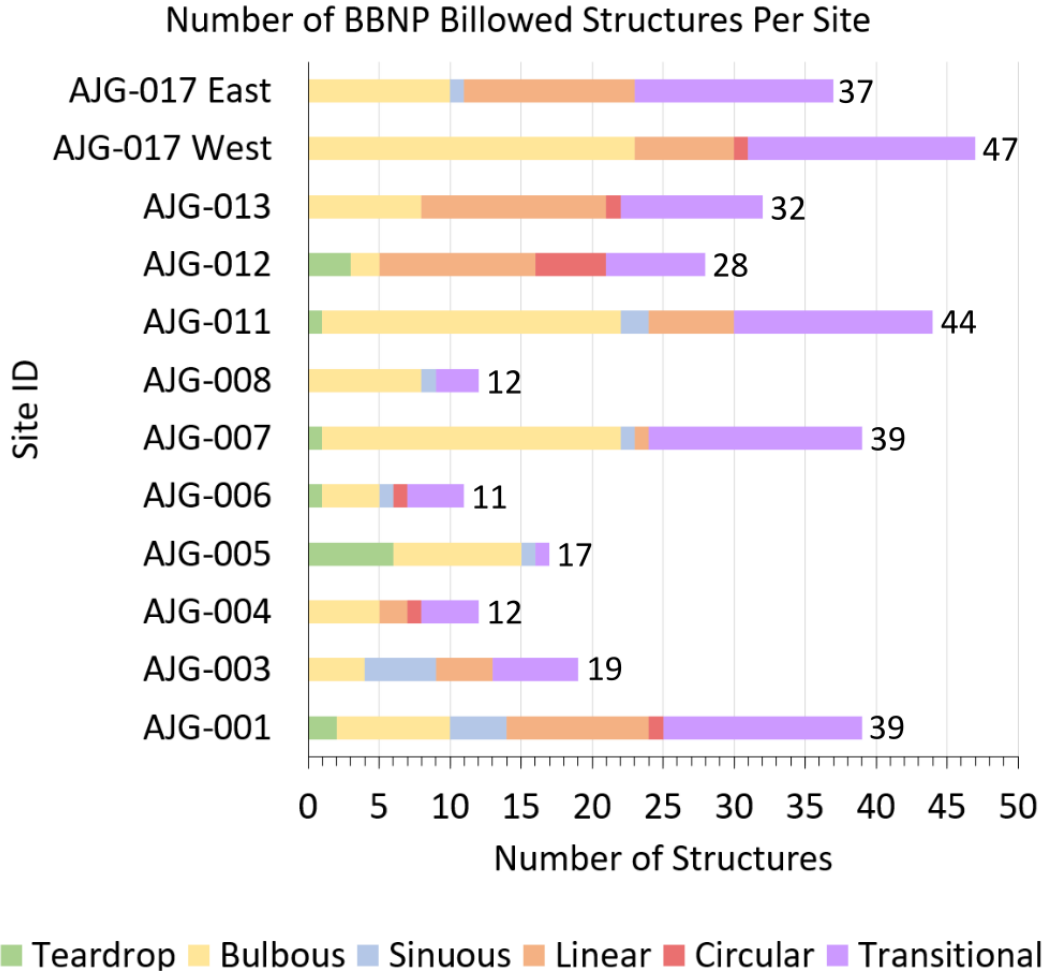
Figure 3.1 – Occurrences of each structure type identified at each field site in Big Bend National Park. Sum of identified structures at a site is labelled to the right of each bar.

Table 3.1 – Billowed structure populations by site at Big Bend National Park.

Site ID	Structure Type					
	Bulbous	Transitional	Linear	Circular	Sinuous	Teardrop
AJG-001	8	14	10	1	4	2
AJG-003	4	6	4	0	5	0
AJG-004	5	4	2	1	0	0
AJG-005	9	1	0	0	1	6
AJG-006	4	4	0	1	1	1
AJG-007	21	15	1	0	1	1
AJG-008	8	3	0	0	1	0
AJG-011	21	14	6	0	2	1
AJG-012	2	7	11	5	0	3
AJG-013	8	10	13	1	0	0
AJG-017 West	23	16	7	1	0	0
AJG-017 East	10	14	12	0	1	0
Total Quantity:	123	108	66	10	16	14
Percent of Total:	36.5%	32.0%	19.6%	3.0%	4.7%	4.2%

198 billowed structures were identified and measured in models from 10 field sites at 71 Gulch (Figure 3.2, Table 3.2). These features were divided into trough (n = 84) and crest (n = 111) structures. Bulbous crest structures (n = 80, 40.4%) are the most abundant classification at 71 Gulch. Next most are transitional trough structures (n = 67, 33.8%) and linear crest structures (n = 24, 12.1%), respectively. Circular crest (n = 14, 7.1%), sinuous crest (n = 7, 3.5%), and teardrop trough structures (n = 6, 3.0%) are present at most field sites, but are fewer in number. No overprinted structures were identified at 71 Gulch.

Number of 71 Gulch Billowed Structures Per Site
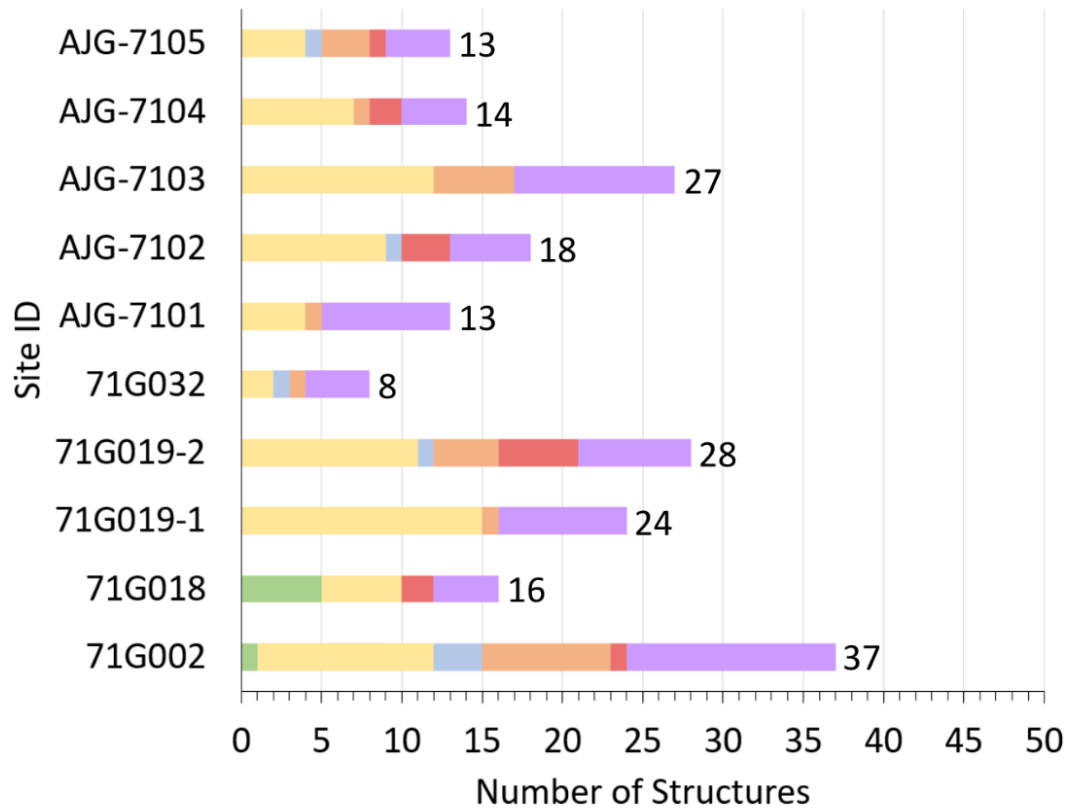
Figure 3.2 – Occurrences of each structure type identified at each field site in 71 Gulch. Sum of identified structures at a site is labelled to the right of each bar.

Table 3.2 – Billowed structure populations by site at 71 Gulch.

Site ID	Structure Type					
	Bulbous	Transitional	Linear	Circular	Sinuous	Teardrop
71G002	11	13	8	1	3	1
71G018	5	4	0	2	0	5
71G019-1	15	8	1	0	0	0
71G019-2	11	7	4	5	1	0
71G032	2	4	1	0	1	0
AJG-7101	4	8	1	0	0	0
AJG-7102	9	5	0	3	1	0
AJG-7103	12	10	5	0	0	0
AJG-7104	7	4	1	2	0	0
AJG-7105	4	4	3	1	1	0
Total Quantity:	80	67	24	14	7	6
Percent of Total:	40.4%	33.8%	12.1%	7.1%	3.5%	3.0%

Bulbous crests and transitional troughs were identified in all 21 individual field sites in both localities. Linear crests were identified at 9 of the 11 field sites at BBNP and at 8 of the 10 field sites at 71 Gulch. Circular troughs were identified at 6 of the 11 field sites at BBNP and at 6 of the 10 field sites at 71 Gulch. Sinuous crests were identified at 6 of the 11 field sites at BBNP and 5 of the 10 field sites at 71 Gulch. Teardrop troughs were identified at 6 of the 11 field sites at BBNP and at 2 of the 10 fields sites at 71 Gulch.

Billowed Structure Dimensions

Big Bend National Park

Trough structure wavelength dimensions vary from 5 cm to 110 cm with a mean of 20 cm, while trough amplitude dimensions vary from 1 to 34 cm with a mean of 6 cm. A single 110 cm wavelength measurement of a circular trough exceeds 77 cm. Teardrops

structures have the greatest mean trough wavelength (26 cm) and amplitude (13 cm), while transitional troughs have the lowest mean wavelength (19 cm) and lowest mean amplitude matching that of circular structures (5 cm).

Crest structure wavelength dimensions vary from 4 cm to 231 cm with a mean of 25 cm, while crest amplitude dimensions vary from 1 to 30 cm with mean of 5 cm. A single 231 cm wavelength measurement of a bulbous crest is an outlier; all other crest structure wavelength measurements are ≤110 cm. Bulbous crests have the greatest mean crest wavelength (30 cm) and linear crests have the lowest (17 cm), while sinuous crests have the greatest mean amplitude (7 cm) and linear crests have the lowest (4 cm).

Two overprinted structures were recognized at BBNP, but due to the irregular geometry of overprinted structures, their dimensions were not accounted for among the other structures. Measurable dimensions of other structure types which make up the overprinted structures were recorded.

71 Gulch

Trough structure wavelength dimensions vary from 6 cm to 63 cm with a mean of 23 cm, while trough amplitude dimensions vary from 1 to 25 cm with a mean of 8 cm. Teardrops structures have the greatest mean trough wavelength (26 cm) and circular structures have the lowest (21 cm), while transitional troughs have the greatest mean amplitude (8 cm), while circular structures have the lowest mean amplitude (6 cm)

Crest structure wavelength dimensions vary from 7 cm to 58 cm with a mean of 25 cm, while crest amplitude dimensions vary from 2 to 21 cm with mean of 7 cm. Bulbous crests have the greatest mean crest wavelength (26 cm) and linear crests have the lowest (22

cm) matching that of sinuous crests. Linear and sinuous crests have the same greatest mean

amplitude (8 cm) and bulbous crests have the lowest (7 cm).

Linear Crest Structure Orientation

For billowed intrusions that contained multiple parallel linear crests, the orientation

angle of linear crests was recorded relative to the control point ground surface. A total of 65

linear crests were recorded at field sites in BBNP along the N-S trending 4 km long dike in

BBNP. BBNP linear crest orientations have a normal, slightly skewed distribution, favoring

orientations between 95° and 125° (Figure 3.3). Of measured linear crests, 46.2% (n = 30)

are oriented between 95° and 125°, 24.6% (n = 16) of orientations are between 0° and 95°,

and 29.2% (n = 19) are between 125° and 180°.
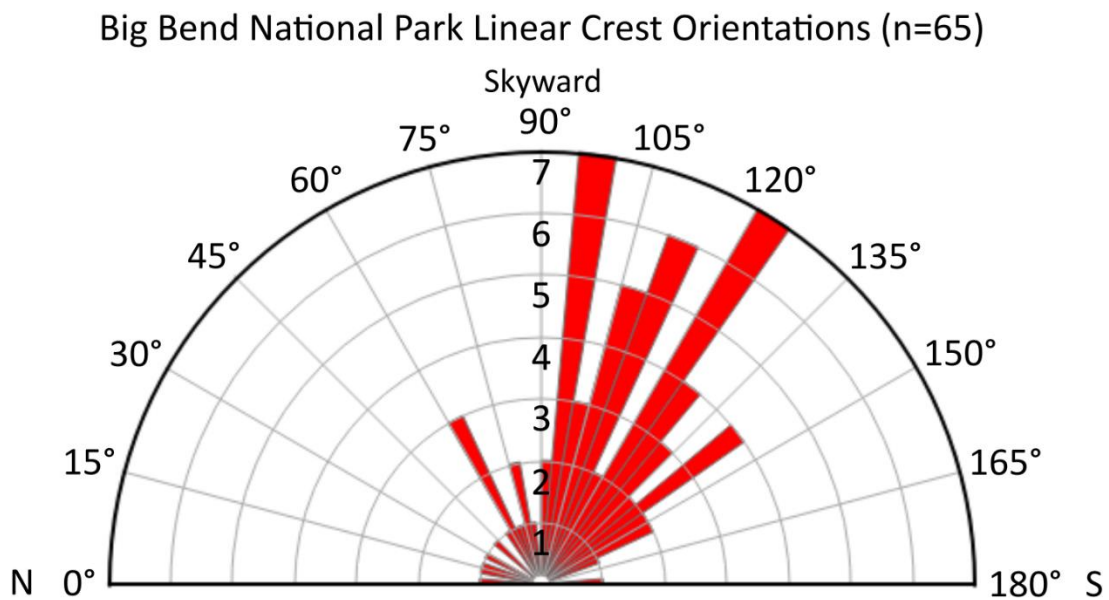
Figure 3.3 – A rose diagram displaying the orientations of linear structures at BBNP.
Measurements are shown grouped into 5° intervals. Note the clustered distribution between
95° and 125°.

A total of 24 linear crests were measured at 71 Gulch because all field sites are along the singular fissure structure. 71 Gulch linear crest orientations have a multimodal distribution, slightly favoring orientations between 0° and 20°, 60° and 80°, and 100° and 160° (Figure 3.4). 29.2% (n = 7) have measured orientations between 0° and 60°, 37.5% (n = 9) have measured orientations between 60° and 120°, and 33.3% (n =8) have measured orientations between 120° and 180°.
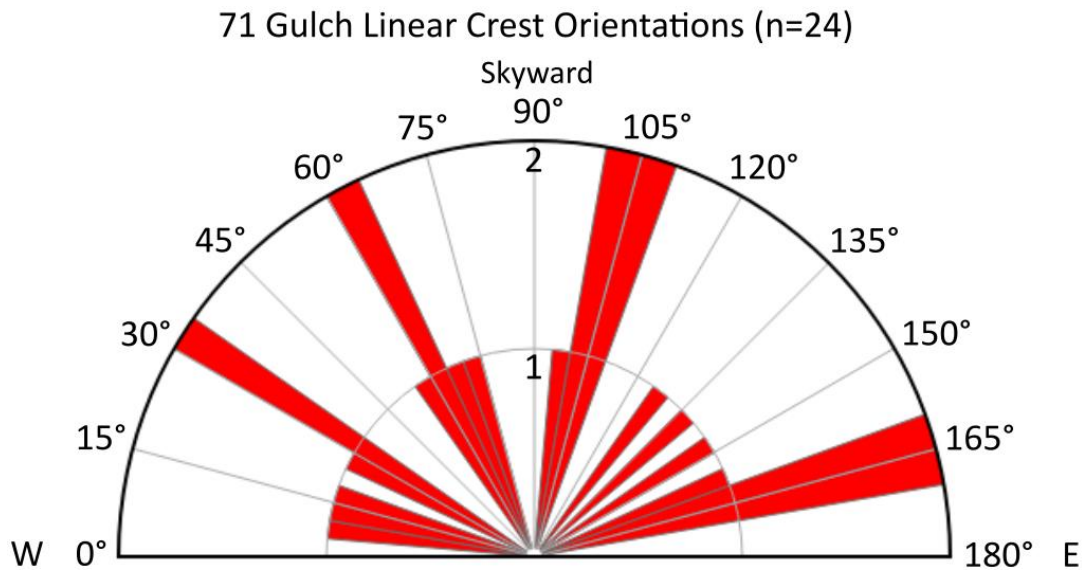
Figure 3.4 – A rose diagram displaying the orientations of linear structures at 71 Gulch. Measurements are shown grouped into 5° intervals. Note the more scatted distribution.

Magma Viscosity Calculations

A range of possible magma viscosities were calculated for three samples from BBNP and for five samples from 71 Gulch by processing 16 scenarios of varying water content and temperature were conducted for each sample (Table 3.3). The Magma Viscosity Calculator spreadsheet developed at Whitman College, after the methods of Shaw (1972), was used to calculate viscosity. Unnormalized weight percentages of oxides, using the loss on ignition percentage (LOI%) for H_2O content, and normalized weight percentages of oxides with

45

varying H_2O content (1%, 2%, and 3% weight) were analyzed with varying temperatures (900°C, 1000°C, 1100°C, and 1200°C).

Temperature had the greatest influence on calculated viscosity. At BBNP, calculated viscosities vary on the order of one or two orders of magnitude. Viscosities range from 78.3 Pa*s to 1400 Pa*s at 900°C, from 22.5 Pa*s to 305 Pa*s at 1000°C, from 7.78 Pa*s to 83.3 Pa*s at 1100°C, and from 3.1 Pa*s to 27.1 Pa*s at 1200°C. At 71 Gulch, in the perspective of changing temperature, vary on the order of just one order of magnitude. Viscosities range from 12.7 Pa*s to 259 Pa*s at 900°C, from 4.36 Pa*s to 66.6 Pa*s at 1000°C, from 1.74 Pa*s to 20.9 Pa*s at 1100°C, and from 0.79 Pa*s to 7.64 Pa*s at 1200°C.

In the perspective of water content, at BBNP, viscosities vary on the order of just one order of magnitude. The maximum difference in viscosity across varying water content at BBNP is between 144 Pa*s to 1400 Pa*s in sample 2016DD at 0.57% H_2O (reported LOI) and 3% H_2O (high-order value of varying H_2O content), respectively. At 71 Gulch, viscosities also vary on the order of just one order of magnitude. The maximum difference in viscosity across varying water content at BBNP is between 12.7 Pa*s and 259 Pa*s in sample KB030 at 1% H_2O and 4.84% H_2O (reported LOI), respectively.

Within the more realistic temperature regime of 1100°C, 71 Gulch magmas are overall less viscous than at BBNP. The estimated average viscosity across varying water content is calculated to be 31.6 Pa*s at BBNP and 7.5 Pa*s at 71 Gulch. In relation to the viscosity of lobate textures in basalt, whose textures are like those of billowed structures, these viscosities are realistic and fall within the range of viscosities for basalts with a flow rate of 0.1-1.0 m^3/s which cool to preserve lobate textures (Gregg and Fink, 1995).

Table 3.3 – Magma viscosities calculated utilizing methods of Shaw (1972) at varying water content and temperature.

A)

	Viscosity (Pa*s) - Unnormalized wt % (LOI % for H$_2$O)			
Sample ID	**900 °C**	**1000 °C**	**1100 °C**	**1200 °C**
09-008	78.3	22.5	7.78	3.1
09-025	443	108	32.4	11.4
2016DD	1400	305	83.3	27.1

E)

	Viscosity (Pa*s) - Unnormalized wt % (LOI % for H$_2$O)			
Sample ID	**900 °C**	**1000 °C**	**1100 °C**	**1200 °C**
KB011b	18.1	6	2.33	1.03
KB024	46.8	14.1	5.09	2.1
KB030	12.7	4.36	1.74	0.79
KB055	13.2	4.51	1.8	0.813
KB078	70.2	20.4	7.11	2.86

B)

	Viscosity (Pa*s) - Normalized wt. % (1% H$_2$O)			
Sample ID	**900 °C**	**1000 °C**	**1100 °C**	**1200 °C**
09-008	806	186	53	17.9
09-025	591	140	41.1	14.2
2016DD	894	204	57.7	19.4

F)

	Viscosity (Pa*s) - Normalized wt. % (1% H$_2$O)			
Sample ID	**900 °C**	**1000 °C**	**1100 °C**	**1200 °C**
KB011b	89.1	25.3	8.65	3.42
KB024	148	40.1	13.1	5.01
KB030	259	66.6	20.9	7.64
KB055	209	54.8	17.5	6.49
KB078	166	44.4	14.4	5.45

C)

	Viscosity (Pa*s) - Normalized wt. % (2% H$_2$O)			
Sample ID	**900 °C**	**1000 °C**	**1100 °C**	**1200 °C**
09-008	311	78.4	24.2	8.75
09-025	234	60.6	19.1	7.07
2016DD	339	85	26	9.36

G)

	Viscosity (Pa*s) - Normalized wt. % (2% H$_2$O)			
Sample ID	**900 °C**	**1000 °C**	**1100 °C**	**1200 °C**
KB011b	41.1	12.6	4.58	1.91
KB024	65.6	19.2	6.72	2.71
KB030	109	30.5	10.3	3.99
KB055	90.1	25.6	8.73	3.45
KB078	72.7	21.1	7.32	2.93

D)

	Viscosity (Pa*s) - Normalized wt. % (3% H$_2$O)			
Sample ID	**900 °C**	**1000 °C**	**1100 °C**	**1200 °C**
09-008	133	36.5	12.1	4.63
09-025	102	28.8	9.71	3.8
2016DD	144	39.1	12.8	4.9

H)

	Viscosity (Pa*s) - Normalized wt. % (3% H$_2$O)			
Sample ID	**900 °C**	**1000 °C**	**1100 °C**	**1200 °C**
KB011b	20.6	6.73	2.59	1.13
KB024	31.7	9.95	3.7	1.57
KB030	50.8	15.2	5.45	2.24
KB055	42.6	13	4.71	1.96
KB078	34.9	10.9	4.00	1.69

Note: A-D show geochemistry samples from BBNP. E-H show geochemistry samples from 71 Gulch. A and E utilize unnormalized oxide weight percentages, B-D and F-H utilize normalized oxide weight percentages. Highlighted in orange are the viscosities associated with 1100°C, the temperature regime which is most likely to reflect natural conditions of these samples.

Density and Lithostatic Pressure Estimates

Host Sediment Density and Lithostatic Pressure

Rock density and lithostatic pressure estimates for the Javelina and Black Peaks formations at BBNP and the Glenns Ferry formation at 71 Gulch are shown in Table 3.4. The Javelina and Black Peaks formations unsaturated densities estimated by Martin (2007) are similar, 2.24 g/cm^3 and 2.27 g/cm^3, respectively. For saturated density at BBNP, densities ranged from 2.38g/cm3 to 2.53 g/cm3 (15% porosity) for the Javelina Formation and 2.42 g/cm3 to 2.57 g/cm3 (30% porosity) for the Black Peaks formation. The estimates for both unsaturated and saturated densities are assumed to be inflated from the time of magma intrusion as the unsaturated sediment densities for each formation are derived from modern day data and saturated sediment density utilizes high-end value of 30% porosity to incorporate the density of water. For the 71 Gulch Glenns Ferry formation, unsaturated density estimates from three samples ranged from 1.48 g/cm^3 to 1.72 g/cm^3 with a mean density of 1.60 g/cm^3. Saturated densities ranged from 1.76 g/cm^3 to 2.02 g/cm^3 with a mean of 1.88 g/cm^3.

Utilizing equation (2), lithostatic pressure (MPa) was calculated using the appropriate host sediment densities (g/cm^3) and the estimated maximum depth of billowed structure formation, 500 m for BBNP and 24 m for 71 Gulch.

Table 3.4 – Density and lithostatic pressure estimates of relevant host sediment formations

Grapevine Hills, BBNP Formation ID	Unsaturated Density (g/cm³)	Saturated Density at 15% Porosity (g/cm³)	Saturated Density 30% Porosity (g/cm³)	Pressure at 500 m depth (MPa)
Javelina Formation	2.23	2.38	2.53	10.94
Black Peaks Formation	2.27	2.42	2.57	11.13

Glenns Ferry Fm., 71 Gulch Sample ID	Unsaturated Density (g/cm³)	Saturated Density at calculated porosity (g/cm³)	Pressure at 24 m depth (MPa)
KB008	1.48	1.76	0.35
KB050	1.72	2.02*	0.41
KB051	1.60	1.86	0.38

Porosity percentage adjusted to 30%

Note: BBNP densities are estimated from modern day conditions. Densities are assumed to have been lower due to the sediment being unlithified and groundwater-rich at the time magma intruded. Also, pressure estimates were calculated using the maximum of the range of the depths at each locality.

Magma Density

Hydrous and anhydrous magma density estimates from three BBNP samples and five 71 Gulch samples were calculated utilizing unnormalized whole rock oxide weight percentages, estimated lithostatic pressures from corresponding strata and a temperature of 1100°C (Table 3.5). BBNP hydrous magma has a mean density of 2.64 g/cm³ with a standard deviation of 0.05 g/cm³; anhydrous magma has a mean density of 2.77 g/cm³ with a standard deviation of 0.04 g/cm³. 71 Gulch hydrous magma has a mean density of 2.70 g/cm³ with a standard deviation of 0.05 g/cm³; anhydrous magma has a mean density of 2.96 g/cm³ with a standard deviation of 0.03 g/cm³.

Table 3.5 – Magma density estimates of BBNP and 71 Gulch basalt samples

BBNP Magma Densities at 1100°C/500 m depth (g/cm3)

Sample ID	Hydrous	Anhydrous
09-008	2.58	2.82
09-025	2.67	2.76
2016DD	2.68	2.72
Mean	2.64	2.77

71 Gulch Magma Densities at 1100°C/24 m depth (g/cm3)

Sample ID	Hydrous	Anhydrous
KB011b	2.74	2.98
KB024	2.72	2.94
KB030	2.63	2.99
KB055	2.65	2.99
KB078	2.76	2.91
Mean	2.70	2.96

Comparison

When comparing the saturated densities of sediment to relevant magma densities, magma has a greater density in all scenarios. The greatest saturated density of BBNP sediment is 2.57g/cm^3, compared to a mean hydrous magma density of 2.64 g/cm^3. In this case, the saturated density of the sediment in BBNP is assumed to be inflated from the actual density during the time of magma intrusion. The greatest saturated density of 71 Gulch is 2.02 g/cm^3, compared to a mean hydrous magma density of 2.70 g/cm^3.

Big Bend National Park

N-S Trending Dike

Southern Section

One sample of the intrusion interior and one sample of the intrusion margin were collected for petrographic analysis from the southern portion of the 4-km-long N-S trending intrusion. In hand sample, the intrusion interior sample (AJG-002-1) is medium-to-dark gray coherent porphyritic basalt. Plagioclase phenocrysts up to 5 mm long are set in a medium-to-dark gray microcrystalline matrix. In thin section (Figure 3.5), 50-60% subhedral plagioclase microlite laths, 5% subhedral oxide microlites, 2-5% anhedral clinopyroxene microlites, and scarce euhedral 1 mm long phenocrysts of olivine are observed in a hyalopilitic groundmass of sideromelane. The smaller plagioclase laths are oriented parallel to dike orientation. Some larger phenocrysts and glomerocrysts of plagioclase, 1-5 mm long, and equant and elongate subhedral oxides, up to 1 mm wide, are present. Vesicles were not observed in this sample.

Figure 3.5 – Cross polarized photomicrograph representing the intrusion interior at AJG-002. The preferred orientation of plagioclase crystals is parallel to dike orientation.

In hand sample, the sample of intrusion margin from the south end of the intrusion (AJG-001-1) is dark-gray microcrystalline groundmass in contact with yellow-tan to white very fine-grained sediment with small veins of calcite present. Elongated vesicles oriented parallel to billowed troughs in areas where the outermost glassy margin is well preserved (Figure 3.6). In thin section (Figure 3.7), the outer-most edge of the glassy intrusion margin consists of about 10% subhedral plagioclase microlite laths and 10% subhedral oxide microlites. Laths occur in a groundmass of sideromelane with 10% vesicularity. Vesicles are elongate and oval in shape and secondary minerals of zeolite and calcite fill most void spaces with small veins of calcite up to 0.5 mm in wide also present. Elongate vesicles and

plagioclase laths show preferred orientation parallel to dike margin. The sedimentary component adhered to the exterior of the intrusion consists of 20-30% fine-grained angular clasts of plagioclase, oxides, and calcite in a very fine-grained matrix and calcite cement. Calcite veins up to 1 mm wide are common.

Figure 3.6 – Field photo taken at AJG-001 in BBNP showing elongated vesicles preserved within the glassy margins of the southern portion of the N-S trending intrusion. Small 3-5 mm long vesicles can be seen within the green ellipses on the figure. Note the elongated vesicles are generally oriented parallel to billow troughs which are located on the top-left and right side of the figure. Measuring stick minor tick marks are in millimeter interval.
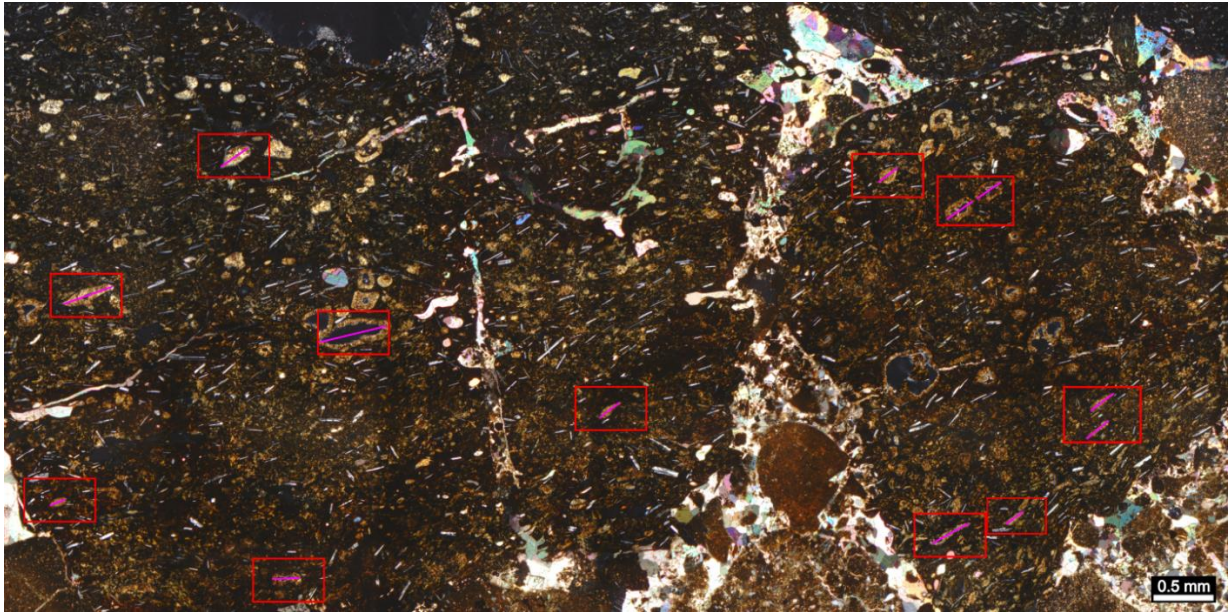
Figure 3.7 – Cross polarized photomicrograph of the margin of AJG-001. Elongate vesicles are indicated by red boxes and the orientation of their major axis indicated by a magenta line. The elongate vesicles and plagioclase laths show preferential orientation parallel to the orientation of the dike margin.

Northern Section

Hand samples of intrusion margin (AJG-012-1A, AJG-012-1B, and AJG-017-1) are aphanitic and light brown to light tan in color with circular to elongate vesicles. Calcite and some brown to white fine-grained sediment fill vesicles up to 5 mm wide. Elongate vesicles are oriented parallel to billowed troughs (Figure 3.8). In thin section, the mineralogy of the samples is similar. They consist of 5-20% subhedral microlite laths of plagioclase and <5% anhedral oxides set in an intersertal groundmass of sideromelane with 15-25% vesicularity. Some larger phenocrysts and few glomerocrysts of plagioclase similar in size, 0.5-1.5 mm in diameter, are present. Plagioclase laths have a slight preferred orientation parallel to orientation of the dike margin in samples AJG-012-1A (Figure 3.9) and AJG-012-1B, but are randomly oriented in AJG-017-1. Small vesicles, <0.05 to 0.6 mm in diameter, are rimmed

54

and sometimes filled by fibrous zeolite. Calcite amygdules 0.4 to 3.0 mm in diameter are also present. In AJG-012-1B, a circular sedimentary lithic, approximately 2 mm in diameter, is present approximately 2 mm from the exterior margin consisting of fine-grained angular fragments of plagioclase, angular quartz, and subrounded calcite in a matrix of clay and some sideromelane with smaller plagioclase laths oriented around it (Figure 3.9). Near the sedimentary lithic, a plagioclase glomerocrysts, approximately 1 mm wide, is present approximately 1 mm from the exterior margin. Also, in sample AJG-012-1A the outer, most exterior portion of the margin is composed of a lighter brown colored palagonite and some sideromelane which grades to opaque tachylyte glass, then grades to a more plagioclase abundant groundmass moving inwards (Figure 3.10).

Figure 3.8 – Field photo taken near AJG-012 and AJG-013 in BBNP showing elongated vesicles preserved within the glassy margins of the northern portion of the N-S trending intrusion. Small 2-8 mm long vesicles can be seen around and above the measuring stick. Note the elongated vesicles are generally oriented parallel to billow troughs which are located on the left and right side of the figure. Measuring stick minor tick marks are in millimeter interval.

Figure 3.9 – Cross polarized photomicrograph of the exterior margin of AJG-012-1B. The dike margin is seen along the bottom of the figure. A circular sedimentary lithic, approximately 2 mm in diameter, can be seen near the center of the figure. Note the small plagioclase laths in the groundmass and elongated vesicles generally oriented parallel to the exterior of the clast. A 1 mm wide plagioclase glomerocrysts can also be seen to the right of the figure, near the exterior margin of the sample.
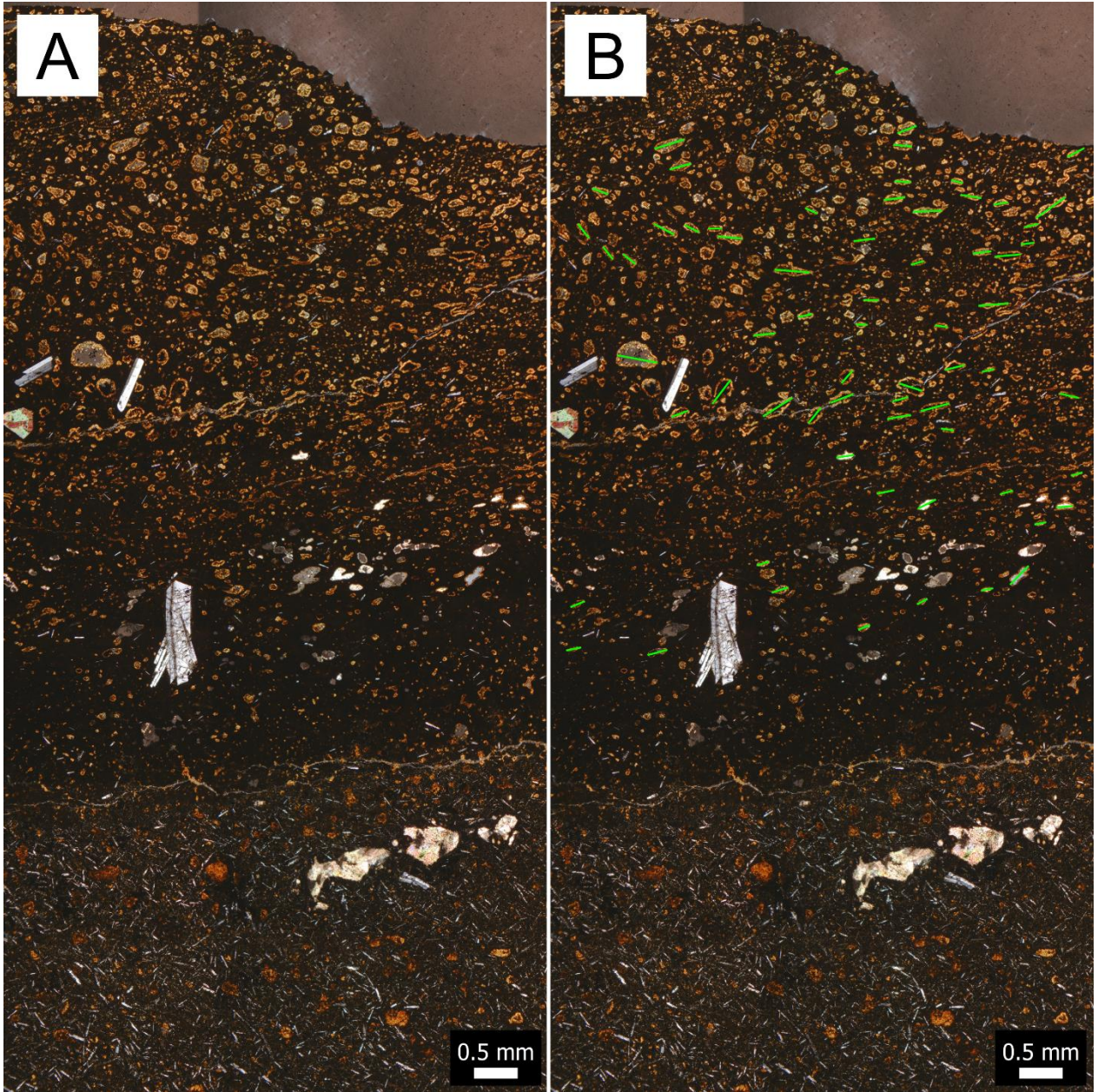
Figure 3.10 – A) and B) are the same cross polarized photomicrograph of the margin of AJG-012-1A. The dike margin is seen at the top of the figures. A) provides a non-annotated view of the phases of transitional glass. Circularity of vesicles, the density of the glass groundmass, and abundance of plagioclase increases away from the margin of sample. B) provides an annotated view with green lines indicating the orientation of the major axis of elongated vesicles.

Study Butte Area Intrusion

One sample of the intrusion interior (AJG-007-1) was collected and used for petrographic description. In hand sample, AJG-007-1 is a light gray to brown aphanitic basalt with no vesicularity. In thin section (Figure 3.11), AJG-007-1 is sample consists of 55% anhedral to subhedral microlite laths of plagioclase, 10% anhedral microlites of oxide, and 5-10% anhedral microlites clinopyroxene in a hyalopilitic groundmass of sideromelane. Some larger phenocryst laths of plagioclase, up to 1.5 mm long, are present. A poikilitic texture is observed with plagioclase surrounded by or included in larger clinopyroxene. There is no preferred crystal orientation in this sample.
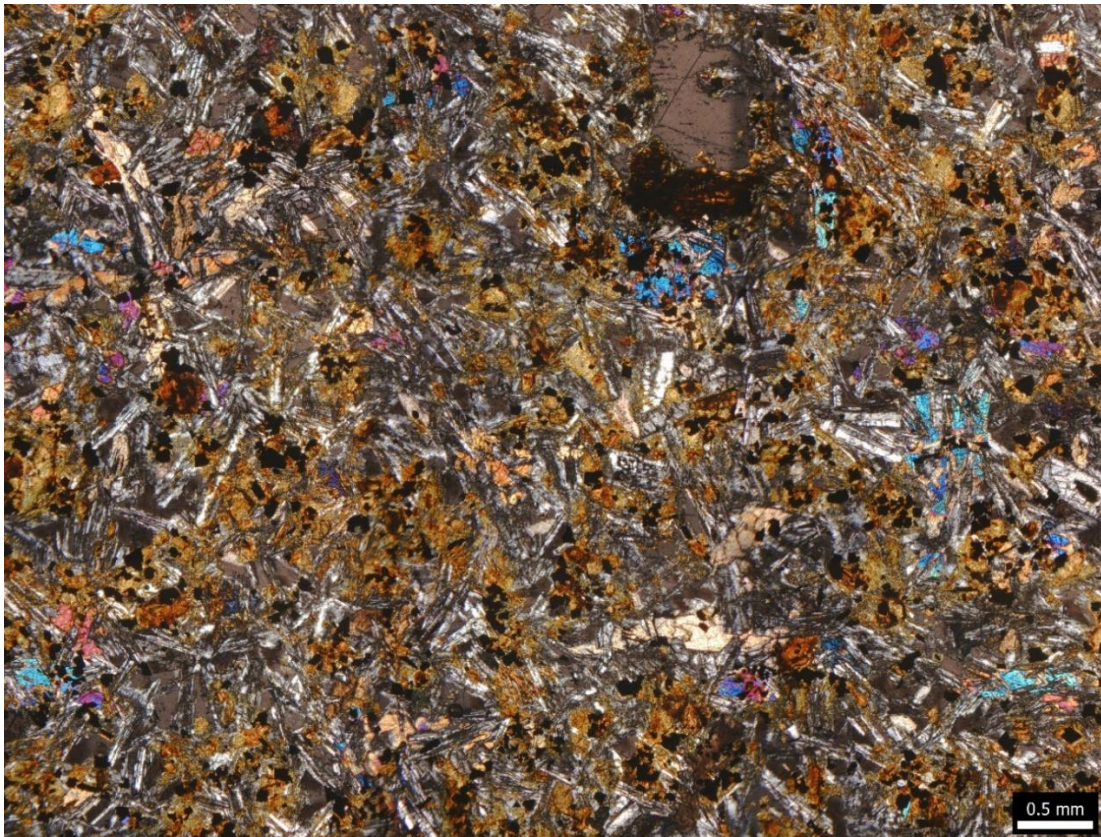
Figure 3.11 – Cross polarized photomicrograph representing the intrusion interior at AJG-007. There is no preferred crystal orientation in this sample. A larger amount of glass and slightly larger percentage of oxides and clinopyroxene are present in comparison to the intrusive interior of AJG-002.

71 Gulch

Five thin section samples (KB011b, KB030bb, KB030bc, KB036, and KB061a) were used for petrographic description, shared by Kadie Bennis from her thesis work in 2018. In hand sample, KB011b and KB061a are similar. Both are light to dark gray aphanitic basalts with moderate vesicularity, larger vesicles measure up to 1 mm in diameter. KB036 in hand sample consists of a light tan quartz sandstone hosting light to dark gray aphanitic basalt with moderate vesicularity of vesicles up to 1 mm in diameter, forming a blocky peperite.

In thin section, samples KB011b, KB036 (Figure 3.12A), and KB061a (Figure 3.12B) consist of 40-45% subhedral plagioclase microlites and 5-15% anhedral to euhedral clinopyroxene microlites in a tachylyte groundmass with 15-30% vesicularity. Vesicles measure 0.2-1.0 mm in diameter, most are partially rimmed or filled by secondary minerals, except in KB-061a where vesicles are void of or have very thin portions rimmed with secondary minerals. Glomerocrysts of plagioclase are also present measuring 0.4-3.5 mm in width. Neither vesicles nor crystals have a preferred orientation. Sediment is present in KB036 filling cracks in the basalt, consisting of angular glass shards, microcrystalline sedimentary lithics, subrounded quartz, and subrounded to subangular plagioclase.

In thin section, KB030bb (Figure 3.13A) and KB030bc (Figure 3.13B) consist of 10-20% euhedral to subhedral plagioclase microlites and 5% subhedral clinopyroxene in a groundmass of tachylyte and sideromelane, where sideromelane is in direct contact with the host sediment. Host sediment primarily consists of quartz with some plagioclase and sedimentary lithics. In both samples, vesicles are approximately 0.1-0.5 mm in diameter are present and display elongation in KB030bb. Plagioclase laths and elongated vesicles along

60

the tachylyte-sideromelane contact are preferentially oriented parallel to the margin of the intrusion.
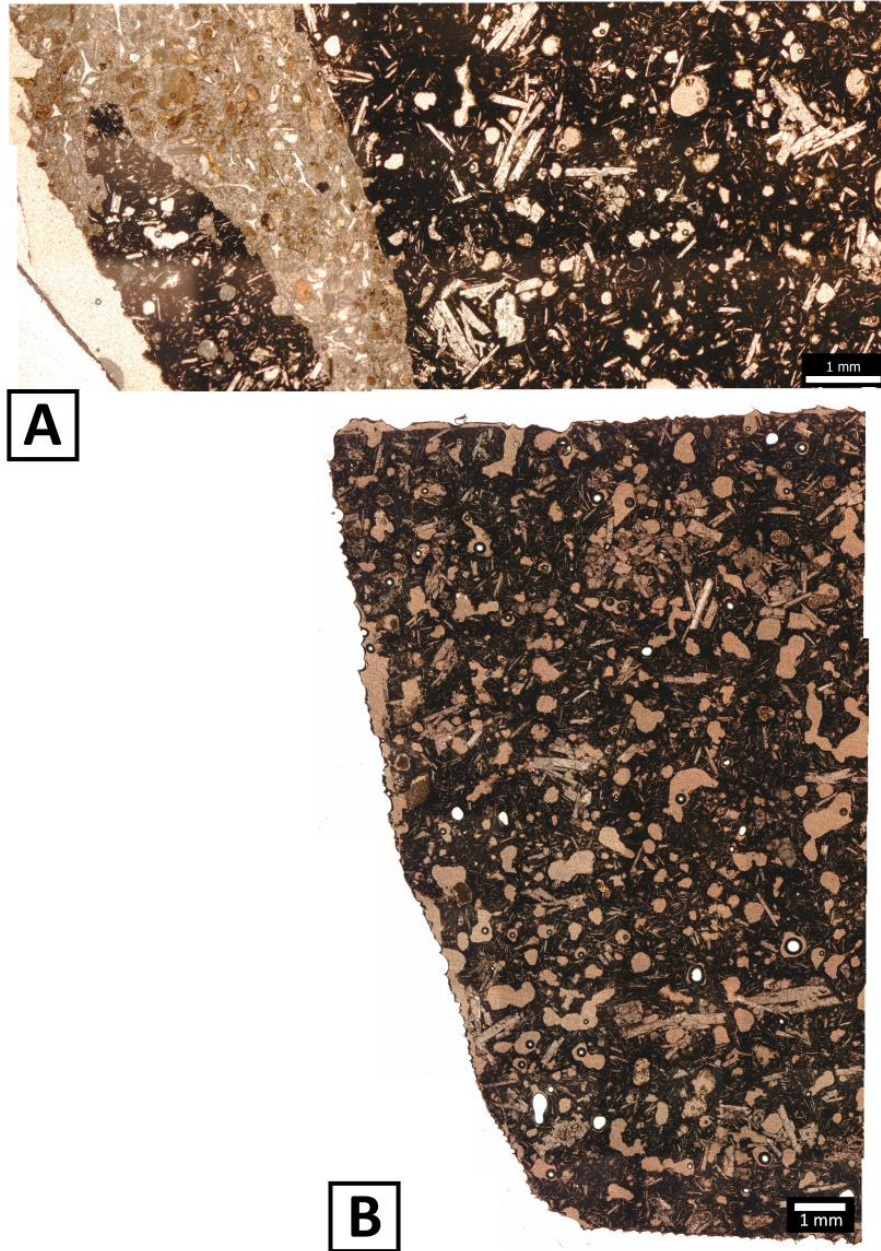
Figure 3.12 – Plain polarized photomicrographs of the intrusion margins of samples KB036 (A) and KB061a (B). The margin of the dike is seen on the left side of the figures. In A), a clear contact between light tan sediment and the darker tachylyte glass can be seen. B) does not exhibit sediment in contact with tachylyte and has many vesicles throughout. B) is also representative of thin section KB011b, however vesicles are often filled with secondary minerals in KB011b. Note that in both A and B, there are no elongated vesicles with preferred orientation or preferential orientation of plagioclase crystals.
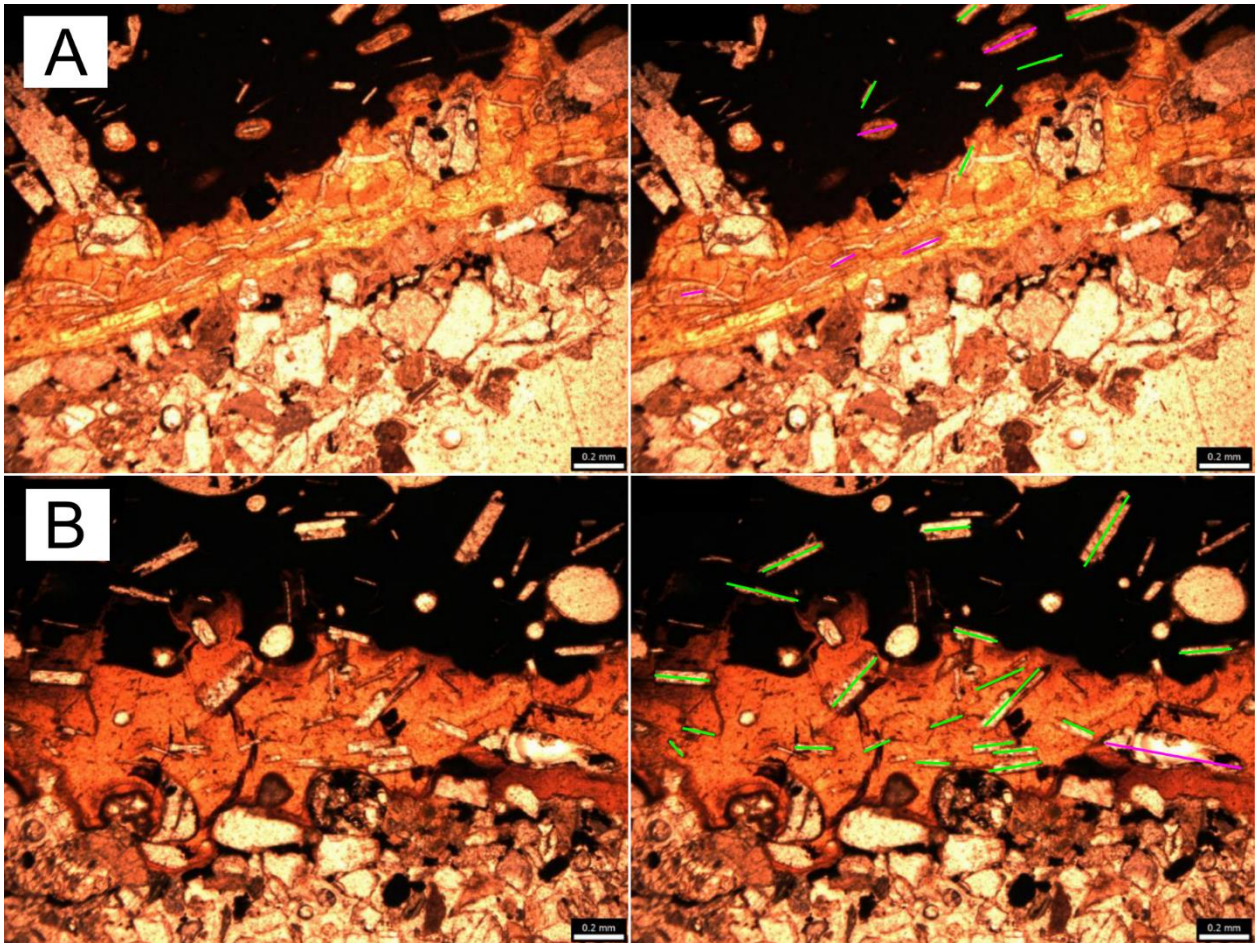
Figure 3.13 – Plain polarized photomicrographs of the intrusion margins of samples KB030bb (A) and KB030bc (B). Figures A and B contain the photomicrograph image and annotated image of the samples. In the annotated image, green lines represent the orientation of plagioclase laths and pink lines represent the orientation of elongated vesicles. In all images a clear contact can be distinguished between the black tachylyte glass in the top portion of the figures and the lighter brown sideromelane in the middle portion of the images. In the bottom portion of the images, sediment can be seen contacting sideromelane. Note the preferred orientation of plagioclase laths and elongate vesicles generally oriented parallel to the intrusion margin. Modified photo from Bennis (2019).

Geochemistry

Big Bend National Park

XRF and ICP-MS bulk whole rock geochemistry analysis of one sample from the N-S trending intrusion (2016DD (2016)) and two samples (09-008 (2010) and 09-025 (2010)) from nearby intrusive features were shared by Dr. Richard Hanson of Texas Christian University and his colleagues (Figure 3.14).

Variation in major element oxide weight percentages for samples 2016DD, 09-025, and 09-008 is low; 49.47, 48.92, and 49.79 weight percent SiO_2, respectively. Plotting total alkalis versus silica, samples 2016DD and 09-025 plot high in alkalinity for basalt, falling into the trachybasalt range. Sample 09-008 has slightly high alkalinity, plotting as a basaltic trachyandesite, near the boundaries of trachybasalt, tephrite, and phonotephrite (Figure 3.16).

Because alkalis are particularly susceptible to low temperature alteration and low temperature alteration is common in the BBNP region, rock classification used methods of Winchester and Floyd (1977) and the modified version by Pearce (1996) to plot values of more immobile elements (Zr/TiO_2 against Nb/Y) (Figures 3.17 and 3.18). In both methods, 2016DD, 09-008, and 09-025 plots overlap within the range of alkali basalt. Multi-element plots of incompatible trace elements show the similarity between samples with slight variation in cesium between the 09-008 and 09-025 samples and the 2016DD sample (Figure 3.19). Samples closely resemble the Sun and McDonough (1989) pattern for oceanic alkali basalt.
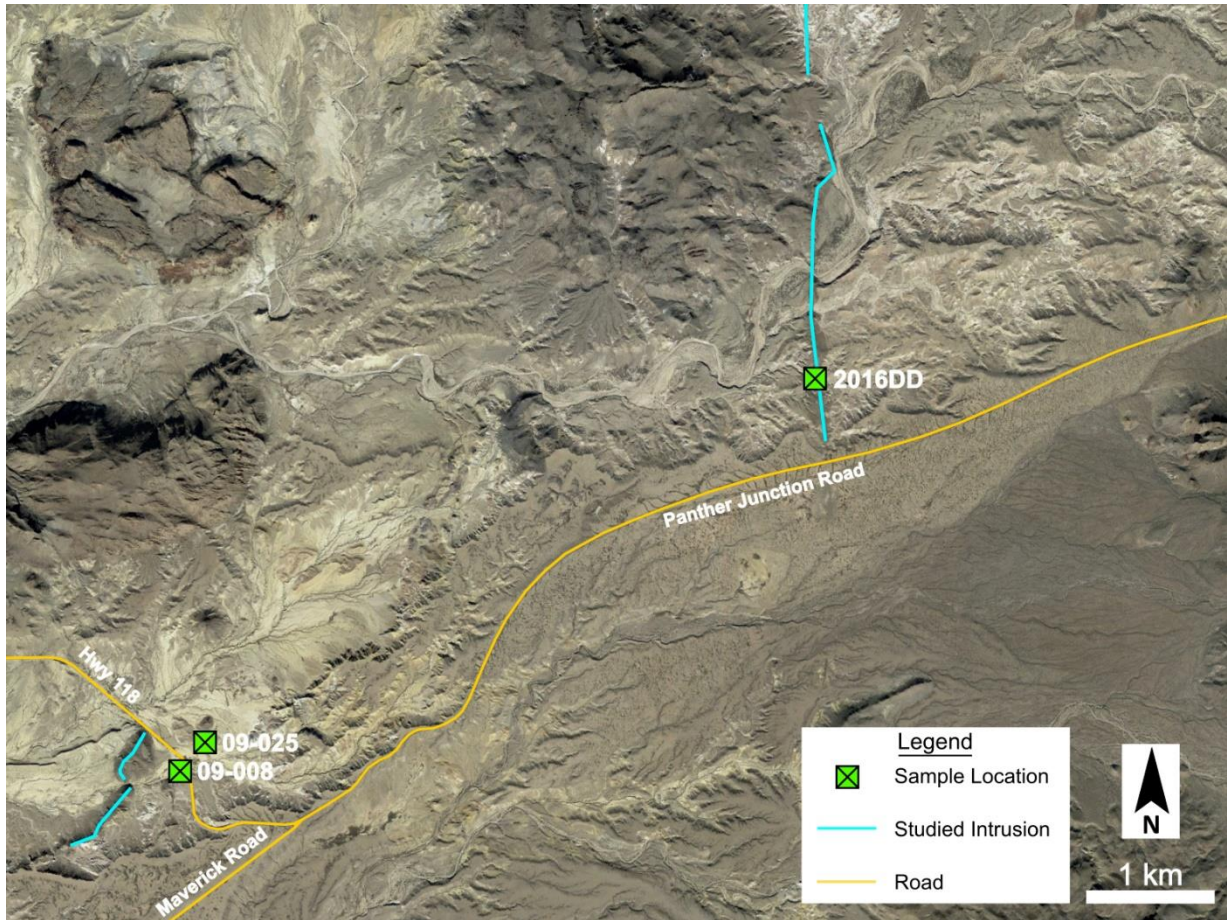
Figure 3.14 – Location map of geochemistry samples from West Big Bend National Park. The blue Studied Intrusion line highlights the general trend of the studied intrusions.

71 Gulch

XRF and ICP-MS bulk whole rock geochemistry analysis of five samples from 71 Gulch (KB011b, KB024, KB030, KB055, and KB078) were shared by Kadie Bennis from her thesis work in 2018 (Figure 3.15). Variation in major element oxide weight percentages is low for all samples, with a slight increased variation in CaO by ~2.5% in sample KB011b. SiO_2 weight percentages are: 44.38 (KB011b), 46.03 (KB024), 47.10 (KB030), 46.90 (KB055), and 46.48 (KB078). Plotting the total alkalis versus silica results in a grouping within the range of basalt, except for KB011b which plots as a tephrite, near the boundaries

of basalt and picrobasalt (Figure 3.16). Discrimination diagrams after Winchester and Floyd (1977) and Pearce (1996) were also created for 71 Gulch samples due to observed alteration (Figures 3.17 and 3.18). A tight grouping among the samples is plotted within the range of basalt. Results for the samples in trace element analysis have low variation and closely resemble the Sun and McDonough (1989) pattern for oceanic alkali basalt (Figure 3.19).
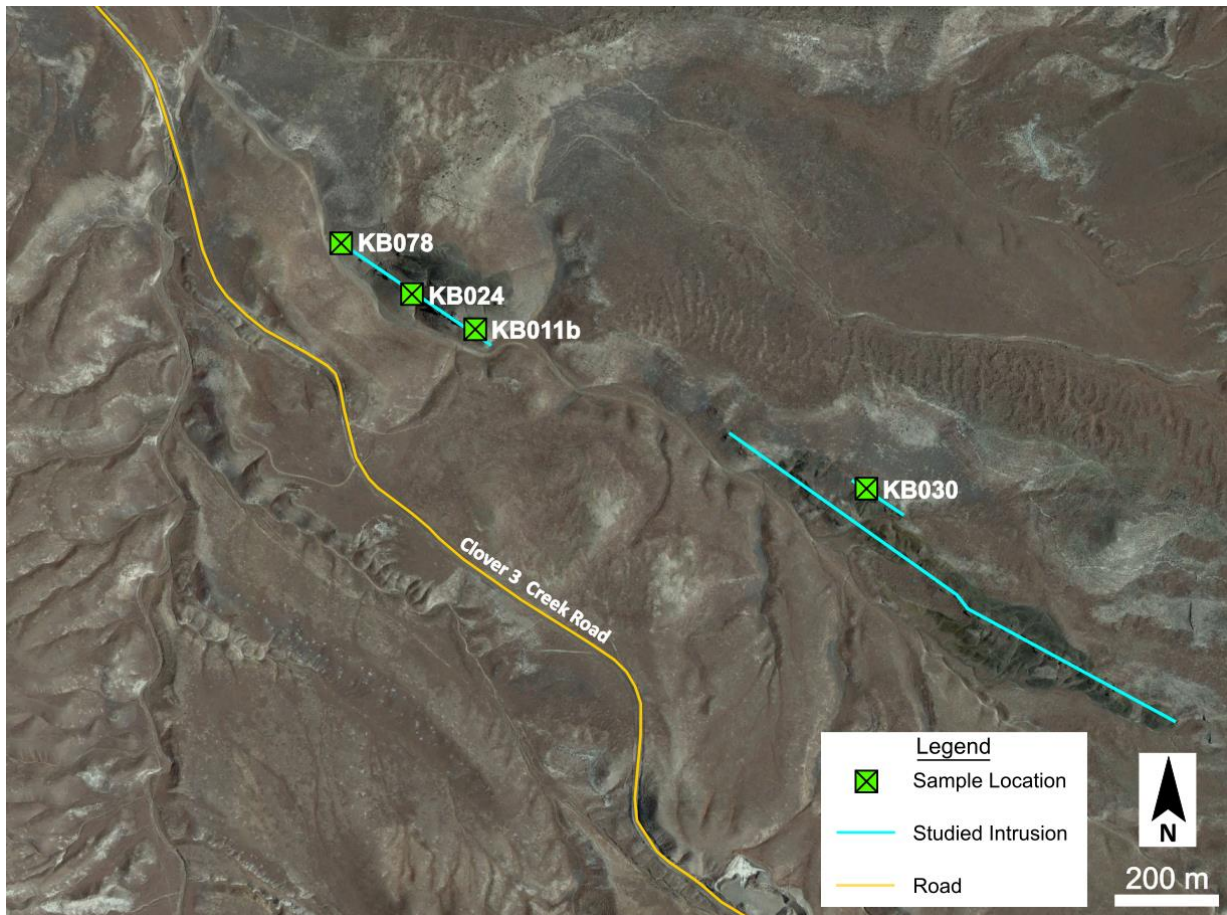
Figure 3.15 – Location map of geochemistry samples from 71 Gulch. The blue Studied Intrusion line highlights the general trend of the studied intrusions. KB055 excluded from the map due to error in GPS location point data.
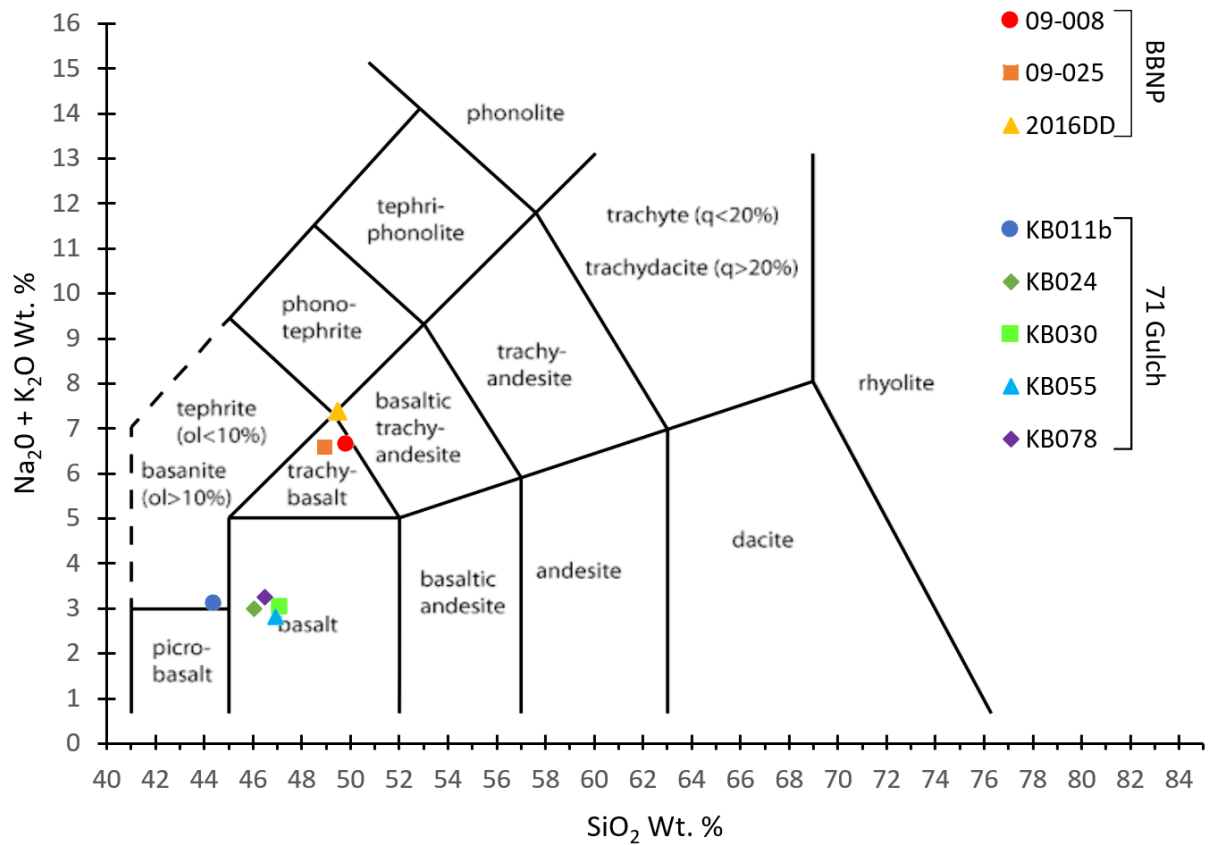
Figure 3.16 – TAS diagram showing the distribution of BBNP and 71 Gulch samples. BBNP samples plot as trachybasalt and basaltic trachyandesite. A majority of the 71 Gulch samples plot as basalt; only one sample plots as tephrite.
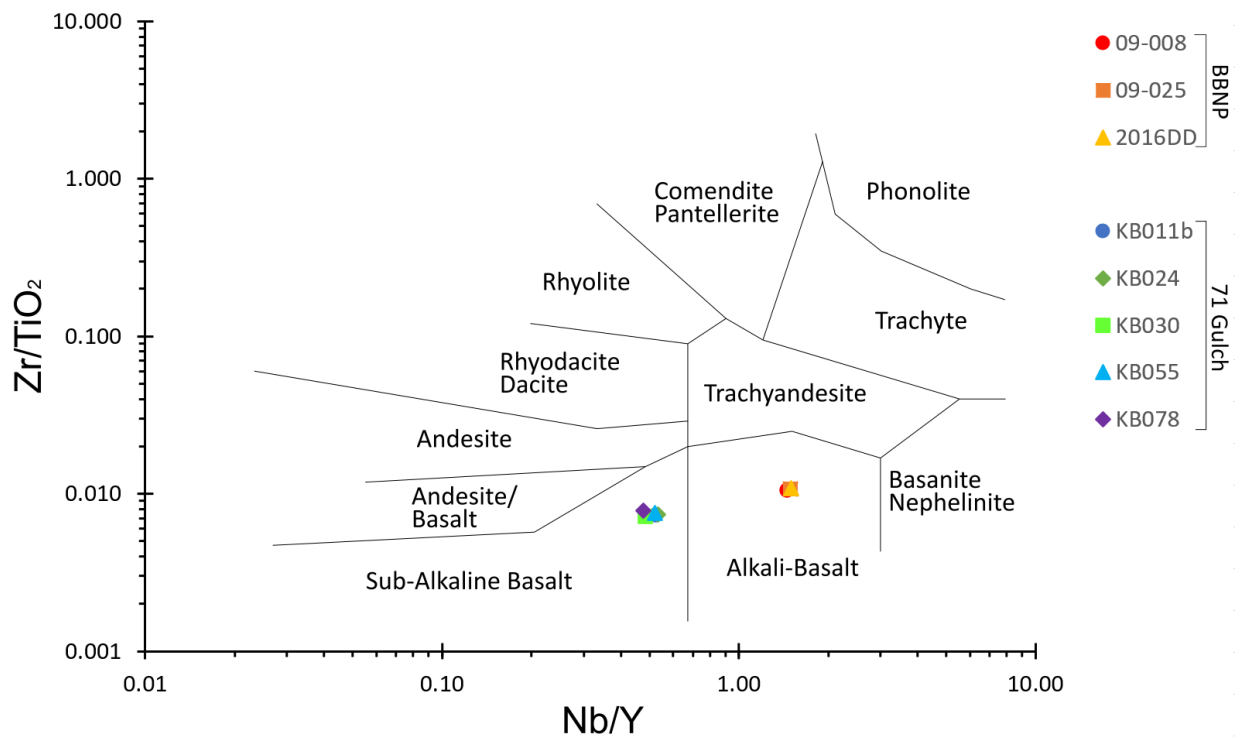
Figure 3.17 – Zr/TiO$_2$ versus Nb/Y discrimination diagram after Winchester and Floyd (1977). All BBNP samples plot as alkali-basalt and all 71 Gulch samples plot as sub-alkaline basalt.
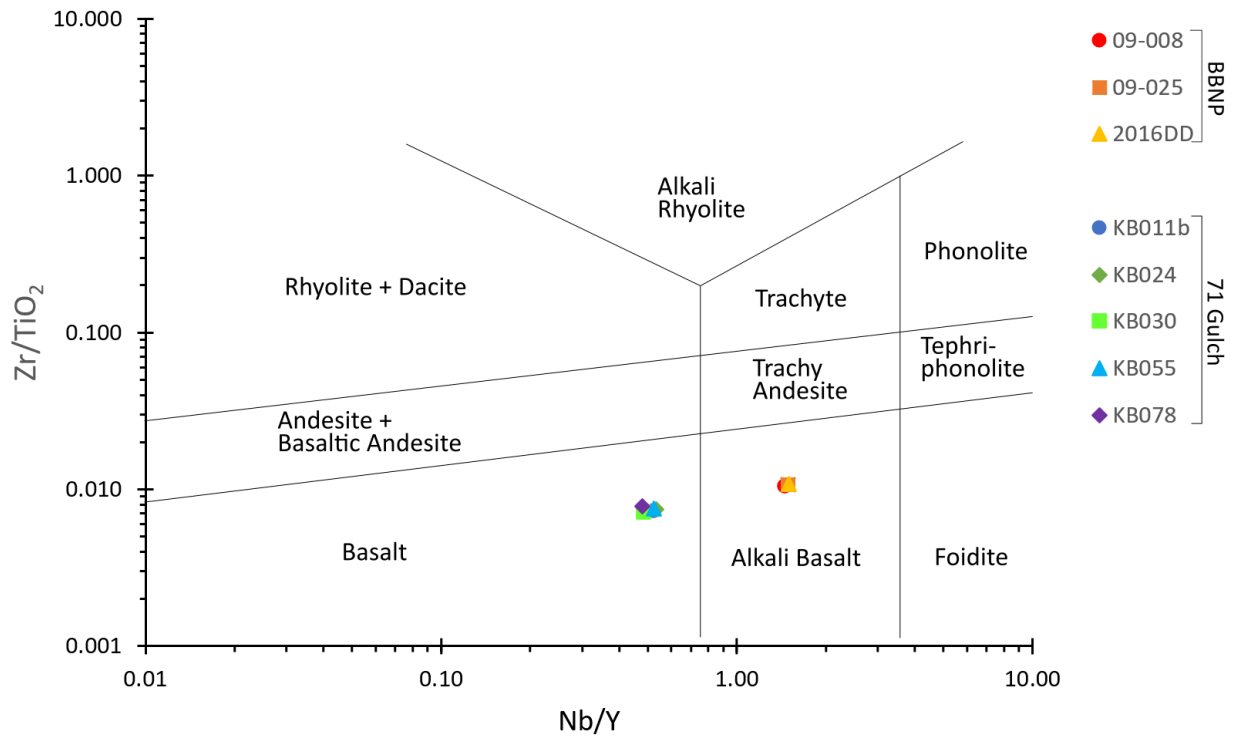
Figure 3.18 – Zr/Ti versus Nb/Y discrimination diagram from Pearce (1996). All BBNP samples plot as alkali-basalt and all 71 Gulch samples plot as basalt.
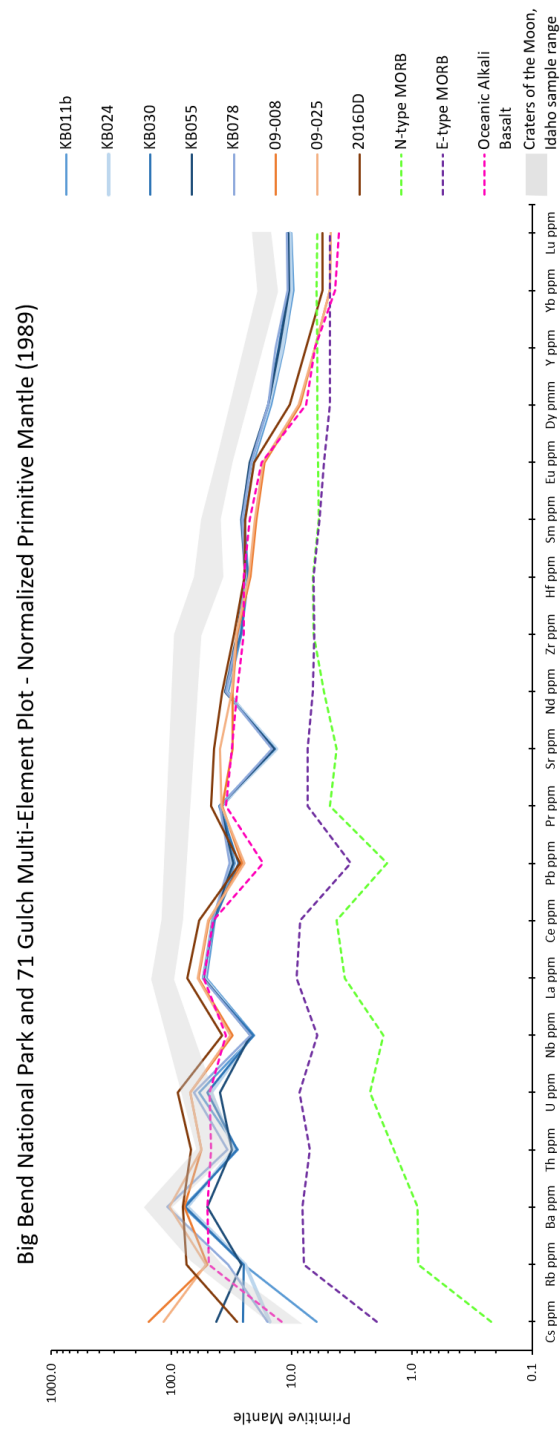
Figure 3.19 – Multi-element plot of five 71 Gulch samples and three Big Bend National Park samples. Samples are normalized to the primitive mantle (Sun and McDonough, 1989). Dashed lines represent patterns for moderately to highly incompatible elements in average N-type and E-type MORB and oceanic alkali basalts using values from Sun and McDonough (1989). The gray shaded region represents a range for basaltic lavas from Craters of the Moon, Idaho as an additional comparison for intraplate basalt. All samples closely correlate with the oceanic alkali basalt and Craters of the Moon basalt patterns.

CHAPTER 4: DISCUSSION

Big Bend National Park and 71 Gulch present two suitable localities to evaluate the characteristics and conditions in which billowed structures form. The presence of water at the time of magma intrusion is evident at both localities in the form of nearby desiccation cracks in sediment (BBNP), peperites (BBNP and 71 Gulch), phreatomagmatic deposits (BBNP and 71 Gulch), and transitional glass phases resembling the quench margins of pillow lavas (BBNP and 71 Gulch). Geochemical data of sampled intrusions show that both localities host OIB-like basalt which intruded through water-bearing sediments. From these similarities, we can begin to understand the characteristics that are common for billowed structures of a basaltic composition as they intrude into water-bearing sediments across more than one locality. The significant difference between the two localities is the depth in which the billowed structures formed below the pre-eruptive surface, 400-500 meters at Big Bend National Park (Befus et al., 2009) and ≤24 meters at 71 Gulch (Bennis, 2019). This provides an opportunity to compare characteristics of billowed structures formed at different depths with consideration for the host sediment lithostatic pressures and the availability of water.

Formation of Billowed Structures as a Result of Kelvin-Helmholtz Instability

Billowed structures preserved along the margins of intrusions are wave-like structures which indicate a complex non-explosive interaction at the interface between molten basalt and water-bearing sediments. The initial formation of billowed structures is likely the result of Kelvin-Helmholtz instability between at the magma and water-bearing sediment interface before any significant cooling of the intrusion. Kelvin-Helmholtz instability typically occurs when there is velocity shear in a fluid due to differing velocities between the interface of two

fluids of differing densities (Drazin, 2015). Because of this shear, disturbance between the boundary of the two fluids begins to occur in the form of waves, such as when wind moves across the surface of water or interacts with clouds. As magma and water-bearing sediment interact, they behave as two fluids of differing densities (Buttner and Zimanowski, 1998; Skilling et al., 2002; Befus et al., 2009). From calculating estimates of saturated sediment density and magma density from both localities, the two mediums have distinctly different densities, Magma is consistently denser than the saturated sediment, even in the case of BBNP where estimates of unsaturated sediment density and porosity utilize higher-order values.

The velocity shear between the two mediums as magma was intruding is likely the biggest influencer of billowed structure geometry. As magma intruded through water-bearing sediments of BBNP and 71 Gulch, it did so at a high velocity. From modelling of other basaltic intrusions, the magma likely intruded at a velocity ranging between 0.5-1 m/s (Einarsson and Brandsdottir, 1980; Wilson and Head, 1981; Gudmundsson, 1984; Wilson and Head, 2002), creating shear between at the interface of the two fluids. Shortly after the development of the waves, or billows, at the magma and water-bearing sediment interface, the outer margin of the intrusion began to cool quickly, as evidence from the glassy margins, preserving the billowed structures along the cooled intrusion margin. The different geometries of billowed structures identified in this study may then preserve different morphologic segments of this instability interaction.

Indications of Flow During Billow Formation

Thin Section Observations

Thin sections made from the intrusion margins at BBNP do not exhibit cracking along the glassy exterior margins, which would be present had the exterior margins of the intrusion experienced inflation. The orientation of elongated vesicles and plagioclase laths along the exterior of the glassy margin parallel to the dike margin is also observed indicating flow along the margins of the intrusion during billow formation (Figures 3.6, 3.8, 3.9, and 3.10). In field observation, preferentially oriented plagioclase phenocrysts were apparent on the interior of the thicker, southern portion of the N-S trending intrusion (AJG-002), where thickness was approximately 6 meters.

A sequence of glass, typical of quenched glass, is evident in thin section AJG-012-1A (Figure 3.10) from BBNP. Moving inwards from the margin of the intrusion, a transition from palagonite and sideromelane to denser tachylyte glass containing a denser groundmass of plagioclase is present. This transition is also evident in KB030 (Figure 3.13) where sediment is in contact with sideromelane, which then transitions to denser tachylyte glass. This transition is indicative of gradient cooling behavior as the outermost exterior cooled at a different rate than the margin just a few millimeters in, similar to the sequence of glass developed in quenched pillow margins (Melson and Thompson, 1973; Kawachi and Pringle, 1988). This indicates that there was sufficient pore water in the host sediment during the formation of billowed structures to cause similar quenching behavior as the margins of extrusive pillow lavas.

Additionally, in thin section AJG-012-1B (Figure 3.9), a large round lithic of sediment can be observed approximately 2 mm from the exterior margin of the sample with plagioclase and elongated vesicles oriented generally parallel to the surface of the lithic. This indicates that the lithic was quickly incorporated into the intruding magma before the outermost exterior margin of the intrusion began to solidify, suggesting that the intrusion, and therefore billowed structure formation, occurred rapidly. The lithic was then able to continue migrating within a flowing interior before it solidified in its final location. These factors combined suggest that magma quickly intruded, simultaneously forming billows along the margins of the intrusion, and, with the availability of ample pore water, the exterior margin of the intrusion rapidly cooled, preserving the billowed structures.

In some samples from 71 Gulch, sediment is observed in direct contact with tachylyte glass rather than palagonite or sideromelane in samples KB036 and KB061a, as seen in Figure 3.12. However, fragmentation of the magma is likely to have occurred in these samples, allowing for tachylyte glass to directly encounter sediment. Fragmentation was not evident in sample from BBNP. Samples KB030bb and KB030bc (Figure 3.13) preserve a boundary of sideromelane between host sediment and tachylyte, containing plagioclase laths preferentially oriented parallel to the intrusion margin. This suggests similar processes for billow structure formation occurred at 71 Gulch as did at BBNP.

Elongate Vesicles

Elongate vesicles were observed in multiple locations along the margins of the N-S trending intrusion in the field at BBNP (Figures 3.6 and 3.8). They were present in instances where the glassy margins of the intrusion were well preserved. Where elongate vesicles were

observed in the field, all were oriented parallel or sub-parallel to the billowed trough orientation and were observed to be approximately 0.2-1.0 cm in length. The preservation of elongate preferentially oriented vesicles within the glassy margins of the intrusion suggests that there was some degree of flow as the exterior margins cooled. While the elongate vesicles may not prove reliable for interpretation of flow direction as the orientation could be affected by factors such as thermal convection of the magma and buoyancy of the bubble (Peterson and Hawkins, 1971), they reflect that the melt was still fluid and deforming at the time of billow formation. The orientation of the vesicles is as complicated as the billows themselves suggesting local changes in flow because of the complex interaction along the magma-water interface.

Elongate vesicles were not observed in the field at 71 Gulch. Outcrops at 71 Gulch generally appear to be more weathered and it is possible that the outermost exterior of the margins had been eroded. However, elongate vesicles with preferred orientation parallel to the dike margin were recognized in thin section preserved in sideromelane from 71 Gulch.

Linear Crest Orientation

Figure 3.3 shows a preferred orientation of linear crests at BBNP along the N-S trending dike, whereas, in Figure 3.4, linear crests of 71 Gulch were more random. On average, linear crests are oriented 23° towards the south from skyward (0°). In 71 Gulch, 45.8% of the identified linear structures are oriented at an average of 45.9° west from skyward (0°), and 54.2% are oriented at an average of 40.6° east.

As mentioned in the previous section, elongate vesicles are parallel to the troughs of these structures. While linear crests resemble ropy textures that occur on tops of pahoehoe

flow, which are oriented perpendicular to flow direction (Fink and Fletcher, 1978), the orientation of elongate vesicles parallel to the linear billows suggests that billows are not simply the result of compressional folding as seen on pahoehoe flow surfaces. Therefore, using the orientation of linear crests as an indicator of main flow direction for the intrusion may prove to be unreliable, but may reflect more localized flow direction with simultaneous lateral expansion.

Billowed Structure Population and Geometry

Comparison of Billowed Structure Population

The population of different billowed structure types and scales does not vary significantly between BBNP and 71 Gulch, relative abundances of each structure type by <7% for each structure type between the two localities. When analyzing the relative distribution of structure types between sites and between field localities, they are quite similar (Tables 3.1 and 3.2). All billowed structure types are present at both localities. Bulbous, transitional, and linear structures, respectively, are the most identified structures across both localities. Sinuous, teardrop, and circular structures were identified in a slightly different order of percent abundance but were each <10% of the population at each locality. No one structure type is identified to be exclusive to a single site and all sites host at least three structure types (Figures 3.1 and 3.2). Of the 21 field sites across both localities, 10 host four of the six structure types. One site at each locality hosts all six structure types. Bulbous crests and transitional troughs are found at each site, but this is unsurprising due their less-orderly characteristics for classification compared to other structure classifications. No other structure type is consistently identified with another structure type.

75

Overprinted, Teardrop, and Circular Structures

Only two occurrences of overprinted structures were identified at BBNP and none were identified at 71 Gulch. While they were not accounted for in the population or dimension statistics, there presence is acknowledged. It is unclear as to why the presence of smaller scale structures appears to interrupt a repeating sequence of billowed structures to form an overprinted structure. It could be likely that the heterogeneity of grain size in host sediment caused a localized disturbance in the repeated billow formation as magma was flowing, generating a localized area of smaller structures to form. Teardrop and circular structures may also form from a similar process, where a localized area of sediment was less influenced by intruding magma to form a localized point depression, sometimes accompanied by a trough, on the intrusion surface. Large clasts were never observed trapped within the depressions or troughs of these structures, only fine-grained sediments of clay, silt, and sand, which suggest the likelihood of sediment heterogeneity being an influencing factor of their geometry.

Comparison of Billowed Structure Geometry

Across both localities, billowed structure dimensions do not vary significantly. While billowed structures of a given classification can vary on the order of a few centimeters to sometimes greater than one meter, when analyzing the mean wavelength and amplitudes crest and trough dimension, 71 Gulch billowed structures are within 2 cm larger in scale. Mean bulbous crest wavelength, sinuous crest wavelength, and teardrop trough amplitude and wavelength measurements are slightly larger at BBNP, but each are less than 6 cm in variation from 71 Gulch and are not consistently larger at one locality or the other. Two

outlier measurements from BBNP were excluded from the means; however, it is important to note that while they are uncommon, large structures were observed in BBNP despite the average scale of structures being smaller. More measurements were recorded at BBNP than at 71 Gulch, which could contribute to an increased likelihood of finding uniquely large structures. The outliers include a bulbous crest structure with a wavelength of 210 cm, 97 cm being the next largest crest wavelength, and a circular structure with a wavelength of 110 cm, 77 cm being the next largest trough wavelength.

Interpretations

Billowed structures formed from the intrusion of OIB-like basaltic magma and water-bearing sediments do not differ significantly in structure geometry or scale. Abundances of identified structure types and the mean wavelength and amplitude measurements of billowed structures are similar between both localities despite their significantly different formation depths below the pre-eruptive surface and magma viscosities. The slight variations in shape and size may be dependent on the heterogeneity of the host-sediment.

CHAPTER 5: CONCLUSIONS

This study of preserved billowed structures along the margins of basaltic intrusions from two localities provides insight on the conditions that enable non-explosive interactions of magma and wet sediment across a range of intrusion depths. The two localities, Big Bend National Park, Texas and 71 Gulch, Idaho, were selected because of their similarities in the magma and host sediment compositions, as well as the difference in the depth at which billowed structures formed. Differences in the population and geometries of billowed structure types were analyzed through field measurements, photogrammetric modelling, and DEM analysis. Estimates in magma density, magma viscosity, and host sediment density, as well as indicators of flowing magma during billow formation were analyzed through geochemical and petrographic analysis.

Through this study, it can be concluded that billowed structures form as magma intrudes through unconsolidated water-bearing sediment and velocity shear occurs between the soft, malleable mediums of differing densities, generating billowed structures due to Kelvin-Helmholtz instability. The rapid cooling of flowing magma then preserves the structures of varying geometries and scale along the glassy margins of the intrusion. A vapor film may form during this process to insulate the intruding magma and prevent explosive interaction.

The presence of an abundance of water at the time of magma intrusion is evident in the preservation of glassy intrusive margins, which bears resemblance of pillow lava quench margins, showing palagonite and sideromelane transitioning to tachylyte moving inwards from the exterior margin of the intrusion. Additionally, evidence of nearby desiccation cracks in sediment at BBNP and pillow lavas at 71 Gulch, and the presence of peperites and local

phreatomagmatic deposits at both sites, suggest that ample water was available at both localities.

In thin section and field observations, preferential alignment of elongate vesicles and plagioclase laths suggest that billowed structures were able to form while magma was first flowing in contact with sediment before it quickly cooled. Cracking due to the expansion of glassy margins were not evident in thin section, leading to the conclusion that magma did not first intrude, then expand outwards to form the billowed structures. Since magma is flowing at the time of billowed structure formation, orientations of billowed structures and elongate vesicles observed in outcrop may be indicative of complex local lateral and vertical flow direction.

Magma, being the denser and faster moving of the two interacting mediums, may generate billowed structures which resemble textures like ropy pahoehoe, where crests and troughs are oriented perpendicular to flow direction. Linear crest orientations at BBNP were likely found to be more orderly, oriented similarly along a single 4 km long dike, because confining pressure increases with depth, whereas, at 71 Gulch, orientations were less orderly. The disorder at 71 Gulch is likely due to the magma pressure exceeding the confining pressure, allowing for the magma to begin propagating more freely and less sheet-like. Elongate vesicles also show preferential orientation, certainly providing evidence of flow during magma emplacement. The orientations of these vesicles are parallel to sub-parallel to the orientation of billowed structure crest and trough orientation, suggesting that flow direction as magma is cooling is parallel to the billowed structure orientation. Likely, these two factors are indicators of complex localized lateral and vertical flow direction as the intrusion propagated in the subsurface. To determine if these two factors, linear crest

orientation and elongate vesicles, could indicate flow direction, more detailed research out of the scope of this project is necessary.

All classifications of identified billowed structures were found to form at depths from 400-500 meters below the pre-eruptive surface at BBNP and ≤24 meters below the pre-eruptive surface at 71 Gulch, in magmas of similar basaltic composition, and mingling with sediment of similar composition. Viscosities of the two magmas are also relatively similar at the presumed 1100°C regime with mean viscosities varying from 31.6 Pa*s at BBNP to 7.5 Pa*s at 71 Gulch at varying water contents.

Magma intruding through the subsurface is often prone to interaction with water in some fashion. These unusual structures shed light on how magmas migrate towards the surface through water-bearing sediment in a non-explosive nature. It is important to maintain dialogue and research regarding this interaction as explosive magma-water interaction can occur in populated areas where lives and property are at risk. The more we understand about the conditions of explosivity vs. non-explosivity and the migration of magma through the subsurface, the more prepared we can be in monitoring and mitigation efforts in volcanic environments.

APPENDIX

Sample Information

Sample ID	Collected By	Latitude	Longitude	Analysis	Classification
AJG-001-1	Aaron G.	29.32445	-103.45195	Thin section	Intrusion margin
AJG-002-1	Aaron G.	29.32562	-103.45204	Thin section	Intrusion interior
AJG-007-1	Aaron G.	29.29531	-103.50894	Thin section	Intrusion interior
AJG-012-1A	Aaron G.	29.34817	-103.45290	Thin section	Intrusion margin
AJG-012-1B	Aaron G.	29.34817	-103.45290	Thin section	Intrusion margin
AJG-017-1	Aaron G.	29.35099	-103.45291	Thin section	Intrusion margin
09-008	Richard H.	29.29762	-103.50417	XRF, ICPMS	Intrusion interior
09-025	Richard H.	29.29958	-103.50216	XRF, ICPMS	Intrusion interior
2016DD	Richard H.	29.32563	-103.45208	XRF, ICPMS	Intrusion interior
KB011b	Kadie B.	42.77475	-115.68562	Thin section, XRF, ICPMS	Intrusion margin
KB024	Kadie B.	42.77538	-115.68722	Thin section, XRF, ICPMS, SEM, EDS	Intrusive margin
KB030	Kadie B.	42.77538	-115.67602	Thin section, XRF, ICPMS, SEM, EDS	Intrusion margin
KB036	Kadie B.	42.77587	-115.68806	Thin section	Intrusive margin
KB055	Kadie B.	42.77892	-115.69356	Thin section, XRF, ICPMS	Intrusive margin
KB061a	Kadie B.	42.76961	-115.67349	Thin section	Intrusion margin
KB078	Kadie B.	42.77635	-115.68900	Thin section, XRF, ICPMS	Intrusion margin

Thin Section Descriptions

Thin Section ID	GPS Waypoint ID	Description
AJG001-1	AJG-001	The outer-most edge of the glassy intrusion margin consists of about 10% subhedral plagioclase microlite laths and 10% subhedral oxide microlites. Laths occur in a groundmass of sideromelane with 10% vesicularity. Vesicles are elongate and oval in shape and secondary minerals of zeolite and calcite fill most void spaces with small veins of calcite up to 0.5 mm in wide also present. Elongate vesicles and plagioclase laths show preferred orientation parallel to dike margin. The sedimentary component adhered to the exterior of the intrusion consists of 20-30% fine-grained angular clasts of plagioclase, oxides, and calcite in a very fine-grained matrix and calcite cement. Calcite veins up to 1 mm wide are common.
AJG002-1	AJG002	50-60% subhedral plagioclase microlite laths, 5% subhedral oxide microlites, 2-5% anhedral clinopyroxene microlites, and scarce euhedral 1 mm long phenocrysts of olivine are observed in a hyalopilitic groundmass of sideromelane. The smaller plagioclase laths are oriented parallel to dike orientation. Some larger phenocrysts and glomerocrysts of plagioclase, 1-5 mm long, and equant and elongate subhedral oxides, up to 1 mm wide, are present. Vesicles were not observed in this sample.
AJG007-1	AJG007	55% anhedral to subhedral microlite laths of plagioclase, 10% anhedral microlites of oxide, and 5-10% anhedral microlites clinopyroxene in a hyalopilitic groundmass of sideromelane. Some larger phenocryst laths of plagioclase, up to 1.5 mm long, are present. A poikilitic texture is observed with plagioclase surrounded by or included in larger clinopyroxene. There is no preferred crystal orientation in this sample.

AJG012A-1	AJG-012	10% subhedral microlite laths of plagioclase and <5% anhedral oxides set in an intersertal groundmass of sideromelane with 20% vesicularity. Some larger phenocrysts and few glomerocrysts of plagioclase similar in size, 0.5-0.6 mm in diameter, are present. Plagioclase laths have a slight preferred orientation parallel to orientation of the dike margin in samples. Small vesicles, <0.05 to 0.4 mm in diameter, are rimmed and sometimes filled by fibrous zeolite. Calcite amygdules 0.4 to 1.5 mm in diameter are also present. One skeletal oxide present (~0.5 mm). The outer, most exterior portion of the margin is composed of a lighter brown colored palagonite which grades to opaque tachylyte glass, then grades to a more plagioclase abundant groundmass moving inwards.
AJG012A-2	AJG-012	20% subhedral microlite laths of plagioclase and 20% anhedral oxides set in an intersertal groundmass of sideromelane with 15% vesicularity. Some larger phenocrysts and few glomerocrysts of plagioclase similar in size, 0.5-1.0 mm in diameter, are present. Plagioclase laths have a slight preferred orientation parallel to orientation of the dike margin in samples. Small vesicles, 0.1 to 0.1 mm in diameter, are rimmed and sometimes filled by fibrous zeolite. Calcite amygdules sometimes fills vesicles.
AJG012A-3	AJG-012	15% subhedral microlite laths of plagioclase and 10% anhedral oxides set in an intersertal groundmass of sideromelane with 25% vesicularity. Some larger phenocrysts and few glomerocrysts of plagioclase similar in size, 0.4-1.0 mm in diameter, are present. No apparent indication of flow direction from crystal orientation. Small vesicles, 0.05 to 0.6 mm in diameter, are rimmed and sometimes filled by fibrous zeolite. Calcite amygdules sometimes fills vesicles.

AJG012B-1	AJG-012	5-10% subhedral microlite laths of plagioclase and <5% anhedral oxides set in an intersertal groundmass of sideromelane with 15% vesicularity. Some larger phenocrysts and few glomerocrysts of plagioclase similar in size, 0.3-0.8 mm in diameter, are present. Plagioclase laths and vesicles have a slight preferred orientation parallel to orientation of the dike margin in samples. Small vesicles, <0.05 to 0.4 mm in diameter, are rimmed and sometimes filled by fibrous zeolite. Calcite amygdules <0.05 to 2.0 mm in diameter are also present. A circular sedimentary lithic, approximately 2 mm in diameter, is present approximately 2 mm from the exterior margin consisting of fine-grained angular fragments of plagioclase, angular quartz, and subrounded calcite in a matrix of clay and some sideromelane with smaller plagioclase laths oriented around it.
AJG012B-2	AJG-012	5% subhedral microlite laths of plagioclase and <5% anhedral oxides set in an intersertal groundmass of denser sideromelane with 15% vesicularity. Some larger phenocrysts and few glomerocrysts of plagioclase similar in size, 0.4-2.0 mm in diameter, are present. No apparent indication of flow direction from crystal orientation or vesicles. Small vesicles, <0.05 to 0.3 mm in diameter, are rimmed and sometimes filled by fibrous zeolite. Calcite amygdules <0.05 to 2.0 mm in diameter are also present.
AJG012B-3	AJG-012	~5% subhedral microlite laths of plagioclase and <5% anhedral oxides set in an intersertal groundmass of sideromelane with 15% vesicularity. Some larger phenocrysts and few glomerocrysts of plagioclase similar in size, 0.4-0.6 mm in diameter, are present. No apparent indication of flow direction from crystal orientation or vesicles. Small vesicles, <0.05 to 0.5 mm in diameter, are rimmed and sometimes filled by fibrous zeolite. Calcite amygdules <0.05 to 2.0 mm in diameter are also present.

AJG017-1	AJG-017	5% subhedral microlite laths of plagioclase and <5% anhedral oxides set in a slightly denser intersertal groundmass of denser sideromelane with 15% vesicularity. Some larger phenocrysts and few glomerocrysts of plagioclase similar in size, 0.4-1.5 mm in diameter, are present. No apparent indication of flow direction from crystal orientation or vesicles. Small vesicles, <0.05 to 0.5 mm in diameter, are circular and often rimmed and sometimes filled by fibrous zeolite. Calcite amygdules <0.05 to 3.0 mm in diameter are also present.
AJG017-2	AJG-017	5% subhedral microlite laths of plagioclase and <5% anhedral oxides set in a denser intersertal groundmass of denser sideromelane with 5% vesicularity. No apparent indication of flow direction from crystal orientation or vesicles. Small vesicles, <0.05 to 0.5 mm in diameter, are circular and often rimmed and sometimes filled by fibrous zeolite. Calcite amygdules <0.05 to 3.0 mm in diameter are also present.
KB011b	71G030	Consists of 60% tachylyte, 20% subhedral plagioclase laths, 10% subhedral clinopyroxene, and <5% anhedral orthopyroxene, with 30% vesicular and 40% groundmass. Vesicles (0.2-0.8 mm) are subrounded and are often rimmed or filled with secondary minerals. No preferential alignment of phenocrysts or vesicles is apparent. Some glomerocrysts (0.7 – 3.5 mm wide) of clinopyroxene, plagioclase, and orthopyroxene are present.
KB024	71G056	Consists of 45% tachylyte, 20% subhedral to euhedral plagioclase microlite laths, 15% subhedral clinopyroxene, and <5% orthopyroxene with 15% vesicular and 50% groundmass.

KB030bb	71G076	Consists of 85% tachylyte, 5% sideromelane, 20% euhedral plagioclase microlite laths, 5% subhedral clinopyroxene, and <5% subhedral orthopyroxene with 35% vesicularity and 40% groundmass. Vesicles (<0.1-0.5 mm) are subrounded and are often rimmed or filled with secondary minerals. There is an apparent contact between sediment and fluid-looking sideromelane and between the sideromelane and the tachylyte. Plagioclase laths and some vesicles are preferentially oriented parallel to the dike margin. Some glomerocryst (0.9- 1.5 mm) of clinopyroxene, plagioclase, and orthopyroxene are present.
KB030bc	71G076	Consists of 85% tachylyte, 5% sideromelane, 20% euhedral plagioclase microlite laths, 5% subhedral clinopyroxene with 35% vesicularity and 40% groundmass. Vesicles (<0.1-0.8mm) are subrounded and are often rimmed or filled with secondary minerals. There is an apparent contact between sediment and fluid-looking sideromelane and between the sideromelane and the tachylyte. Plagioclase laths and some vesicles are preferentially oriented parallel to the dike margin. Some glomerocryst (0.9- 2.0 mm) of clinopyroxene, plagioclase, and orthopyroxene are present.
KB036	71G003	Consists of 55% tachylyte, 25% subhedral microlite laths of plagioclase, 5% subhedral clinopyroxene, and <5% subhedral orthopyroxene with 15% vesicular and 54% groundmass. Sediment is present and consists of angular glass shards, microcrystalline sedimentary lithics, subrounded quartz and plagioclase. Vesicles (0.1-0.6 mm wide) are subrounded and are often rimmed or filled with secondary minerals. No preferential alignment of phenocrysts or vesicles is apparent. Some glomerocrysts (0.4-1.0 mm wide) of clinopyroxene and plagioclase are present.
KB055	71G151	Consists of 60% tachylyte, 25% subhedral plagioclase microlite laths, and 5% subhedral clinopyroxene. Vesicles (0.2-1.2 mm wide) are irregular and are rimmed or filled with secondary minerals. No preferential alignment of phenocrysts or vesicles is apparent.

KB061a	71G040	Consists of 20% tachylyte, 30% subhedral and euhedral plagioclase microlite laths, 15% subhedral clinopyroxene, and <5% orthopyroxene. Vesicles (0.2-1.0 mm wide) are subrounded and are rimmed with secondary minerals. No preferential alignment of phenocrysts or vesicles is apparent. Glomerocrysts (0.7-1.5 mm wide) of clinopyroxene and plagioclase are present.
KB078	71G001	Consists of 80% tachylyte, 30% subhedral and euhedral plagioclase microlite laths, 20% subhedral clinopyroxene, and <5% orthopyroxene with 15% vesicularity and 35% groundmass. Vesicles (0.1-0.9 mm wide) are subrounded and are sometimes lightly rimmed with secondary minerals. No preferential alignment of phenocrysts or vesicles is apparent.

BBNP Manual vs. Model Trough Wavelength and Amplitude Comparison

Site	Profile	Manual Trough Measurement (cm)		Model Trough Measurement (cm)		Difference of Manual and Model Measurements (cm)	
		Wavelength	Amplitude	Wavelength	Amplitude	Wavelength	Amplitude
AJG-001	A	13	15	14	8	1	7
	B	23	15	22	6	1	9
	C	26	13	25	9	1	4
AJG-003	A	9.5	6	10	2	0	4
	B	18	6	18	6	0	1
	C	11	7	12	4	1	3
AJG-004	A	24	24	29	24	5	0
	B	43	23	46	17	3	6
AJG-005	A	26	30	28	30	2	0
	B	20	16	21	15	1	1
	C	33	13	32	14	1	1
AJG-006	A	46	21	45	21	1	0
	B	41	21	42	25	1	4
AJG-007	A	15	4	15	4	0	0
	B	10	2	11	2	1	0
AJG-008	A	22	4	21	2	1	2
	B	20	5	20	2	0	3
AJG-011	A	15	5	16	3	1	2
	B	13	4	10	2	3	2
	C	14	3	13	2	1	1
AJG-012	A	13	7	13	6	0	1
	B	14	5	14	5	0	0
	C	11	6	11	6	0	0
	D	10	5	11	1	1	4
AJG-013	A	10	3	11	3	1	0
	B	8	2	8	1	0	1
	C	6	3	6	2	0	1
AJG-017 West	A	15	7	16	4	1	3
	B	15	6	15	4	0	2
AJG-017 East	A	10	4	10	4	0	0
	B	18	8	19	8	1	0

71 Gulch Manual vs. Model Trough Wavelength and Amplitude Comparison

Site	Profile	Manual Measurement (cm)		Model Measurement (cm)		Difference of Manual and Model Measurements (cm)	
		Wavelength	Amplitude	Wavelength	Amplitude	Wavelength	Amplitude
71G002	A	17	8	16	8	1	0
	B	15	8	16	8	1	0
	C	8	5	10	5	2	0
	D	18	7	21	7	3	0
	E	74	33	72	39	2	6
71G018	A	42	18	43	20	1	2
	B1	21	9	21	7	0	2
	B2	36	11	37	11	1	0
	B3	19	9	21	8	2	1
	C	32	6	32	8	0	2
	D	19	6	20	3	1	3
	E	12	6	13	7	1	1
71G019-1	A	24	10	25	10	1	0
	B	20	7	20	6	0	1
	C	40	13	41	12	1	1
71G019-2	A	19	10	19	9	0	1
	B	17	4	16	4	1	0
	C	14	3	13	5	1	2
	D	42	10	44	8	2	2
71G032	A	33	9	32	9	1	0
	B	37	13	37	15	0	2
	C	26	9	26	8	0	1
AJG-7101	A	55	20	63	25	8	5
	B	53	7	54	10	1	3
	C	25	11	26	16	1	5
AJG-7102	A	13	5	14	6	1	1
	B	39	6	40	5	1	1
	C	25	9	25	10	0	1
AJG-7103	A	13	6	15	7	2	1
	B	19	5	20	5	1	0
	C	14	5	13	5	1	0
	D	14	8	14	10	0	2
	E	39	6	41	9	2	3
AJG-7104	A	38	11	38	10	0	1
	B	60	16	62	19	2	3
	C	33	19	33	18	0	1
	D	15	8	15	7	0	1
AJG-7105	A	29	10	29	11	0	1
	B	30	6	31	8	1	2
	C	57	11	56	10	1	2
	D	46	21	47	22	1	1

Additional Trough Measurements - BBNP

Site	Profile	Associated Structure	Model Trough Measurement (cm)	
			Wavelength	Amplitude
AJG-001	A*	L-L	14	8
	B*	L-L	22	6
	C*	S-S	25	9
	D	L-B	25	8
	E	L-L	17	5
	F	S-B	13	7
	G	L-S	17	6
	H	L-B	28	12
	I	Teardrop	7	3
	J	L-L	14	4
	K	B-B	17	4
	L	S-B	31	9
	M	L-B	14	6
	N	L-B	10	6
	O	L-B	29	5
	P	Teardrop	23	8
	Q	Circular	13	3
AJG-003	A*	L-O	10	2
	C*	L-B	12	4
	D	L-L	9	3
	E	S-B	9	3
	F	S-B	5	3
	G	L-L	9	3
AJG-004	A*	B-B	29	24
	B*	L-B	46	17
	C	Circular	22	4
	D	L-B	17	8
	E	B-B	17	3
AJG-005	A*	Teardrop	28	30
	B*	Teardrop	21	15
	C*	Teardrop	32	14
	D	B-B	28	13
	E	Teardrop	27	9
	F	Teardrop	77	34
	G	Teardrop	38	28
AJG-006	A*	Teardrop	45	21
	B*	B-B	42	25
	C	Circular	110	27

	D	B-B	37	10
	E	B-B	19	5
	F	B-B	25	3
AJG-007	A*	Teardrop	15	4
	B*	S-B	11	2
	C	B-B	26	3
	D	B-B	28	3
	E	B-B	18	3
	F	B-B	16	3
	G	B-B	48	5
	H	S-B	20	5
	I	B-B	22	3
	J	B-B	33	5
	K	B-B	19	3
	L	B-B	16	2
	M	B-B	22	3
	N	B-B	21	3
	O	B-B	16	2
	P	B-B	19	3
AJG-008	A*	B-B	21	2
	B*	B-B	20	2
	C	B-B	36	10
AJG-011	A*	L-B	16	3
	B*	Teardrop	10	2
	C*	B-B	13	2
	D	B-B	9	2
	E	S-B	13	2
	F	B-B	20	5
	G	L-S	10	3
	H	L-B	13	3
	I	B-B	14	7
	J	B-B	15	4
	K	B-B	11	2
	L	L-B	21	3
	M	B-B	15	2
	N	B-B	16	2
	O	L-B	6	2
AJG-012	A*	L-O	13	6
	B*	L-O	14	5
	C*	Teardrop	11	6
	E	Circular	27	7
	F	Circular	9	2
	G	Circular	10	2

91

	H	Circular	8	2
	I	Circular	18	2
	J	Teardrop	10	3
	K	L-O	17	5
	L	L-L	16	4
	M	Teardrop	14	6
	N	L-O	13	2
	O	L-O	16	5
	P	L-O	12	3
AJG-013	A*	L-L	11	3
	B*	B-B	8	1
	C*	L-B	6	2
	D	Circular	14	2
	E	L-B	7	1
	F	L-O	18	4
	G	B-B	16	6
	H	L-B	16	4
	I	L-B	15	4
	J	L-O	11	3
	K	L-B	23	5
	A*	B-B	16	4
	B*	B-B	15	4
	C	B-B	17	4
	D	B-B	38	8
	E	L-B	12	5
	F	B-B	19	6
	G	B-B	17	8
AJG-017 West	H	B-B	29	12
	I	B-B	20	4
	J	L-B	11	2
	K	Circular	14	3
	L	B-B	6	1
	M	L-L	13	3
	N	B-B	12	5
	O	L-B	8	2
	P	B-B	13	2
	Q	B-B	20	6
	A*	L-B	10	4
	B*	S-B	19	8
AJG-017 East	C	S-B	36	18
	D	L-L	23	5
	E	B-B	20	6
	F	L-B	57	7

G	L-B	16	2
H	L-B	21	4
I	L-B	57	10
J	B-B	25	2
K	L-B	12	2
L	B-B	22	5
M	L-B	30	8
N	L-L	8	2

Note: Troughs that are not classified as circular or teardrop are a variation of transitional trough.
Asterixis indicate model measurements that coincide with an existing manual measurement.

Additional Crest Measurements - BBNP

Site	Profile	Associated Structure	Model Crest Measurement (cm)	
			Wavelength	Amplitude
	A1	Linear	18	7
	A2	Linear	17	6
	B1	Linear	24	7
	C1	Sinuous	21	9
	C2	Sinuous	24	10
	C3	Linear	12	6
	D1	Bulbous	35	6
	F1	Bulbous	14	5
	F2	Sinuous	27	6
	G1	Sinuous	22	5
	H1	Bulbous	29	7
AJG-001	H2	Linear	31	13
	I1	Bulbous	15	4
	J1	Linear	9	4
	J2	Linear	8	2
	K1	Bulbous	17	6
	M1	Linear	19	8
	M2	Bulbous	29	8
	N1	Linear	15	5
	N2	Bulbous	23	6
	O1	Linear	20	5
	Q1	Bulbous	20	3
	A1	Linear	24	6
	B1	Sinuous	32	6
	C1	Linear	6	2
	D1	Bulbous	9	2
	E1	Sinuous	12	4
	E2	Bulbous	14	3
AJG-003	F1	Sinuous	7	2
	F2	Bulbous	13	5
	G1	Linear	7	3
	G2	Linear	10	3
	H1	Bulbous	16	7
	I1	Sinuous	11	7
	J1	Sinuous	10	2
	A1	Bulbous	54	21
AJG-004	B1	Linear	69	18
	B2	Bulbous	67	12

	D1	Linear	97	8
	D2	Bulbous	110	12
	E1	Bulbous	29	6
	E2	Bulbous	15	2
	A1	Sinuous	35	16
	A2	Bulbous	62	23
	A3	Bulbous	39	13
	B1	Bulbous	44	14
AJG-005	C1	Bulbous	49	11
	D1	Bulbous	35	14
	E1	Bulbous	51	14
	F1	Bulbous	75	16
	F2	Bulbous	66	16
	G1	Bulbous	83	19
	A1	Bulbous	44	19
	B1	Sinuous	64	20
AJG-006	E1	Bulbous	35	8
	F1	Bulbous	25	4
	G1	Bulbous	52	12
	A1	Bulbous	25	3
	B1	Bulbous	21	3
	C1	Bulbous	26	4
	C2	Linear	23	3
	D1	Bulbous	41	5
	D2	Bulbous	35	4
	F1	Bulbous	14	2
	G1	Bulbous	34	5
	H1	Sinuous	17	3
	I1	Bulbous	22	3
	I2	Bulbous	23	2
AJG-007	J1	Bulbous	30	4
	K1	Bulbous	28	4
	K2	Bulbous	28	3
	L1	Bulbous	14	2
	M1	Bulbous	27	3
	M2	Bulbous	22	2
	N1	Bulbous	20	2
	N2	Bulbous	25	3
	O1	Bulbous	27	3
	O2	Bulbous	24	4
	P1	Bulbous	25	4
	P2	Bulbous	22	2
AJG-008	A1	Bulbous	28	2

A2	Bulbous	57	8
B1	Bulbous	15	1
B2	Bulbous	19	4
C1	Bulbous	231	30
C2	Bulbous	30	7
D1	Bulbous	24	8
E1	Bulbous	76	16
F1	Sinuous	67	13
	A1	Bulbous	18	4
	A2	Linear	7	2
	B1	Linear	8	2
	B2	Bulbous	17	2
	C1	Bulbous	19	2
	D1	Bulbous	13	3
	D2	Bulbous	14	2
	E1	Bulbous	13	2
	E2	Sinuous	13	2
	F1	Bulbous	12	3
	F2	Bulbous	30	3
	G1	Sinuous	7	2
	G2	Linear	14	3
	H1	Bulbous	12	2
AJG-011	I1	Bulbous	16	4
	I2	Bulbous	21	3
	J1	Bulbous	20	4
	J2	Bulbous	29	3
	K1	Bulbous	16	2
	L1	Bulbous	12	2
	L2	Linear	19	2
	M1	Bulbous	23	3
	M2	Bulbous	16	3
	N1	Bulbous	18	3
	O1	Linear	4	1
	O2	Bulbous	25	3
	P1	Bulbous	15	3
	Q1	Linear	15	2
	R1	Bulbous	11	3
	A1	Linear	17	5
	B1	Linear	21	5
AJG-012	G1	Bulbous	10	2
	J1	Bulbous	14	3
	K1	Linear	17	3
	L1	Linear	18	4

L2	Linear	19	5
M1	Linear	5	1
O1	Linear	16	4
P1	Linear	9	1
Q1	Linear	15	4
R1	Linear	8	1
S1	Linear	11	3
A1	Linear	11	3
A2	Linear	12	2
B1	Bulbous	14	2
B2	Bulbous	19	3
C1	Linear	10	2
C2	Bulbous	8	3
D1	Bulbous	12	3
E1	Linear	9	2
F1	Linear	35	5
F2	Bulbous	15	3
AJG-013 H1	Linear	13	3
H2	Bulbous	8	2
I1	Bulbous	34	6
J1	Linear	14	3
L1	Linear	6	1
M1	Linear	8	2
N1	Linear	8	2
O1	Linear	10	2
P1	Linear	12	3
Q1	Linear	7	1
R1	Bulbous	12	2
B1	Bulbous	66	9
B2	Bulbous	10	1
C1	Bulbous	30	7
D1	Bulbous	52	10
D2	Bulbous	16	2
E1	Linear	10	5
E2	Bulbous	26	7
AJG-017 F1	Bulbous	44	9
West F2	Bulbous	31	6
G1	Bulbous	36	5
G2	Linear	38	10
H1	Bulbous	24	7
I1	Bulbous	33	10
I2	Linear	23	4
J1	Linear	7	1

	K1	Bulbous	29	3
	L1	Bulbous	10	2
	L2	Bulbous	20	2
	M1	Linear	23	3
	M2	Linear	9	2
	N1	Bulbous	13	4
	O1	Linear	8	3
	O2	Bulbous	16	2
	P1	Bulbous	19	3
	P2	Bulbous	13	2
	Q1	Bulbous	16	4
	R1	Bulbous	24	6
	S1	Bulbous	14	3
	T1	Bulbous	32	7
	U1	Bulbous	23	6
AJG-017 East	A1	Linear	11	3
	A2	Bulbous	6	1
	B1	Sinuous	19	11
	B2	Bulbous	12	4
	C1	Bulbous	39	8
	D1	Linear	24	10
	D2	Linear	43	7
	E1	Bulbous	66	12
	F1	Linear	26	7
	G1	Linear	9	2
	G2	Linear	14	2
	H1	Linear	31	6
	H2	Bulbous	30	3
	I1	Bulbous	62	11
	J1	Bulbous	30	6
	J2	Bulbous	32	6
	K1	Linear	16	2
	K2	Linear	11	2
	L1	Bulbous	32	7
	M1	Bulbous	56	12
	M2	Linear	20	6
	N1	Linear	11	3
	N2	Linear	7	1

Additional Trough Measurements – 71 Gulch

Site	Profile	Associated Structure	Model Trough Measurement (cm)	
			Wavelength	Amplitude
71G002	A*	L-S	16	8
	B*	B-S	16	8
	C*	B-S	10	5
	D*	Teardrop	21	7
	E*	Circular	72	39
	F	L-L	8	5
	G	L-L	8	6
	H	L-B	19	11
	I	B-B	20	5
	J	L-B	11	3
	K	B-B	24	12
	L	B-B	17	12
	M	B-B	29	9
	N	L-B	16	6
	O	L-B	19	10
71G018	A*	Circular	43	20
	B1*	Teardrop	21	7
	B2*	Teardrop	37	11
	B3*	Teardrop	21	8
	C*	Teardrop	32	8
	D*	Teardrop	20	3
	E*	Circular	13	7
	F	B-B	26	9
	G	B-B	23	6
	H	B-B	22	6
	I	B-B	25	6
71G019-1	A*	B-B	25	10
	B*	B-B	20	6
	C*	B-B	41	12
	D	B-B	20	6
	E	B-B	22	5
	F	B-B	21	5
	G	B-B	26	5
	H	B-B	20	6
71G019-2	A*	B-B	19	9
	B*	Circular	16	4
	C*	L-B	13	5
	D*	B-B	44	8

E	L-L	8	1
F	Circular	15	3
G	Circular	10	3
H	B-B	9	2
I	B-B	11	3
J	Circular	15	3
K	Circular	13	4
L	B-B	22	5
71G032			
A*	L-B	32	9
B*	S-B	37	15
C*	L-B	26	8
D	B-B	16	3
AJG-7101			
A*	L-O	63	25
B*	L-O	54	10
C*	L-B	26	16
D	B-B	22	5
E	B-B	10	2
F	B-B	47	8
G	B-B	6	2
H	B-B	30	3
AJG-7102			
A*	S-B	14	6
B*	Circular	40	5
C*	B-B	25	10
D	Circular	14	4
E	B-B	17	4
F	Circular	11	2
G	B-B	18	4
H	B-B	20	13
AJG-7103			
A*	B-B	15	7
B*	L-B	20	5
C*	B-B	13	5
D*	L-L	14	10
E*	L-B	41	9
F	L-B	20	5
G	L-B	19	7
H	B-B	27	4
I	B-B	12	3
J	B-B	20	10
AJG-7104			
A*	Circular	38	10
B*	B-O	62	19
C*	B-B	33	18
D*	L-B	15	7
E	Circular	21	7

	F	B-B	38	11
	A*	L-B	29	11
	B*	Circular	31	8
AJG-7105	C*	B-B	56	10
	D*	L-B	47	22
	E	B-O	42	17

Note: Troughs that are not classified as circular or teardrop are a variation of transitional trough. Asterixis indicate model measurements that coincide with an existing manual measurement.

Additional Crest Measurements – 71 Gulch

Site	Profile	Associated Structure	Model Trough Measurement (cm)	
			Wavelength	Amplitude
71G002	A1	Sinuous	23	12
	A2	Linear	20	12
	B1	Bulbous	17	16
	C1	Sinuous	8	3
	C2	Bulbous	14	4
	D1	Bulbous	26	8
	D2	Sinuous	19	7
	F1	Linear	7	7
	F2	Linear	12	9
	G1	Linear	11	11
	H1	Linear	14	12
	H2	Bulbous	19	10
	I1	Bulbous	27	7
	I2	Bulbous	25	8
	J1	Bulbous	11	3
	K1	Bulbous	24	11
	N1	Linear	20	7
	N2	Bulbous	19	3
	O1	Bulbous	19	12
	O2	Linear	11	5
	P1	Linear	11	4
	Q1	Bulbous	14	8
71G018	A1	Bulbous	49	16
	B1	Bulbous	21	4
	D1	Bulbous	39	9
	E1	Bulbous	16	5
	G1	Bulbous	35	4
71G019-1	A1	Bulbous	24	7
	B1	Bulbous	31	8
	B2	Bulbous	23	7
	C1	Bulbous	19	4
	D1	Bulbous	20	4
	D2	Bulbous	21	7
	E1	Bulbous	17	7
	F1	Bulbous	19	4
	F2	Bulbous	20	4
	G1	Bulbous	38	7
	G2	Bulbous	20	2

I1	Bulbous	19	3
J1	Bulbous	27	5
K1	Linear	18	4
L1	Bulbous	13	5
M1	Bulbous	32	7
71G019-2	A1	Bulbous	18	6
	B1	Bulbous	27	4
	C1	Linear	14	4
	C2	Bulbous	18	4
	D1	Bulbous	41	12
	E1	Linear	11	2
	E2	Linear	9	3
	G1	Bulbous	16	3
	H1	Bulbous	10	2
	I1	Bulbous	22	6
	I2	Bulbous	11	2
	J1	Bulbous	20	5
	K1	Bulbous	15	2
	L1	Bulbous	28	4
	M1	Sinuous	14	3
	N1	Linear	14	2
71G032	A1	Bulbous	46	14
	A2	Linear	41	6
	B1	Sinuous	37	15
	D1	Bulbous	24	4
AJG-7101	A1	Linear	46	14
	C1	Bulbous	25	8
	D1	Bulbous	21	5
	E1	Bulbous	24	5
	H1	Bulbous	20	5
AJG-7102	A1	Sinuous	18	6
	A2	Bulbous	26	4
	B1	Bulbous	27	4
	C1	Bulbous	28	6
	C2	Bulbous	20	8
	D1	Bulbous	27	5
	E1	Bulbous	14	4
	E2	Bulbous	18	4
	G1	Bulbous	13	2
	I1	Bulbous	39	14
AJG-7103	A1	Bulbous	31	9
	B1	Linear	17	3
	B2	Bulbous	22	5

C1	Bulbous	17	4
C2	Bulbous	35	5
D1	Linear	15	8
E1	Linear	41	7
E2	Bulbous	49	10
F1	Linear	29	11
G1	Linear	26	13
H1	Bulbous	18	5
H2	Bulbous	30	8
I1	Bulbous	13	3
I2	Bulbous	13	3
J1	Bulbous	30	9
K1	Bulbous	16	8
L1	Bulbous	18	5
	A1	Bulbous	53	13
	B1	Bulbous	42	16
	C1	Bulbous	37	14
AJG-7104	D1	Linear	19	5
	D2	Bulbous	26	6
	E1	Bulbous	19	5
	F1	Bulbous	37	13
	F2	Bulbous	39	15
	A1	Linear	39	12
	B1	Bulbous	48	9
	C1	Bulbous	26	7
AJG-7105	C2	Linear	38	12
	D1	Linear	44	21
	D2	Bulbous	58	14
	E1	Bulbous	55	10
	F1	Sinuous	35	9

Statistics of Trough Measurements - BBNP

	Maximum Wavelength (cm):	110	Maximum Amplitude (cm):	34
	Minimum Wavelength (cm):	5	Minimum Amplitude (cm):	1
All Trough	Mean Wavelength (cm):	20	Mean Amplitude (cm):	6
Types	Median Wavelength (cm):	17	Median Amplitude (cm):	4
	Mode Wavelength (cm):	N/A	Mode Amplitude (cm):	3
	Standard Deviation (cm):	14	Standard Deviation (cm):	6
	Maximum Wavelength (cm):	77	Maximum Amplitude (cm):	34
	Minimum Wavelength (cm):	7	Minimum Amplitude (cm):	2
Teardrop	Mean Wavelength (cm):	26	Mean Amplitude (cm):	13
Troughs	Median Wavelength (cm):	22	Median Amplitude (cm):	8
	Mode Wavelength (cm):	N/A	Mode Amplitude (cm):	N/A
	Standard Deviation (cm):	18	Standard Deviation (cm):	11
	Maximum Wavelength (cm):	110	Maximum Amplitude (cm):	27
	Minimum Wavelength (cm):	8	Minimum Amplitude (cm):	2
Circular	Mean Wavelength (cm):	25	Mean Amplitude (cm):	5
Troughs	Median Wavelength (cm):	14	Median Amplitude (cm):	2
	Mode Wavelength (cm):	N/A	Mode Amplitude (cm):	N/A
	Standard Deviation (cm):	29	Standard Deviation (cm):	7
	Maximum Wavelength (cm):	57	Maximum Amplitude (cm):	25
	Minimum Wavelength (cm):	5	Minimum Amplitude (cm):	1
Transitional	Mean Wavelength (cm):	19	Mean Amplitude (cm):	5
Troughs	Median Wavelength (cm):	16	Median Amplitude (cm):	4
	Mode Wavelength (cm):	N/A	Mode Amplitude (cm):	3
	Standard Deviation (cm):	10	Standard Deviation (cm):	4

Statistics of Crest Measurements - BBNP

All Crest Types	Maximum Wavelength (cm):	231	Maximum Amplitude (cm):	30
	Minimum Wavelength (cm):	4	Minimum Amplitude (cm):	1
	Mean Wavelength (cm):	25	Mean Amplitude (cm):	5
	Median Wavelength (cm):	19	Median Amplitude (cm):	4
	Mode Wavelength (cm):	20	Mode Amplitude (cm):	2
	Standard Deviation (cm):	23	Standard Deviation (cm):	5
Sinuous Crests	Maximum Wavelength (cm):	67	Maximum Amplitude (cm):	20
	Minimum Wavelength (cm):	7	Minimum Amplitude (cm):	2
	Mean Wavelength (cm):	24	Mean Amplitude (cm):	7
	Median Wavelength (cm):	20	Median Amplitude (cm):	6
	Mode Wavelength (cm):	N/A	Mode Amplitude (cm):	3
	Standard Deviation (cm):	18	Standard Deviation (cm):	5
Linear Crests	Maximum Wavelength (cm):	97	Maximum Amplitude (cm):	18
	Minimum Wavelength (cm):	4	Minimum Amplitude (cm):	1
	Mean Wavelength (cm):	17	Mean Amplitude (cm):	4
	Median Wavelength (cm):	14	Median Amplitude (cm):	3
	Mode Wavelength (cm):	N/A	Mode Amplitude (cm):	1
	Standard Deviation (cm):	14	Standard Deviation (cm):	3
Bulbous Crests	Maximum Wavelength (cm):	231	Maximum Amplitude (cm):	30
	Minimum Wavelength (cm):	6	Minimum Amplitude (cm):	1
	Mean Wavelength (cm):	30	Mean Amplitude (cm):	6
	Median Wavelength (cm):	24	Median Amplitude (cm):	4
	Mode Wavelength (cm):	N/A	Mode Amplitude (cm):	2
	Standard Deviation (cm):	26	Standard Deviation (cm):	5

Statistics of Trough Measurements – 71 Gulch

All Trough Types	Maximum Wavelength (cm):	63	Maximum Amplitude (cm):	25
	Minimum Wavelength (cm):	6	Minimum Amplitude (cm):	1
	Mean Wavelength (cm):	23	Mean Amplitude (cm):	8
	Median Wavelength (cm):	20	Median Amplitude (cm):	6
	Mode Wavelength (cm):	N/A	Mode Amplitude (cm):	3
	Standard Deviation (cm):	12	Standard Deviation (cm):	5
Teardrop Troughs	Maximum Wavelength (cm):	37	Maximum Amplitude (cm):	11
	Minimum Wavelength (cm):	20	Minimum Amplitude (cm):	3
	Mean Wavelength (cm):	25	Mean Amplitude (cm):	7
	Median Wavelength (cm):	21	Median Amplitude (cm):	8
	Mode Wavelength (cm):	N/A	Mode Amplitude (cm):	N/A
	Standard Deviation (cm):	7	Standard Deviation (cm):	2
Circular Troughs	Maximum Wavelength (cm):	43	Maximum Amplitude (cm):	20
	Minimum Wavelength (cm):	10	Minimum Amplitude (cm):	2
	Mean Wavelength (cm):	21	Mean Amplitude (cm):	6
	Median Wavelength (cm):	15	Median Amplitude (cm):	4
	Mode Wavelength (cm):	N/A	Mode Amplitude (cm):	N/A
	Standard Deviation (cm):	12	Standard Deviation (cm):	5
Transitional Troughs	Maximum Wavelength (cm):	63	Maximum Amplitude (cm):	25
	Minimum Wavelength (cm):	6	Minimum Amplitude (cm):	1
	Mean Wavelength (cm):	24	Mean Amplitude (cm):	8
	Median Wavelength (cm):	20	Median Amplitude (cm):	6
	Mode Wavelength (cm):	N/A	Mode Amplitude (cm):	3
	Standard Deviation (cm):	13	Standard Deviation (cm):	5

Statistics of Crest Measurements – 71 Gulch

All Crest Types	Maximum Wavelength (cm):	58	Maximum Amplitude (cm):	21
	Minimum Wavelength (cm):	7	Minimum Amplitude (cm):	2
	Mean Wavelength (cm):	25	Mean Amplitude (cm):	7
	Median Wavelength (cm):	21	Median Amplitude (cm):	6
	Mode Wavelength (cm):	N/A	Mode Amplitude (cm):	4
	Standard Deviation (cm):	11	Standard Deviation (cm):	4
Sinuous Crests	Maximum Wavelength (cm):	37	Maximum Amplitude (cm):	15
	Minimum Wavelength (cm):	8	Minimum Amplitude (cm):	3
	Mean Wavelength (cm):	22	Mean Amplitude (cm):	8
	Median Wavelength (cm):	19	Median Amplitude (cm):	7
	Mode Wavelength (cm):	N/A	Mode Amplitude (cm):	N/A
	Standard Deviation (cm):	10	Standard Deviation (cm):	4
Linear Crests	Maximum Wavelength (cm):	46	Maximum Amplitude (cm):	21
	Minimum Wavelength (cm):	7	Minimum Amplitude (cm):	2
	Mean Wavelength (cm):	22	Mean Amplitude (cm):	8
	Median Wavelength (cm):	18	Median Amplitude (cm):	7
	Mode Wavelength (cm):	N/A	Mode Amplitude (cm):	N/A
	Standard Deviation (cm):	12	Standard Deviation (cm):	5
Bulbous Crests	Maximum Wavelength (cm):	58	Maximum Amplitude (cm):	16
	Minimum Wavelength (cm):	10	Minimum Amplitude (cm):	2
	Mean Wavelength (cm):	26	Mean Amplitude (cm):	7
	Median Wavelength (cm):	22	Median Amplitude (cm):	5
	Mode Wavelength (cm):	N/A	Mode Amplitude (cm):	4

Complete XRF Results – Unnormalized Major and Trace Element Geochemical Data

Sample ID	BBNP			71 Gulch				
	09-008	09-025	2016DD	KB011b	KB024	KB030	KB055	KB078
Wt. %								
SiO2	47.51	47.97	48.82	42.81	44.52	44.44	44.32	45.20
TiO2	2.86	2.97	2.92	3.858	4.004	3.900	3.976	3.905
Al2O3	16.64	16.79	17.21	13.13	13.46	13.62	13.36	13.32
FeO*	10.89	11.88	10.22	14.05	15.64	14.80	14.61	14.63
MnO	0.20	0.19	0.18	0.235	0.226	0.220	0.194	0.215
MgO	4.26	4.28	3.16	5.31	5.46	4.23	5.11	5.60
CaO	6.05	6.82	7.89	12.39	9.39	9.31	9.30	10.00
Na2O	4.38	4.37	4.72	2.24	2.23	2.31	2.20	2.21
K2O	1.97	2.10	2.57	0.81	0.71	0.58	0.49	1.00
P2O5	0.68	0.70	1.01	1.635	1.080	0.937	0.932	1.176
Sum	95.42	98.07	98.69	96.46	96.72	94.35	94.49	97.26
LOI %	3.52	1.27	0.57	3.08	2.37	4.84	4.55	1.99
ppm								
Ni	12	12	7	61	60	62	56	59
Cr	0	0	0	119	110	133	107	113
Sc	16	15	17	29	31	30	30	30
V	214	216	149	321	327	326	319	323
Ba	549	734	560	568	530	550	364	781
Rb	33	34	48	18	18	18	17	23
Sr	629	807	914	304	292	302	288	306
Zr	315	323	321	291	304	294	304	307
Y	28	29	33	53	56	58	54	61
Nb	43.1	46	50.6	28.4	29.2	28.6	29.0	30.0
Ga	23	24	21	21	22	23	21	23
Cu	19	20	33	34	34	34	3	32
Zn	105	107	97	154	161	165	164	157
Pb	5	5	6	6	7	7	7	7
La	39	44	49	34	36	39	39	35
Ce	85	87	103	83	85	79	85	80
Th	2	5	7	3	4	4	3	4
Nd	40	43	52	47	48	49	47	44
U	2	1	5	2	2	2	2	3

Note: Samples processed at the WSU GeoAnalytical Laboratory, WA, USA. Total Fe expressed as FeO*.

Complete ICP-MS Results

Sample ID	BBNP			71 Gulch				
	09-008	09-025	2016DD	KB011b	KB024	KB030	KB055	KB078
ppm								
La	40.91	41.81	50.77	35.18	36.86	37.71	37.09	37.49
Ce	86.29	87.99	104.29	77.16	80.92	79.12	81.39	80.32
Pr	10.49	10.60	12.85	10.4	10.92	11.11	10.86	10.84
Nd	41.84	42.67	51.51	45.95	47.7	48.22	48.27	47.43
Sm	8.74	8.94	10.88	10.98	11.67	11.61	11.67	11.44
Eu	2.82	2.90	3.45	3.51	3.66	3.67	3.74	3.67
Gd	7.66	7.74	9.43	11.3	11.86	12.13	12.01	11.71
Tb	1.14	1.15	1.40	1.84	1.91	1.96	1.9	1.9
Dy	6.28	6.44	7.62	10.93	11.35	11.59	11.55	11.62
Ho	1.17	1.18	1.39	2.18	2.25	2.35	2.31	2.37
Er	2.93	2.95	3.45	5.72	5.93	6.19	6.05	6.35
Tm	0.40	0.40	0.47	0.8	0.82	0.87	0.85	0.88
Yb	2.37	2.37	2.73	4.79	5	5.22	5.17	5.32
Lu	0.35	0.35	0.41	0.75	0.77	0.8	0.79	0.81
Ba	547	724	563	554	513	538	353	760
Th	4.82	4.77	5.86	2.39	2.57	2.42	2.68	2.91
Nb	42.31	43.56	51.63	27.74	29.11	28.18	30.04	29.66
Y	29.05	29.21	34.50	52.92	54.42	58.19	57.47	62.08
Hf	6.86	7.05	7.67	7.13	7.41	7.15	7.54	7.48
Ta	2.84	2.97	3.44	1.84	1.93	1.88	1.91	1.87
U	1.47	1.47	1.86	1.24	0.98	1.05	0.83	1.37
Pb	4.78	4.56	5.00	5.49	5.73	5.15	5.64	6.06
Rb	31.90	32.80	47.50	15.9	15.4	15.9	16.6	21.6
Cs	4.96	3.71	0.91	0.2	0.49	0.81	1.36	0.51
Sr	657	834	933	298	281	293	296	306
Sc	16	16	16	27.2	27.2	26.9	30.4	29.8
Zr	317	326	339	293	307	296	319	314

Note: Samples processed at the WSU GeoAnalytical Laboratory, WA, USA. Rare Earth Elements are unnormalized.

AJG-001 at BBNP – DEM and billow profiles

AJG-003 at BBNP – DEM and billow profiles

A Profile
B Profile
C Profile
D Profile
E Profile
A1 Profile
B1 Profile
B2 Profile
D1 Profile
D2 Profile
E1 Profile
E2 Profile
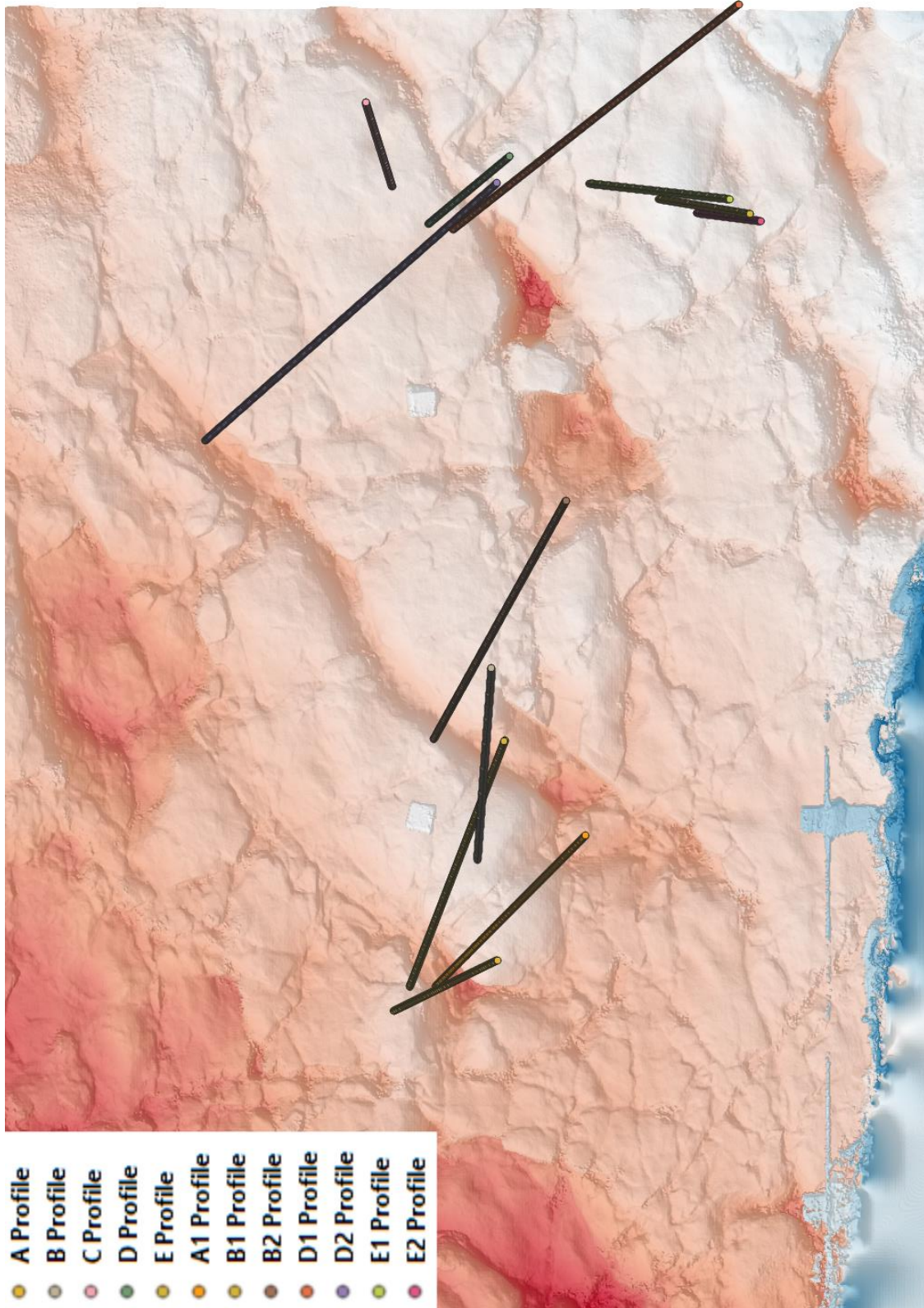
AJG-004 at BBNP – DEM and billow profiles
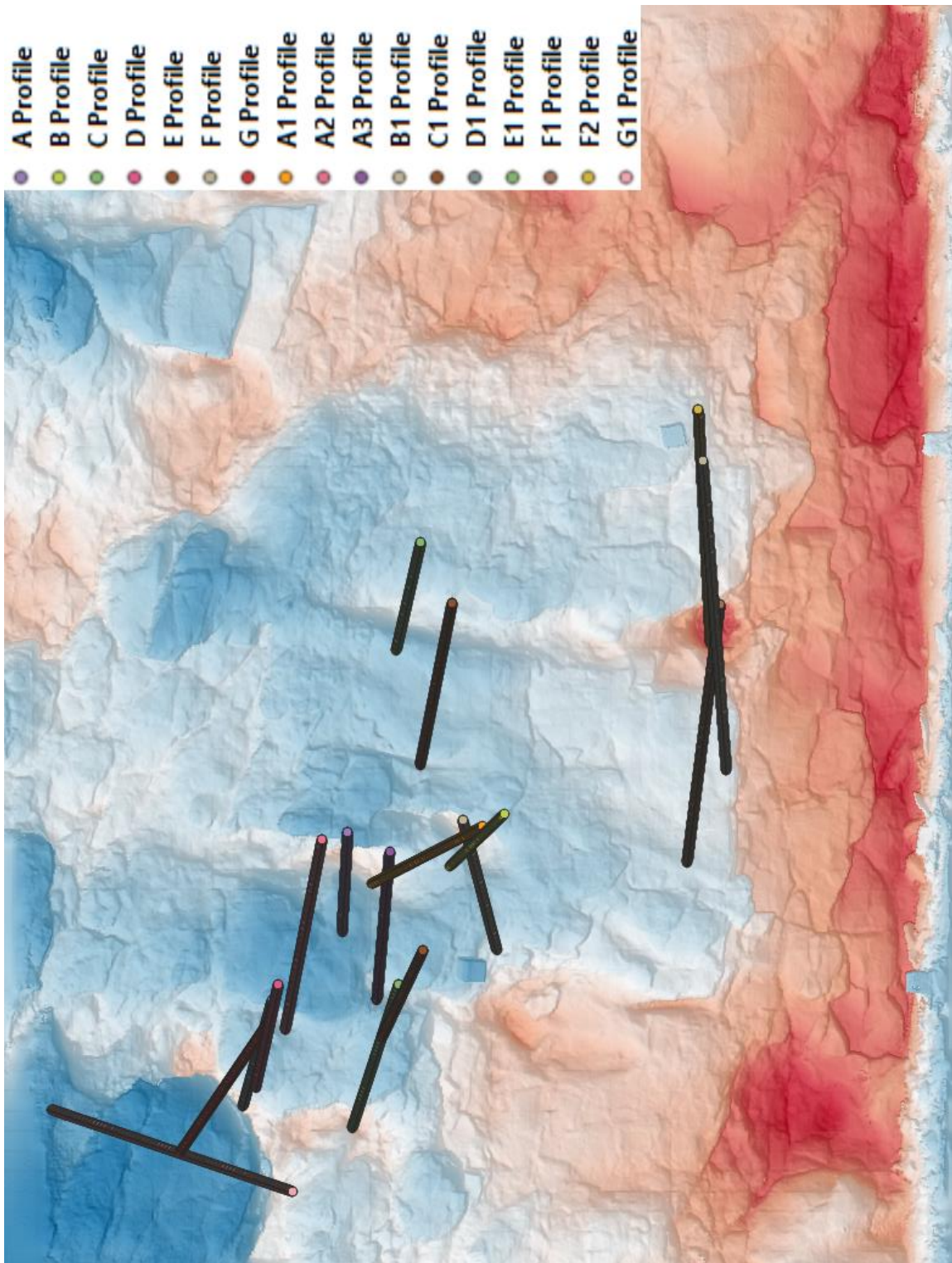
AJG-005 at BBNP – DEM and billow profiles

114
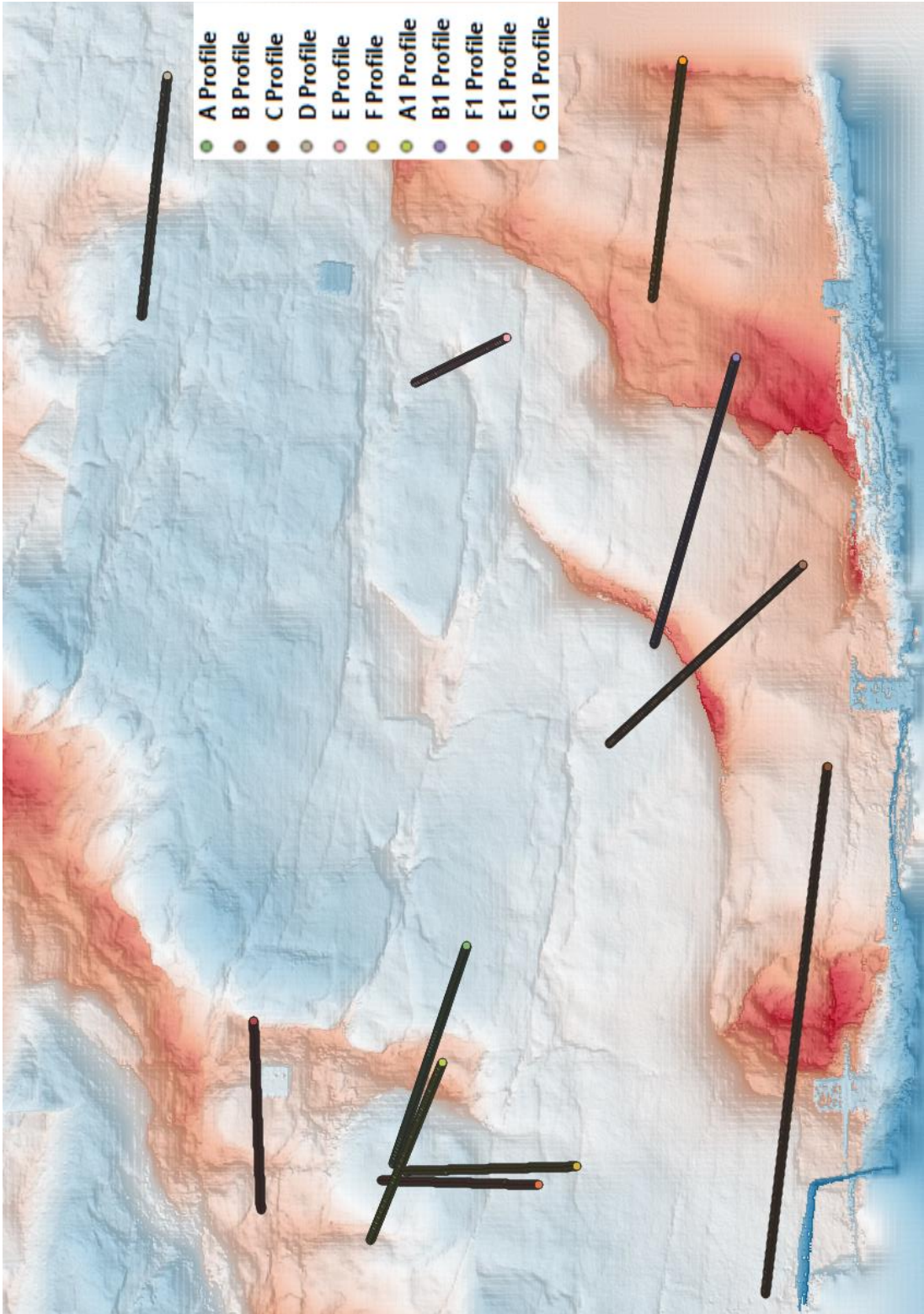
AJG-006 at BBNP – DEM and billow profiles
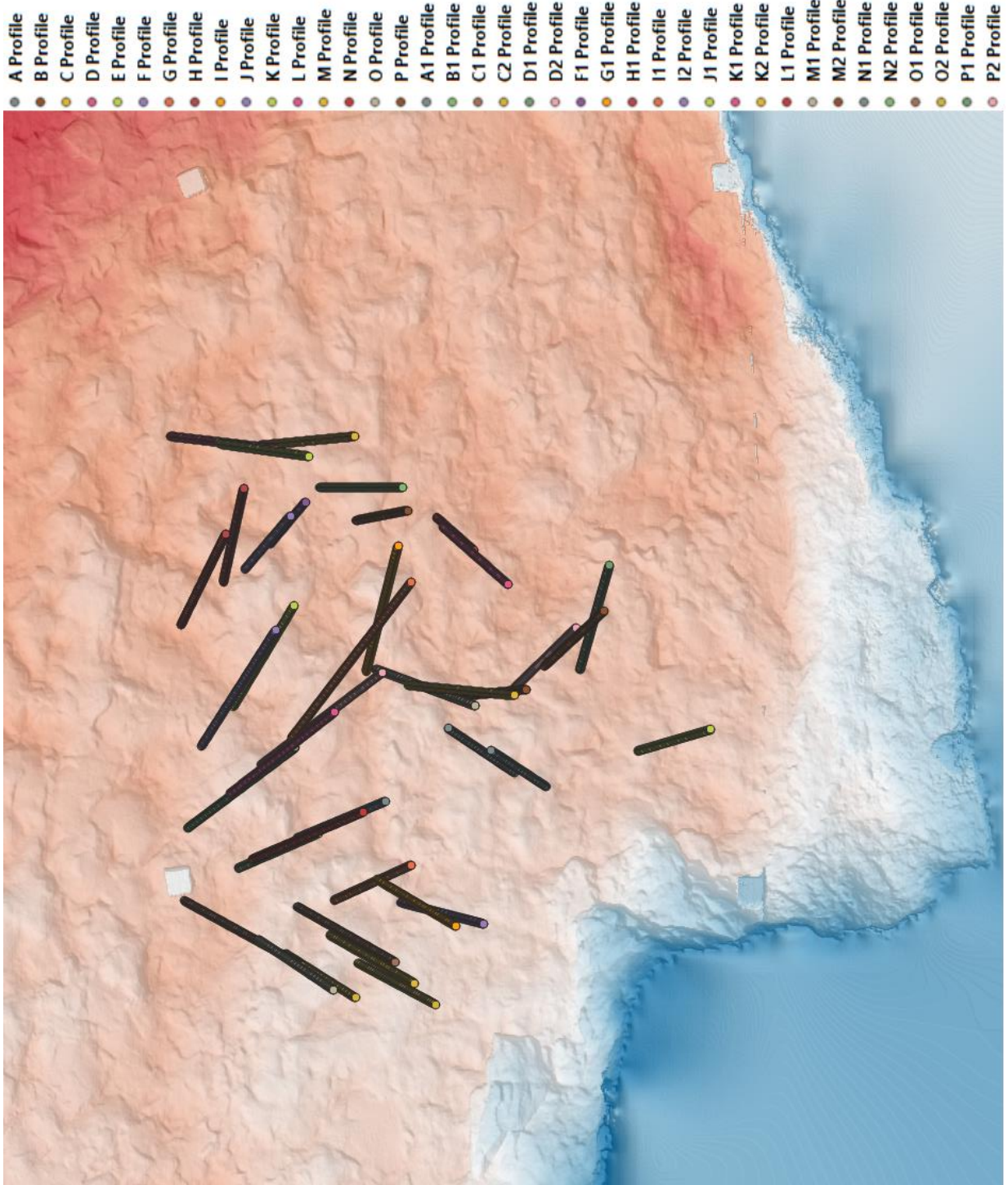
AJG-007 at BBNP – DEM and billow profiles
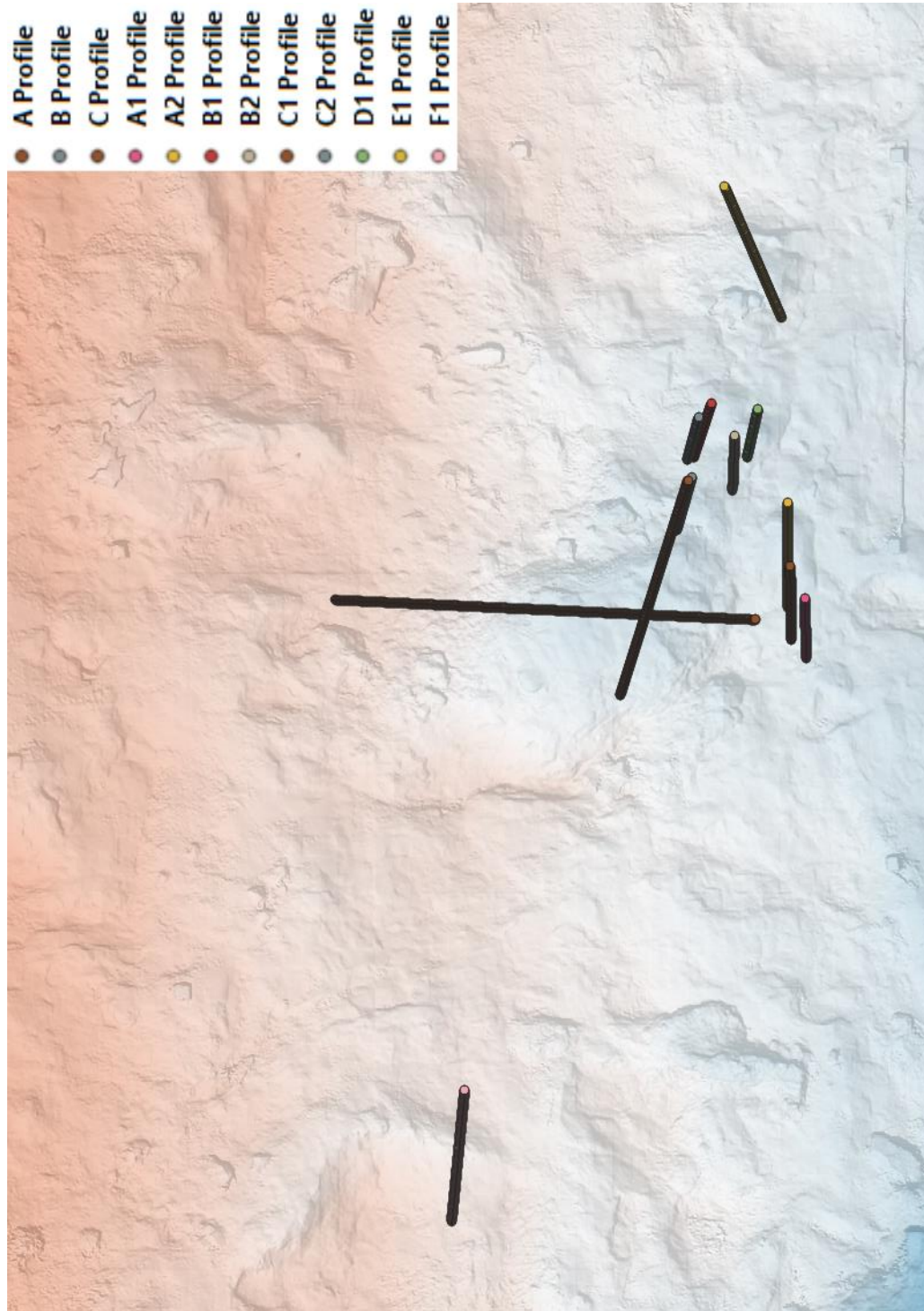
AJG-008 at BBNP – DEM and billow profiles
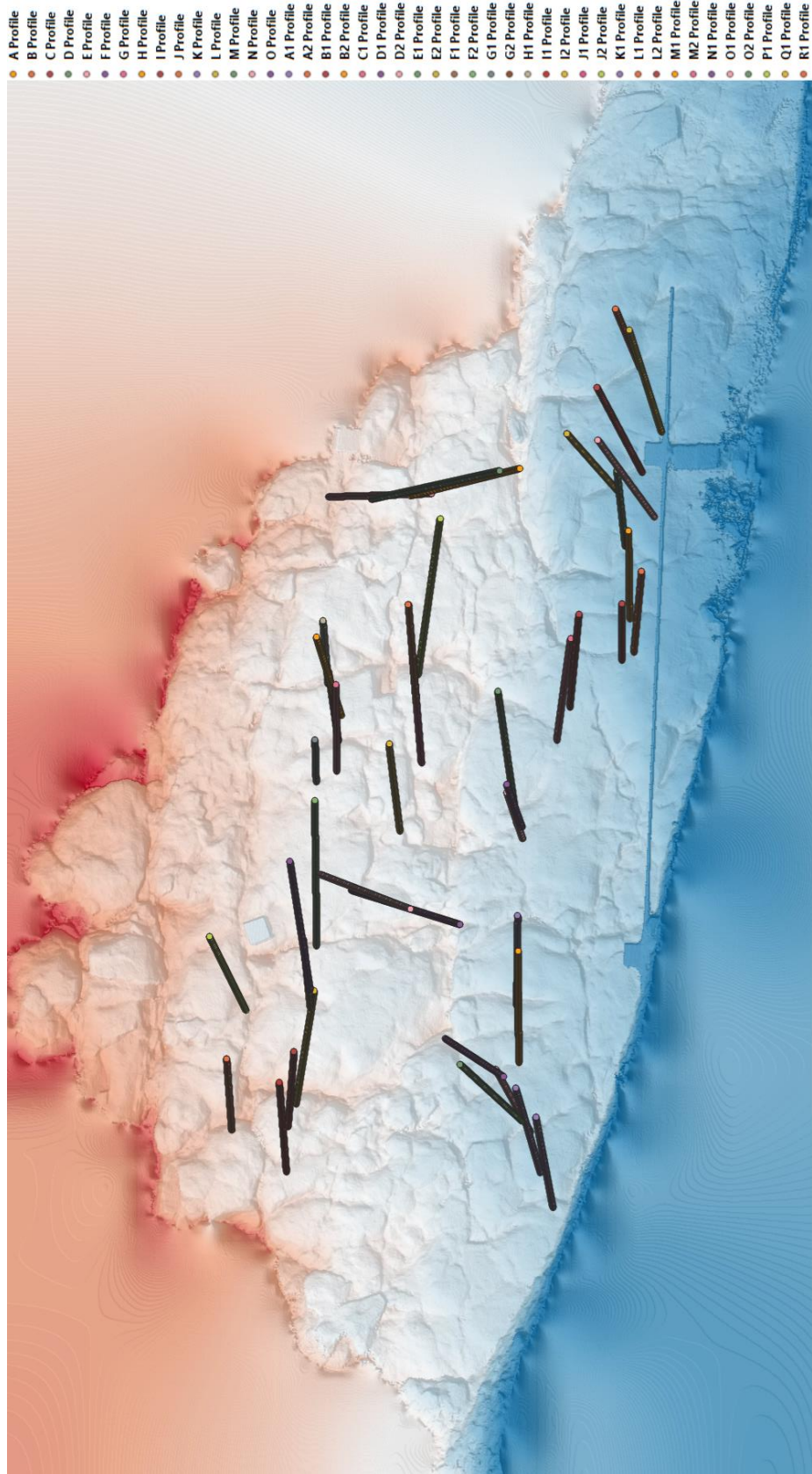
AJG-011 at BBNP – DEM and billow profiles

AJG-012 at BBNP – DEM and billow profiles
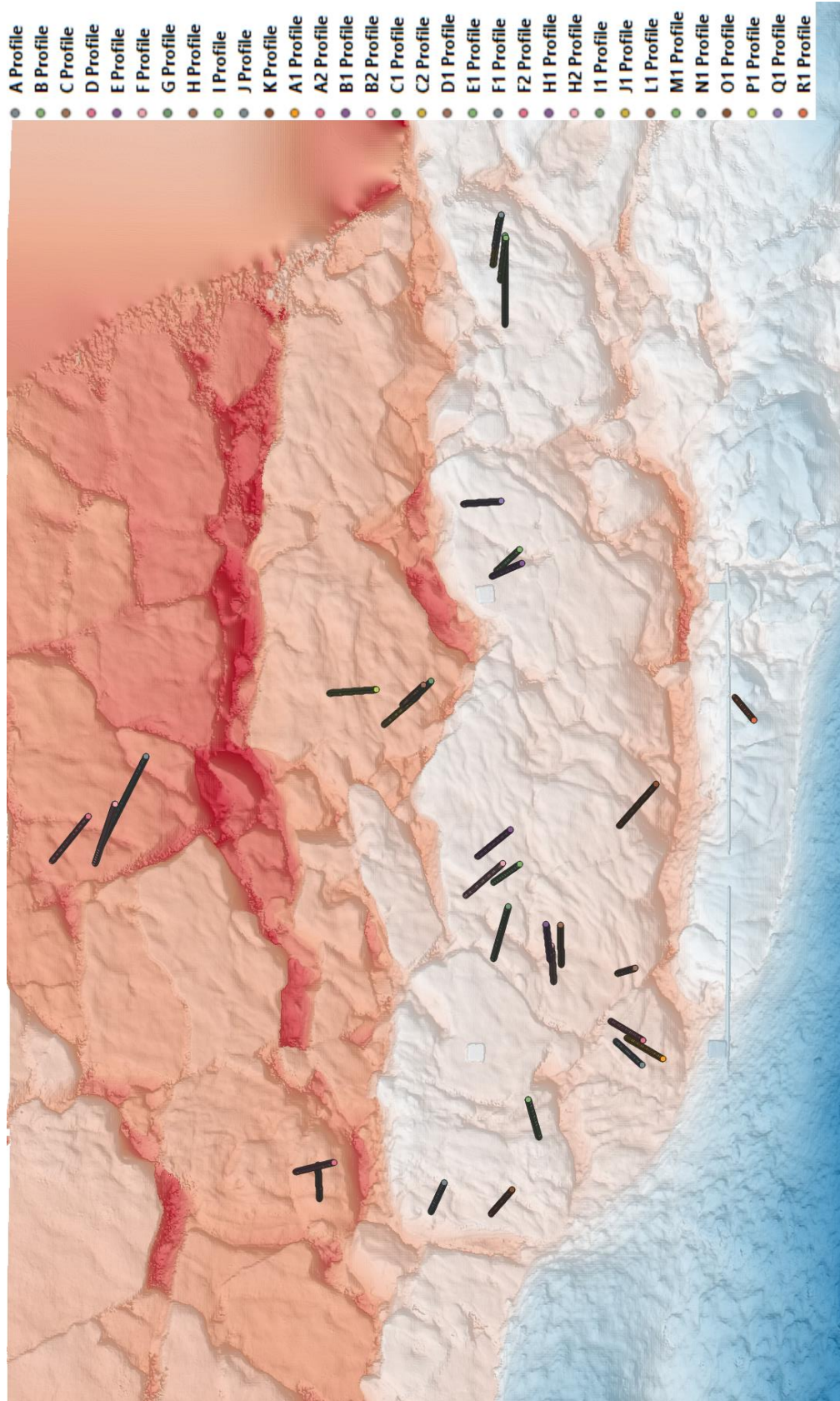
AJG-013 at BBNP – DEM and billow profiles

120
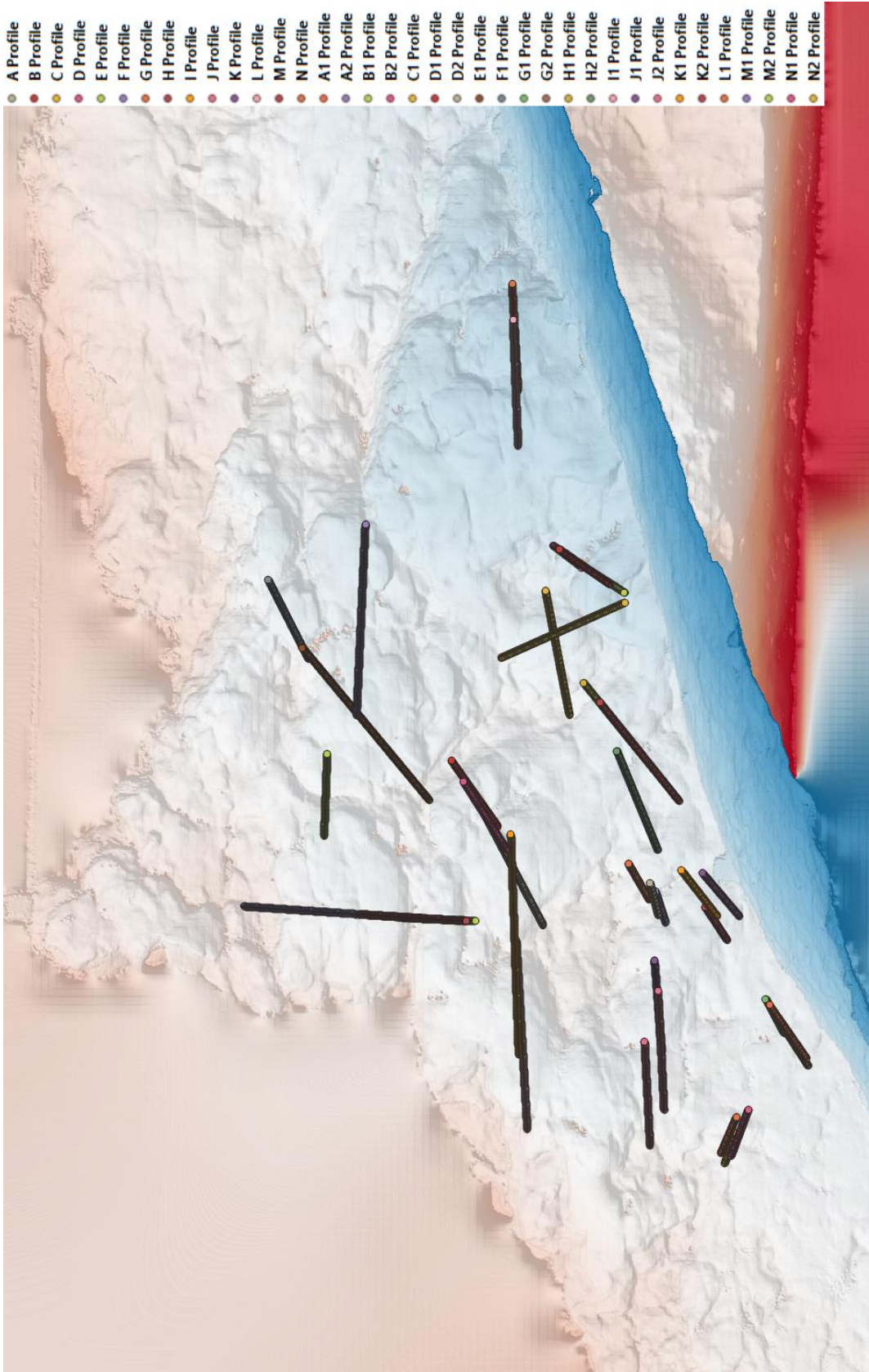
AJG-017 East at BBNP – DEM and billow profiles
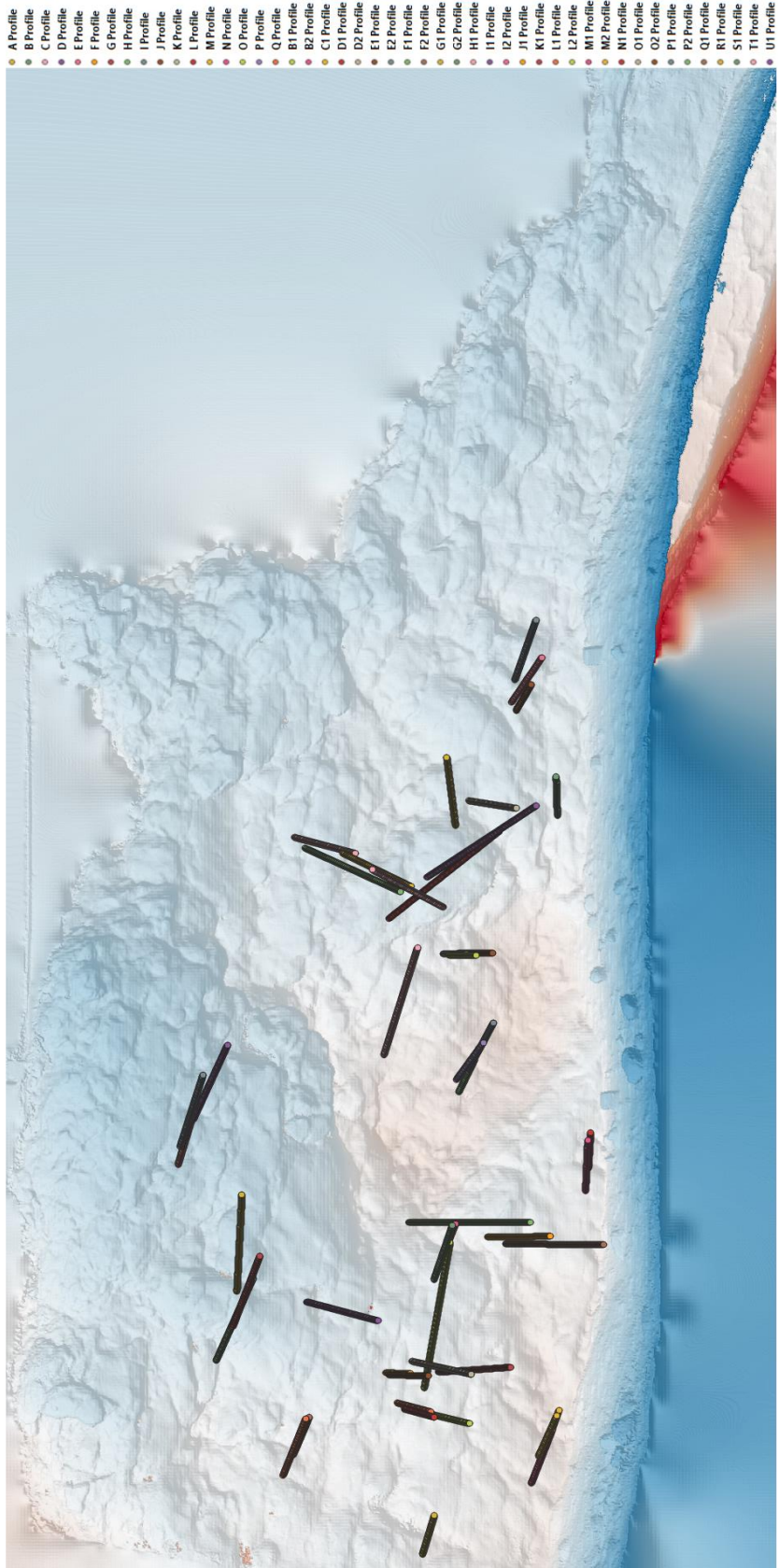
AJG-017 West at BBNP – DEM and billow profiles
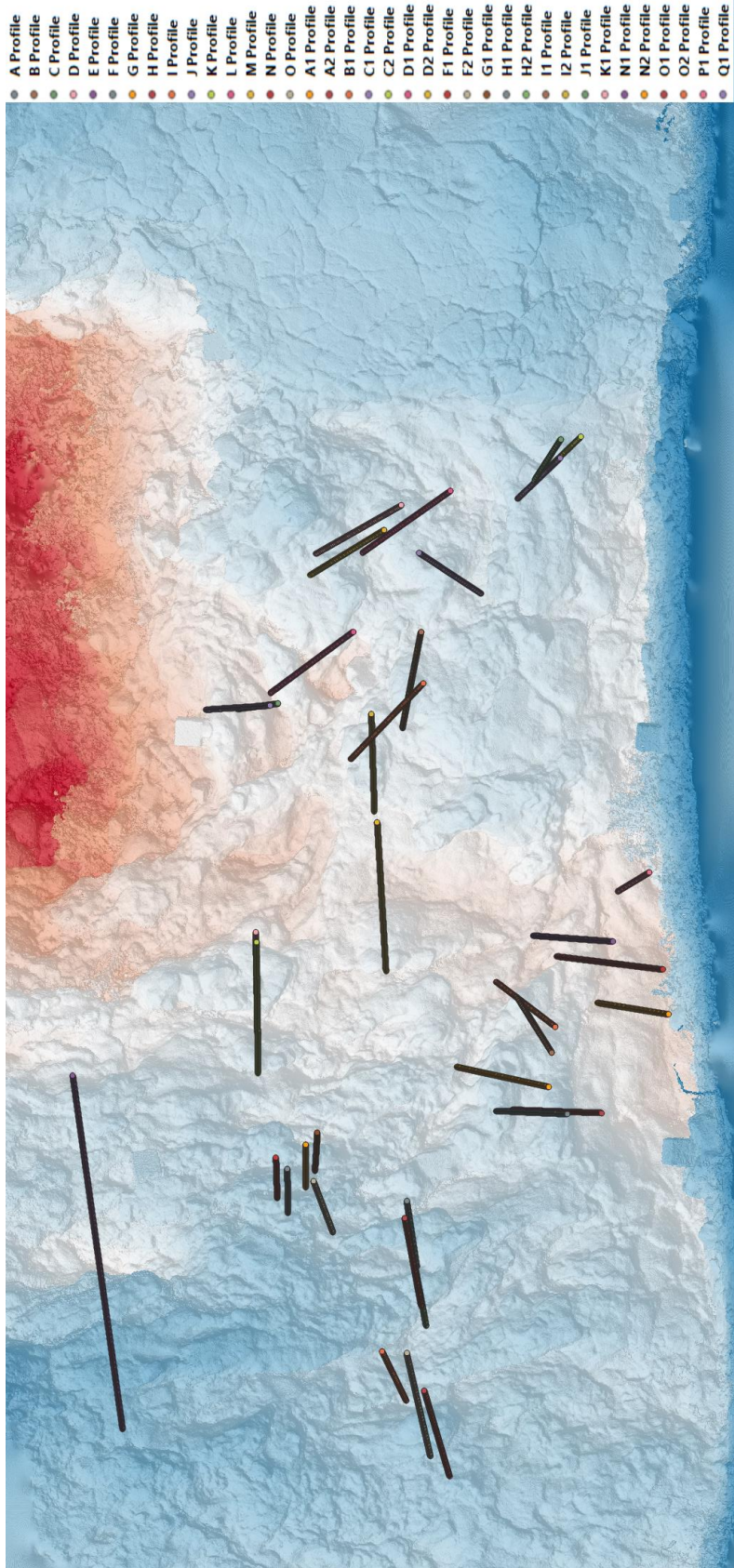
71G002 at 71 Gulch – DEM and billow profiles
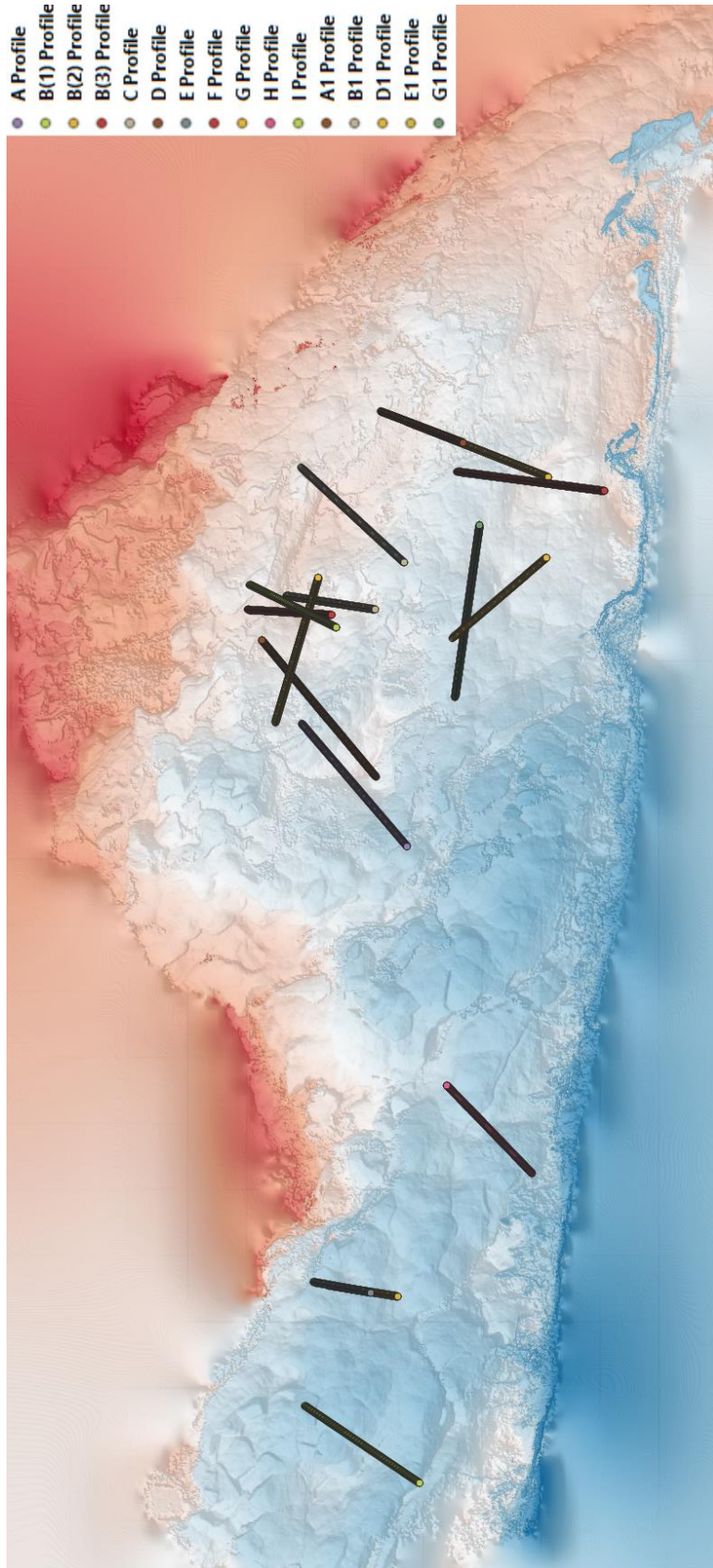
71G018 at 71 Gulch – DEM and billow profiles

A Profile B Profile C Profile D Profile E Profile F Profile G Profile H Profile A1 Profile B1 Profile B2 Profile C1 Profile D1 Profile D2 Profile E1 Profile F1 Profile F2 Profile G1 Profile G2 Profile I1 Profile J1 Profile K1 Profile L1 Profile M1 Profile
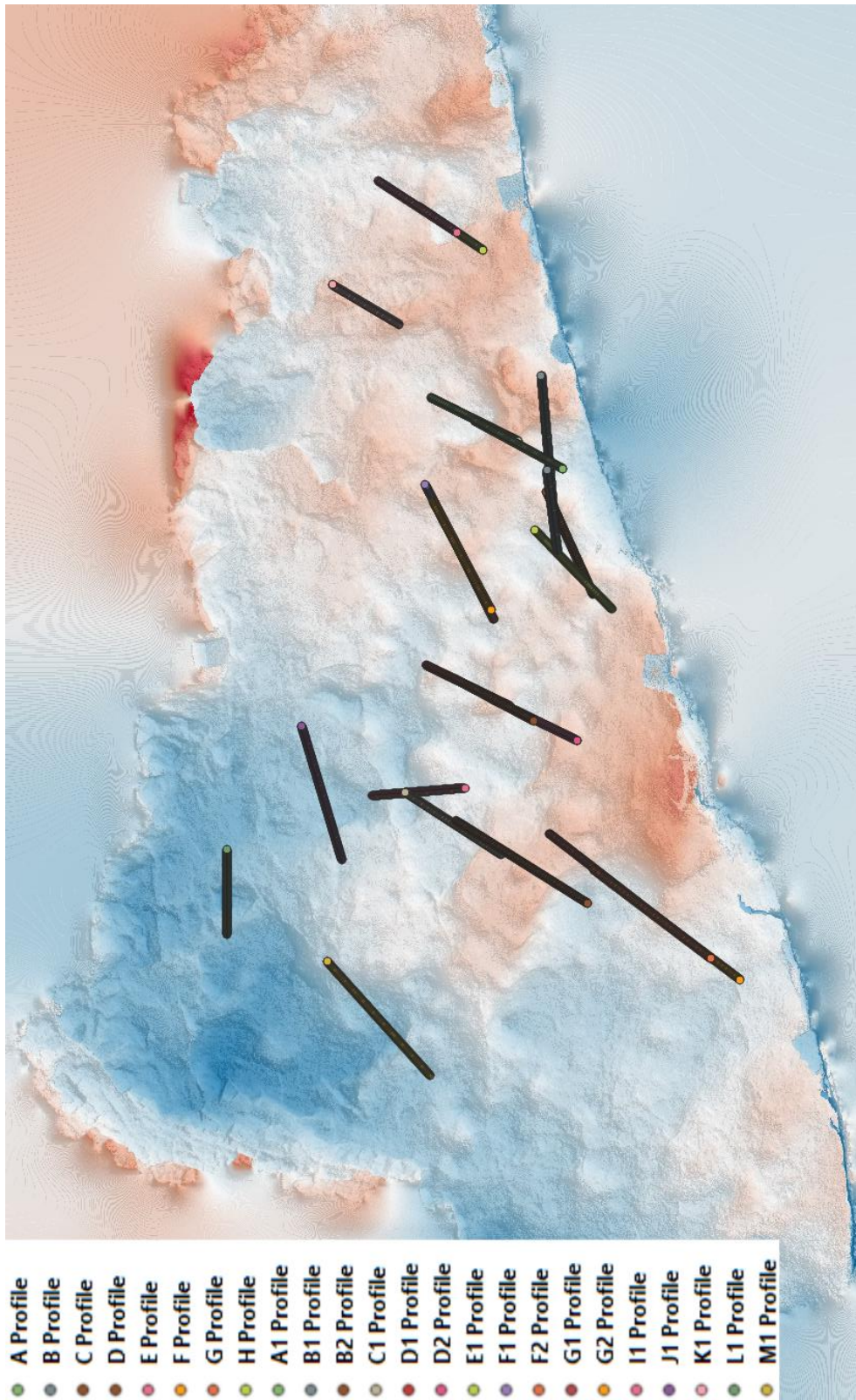
71G019-1 at 71 Gulch – DEM and billow profiles
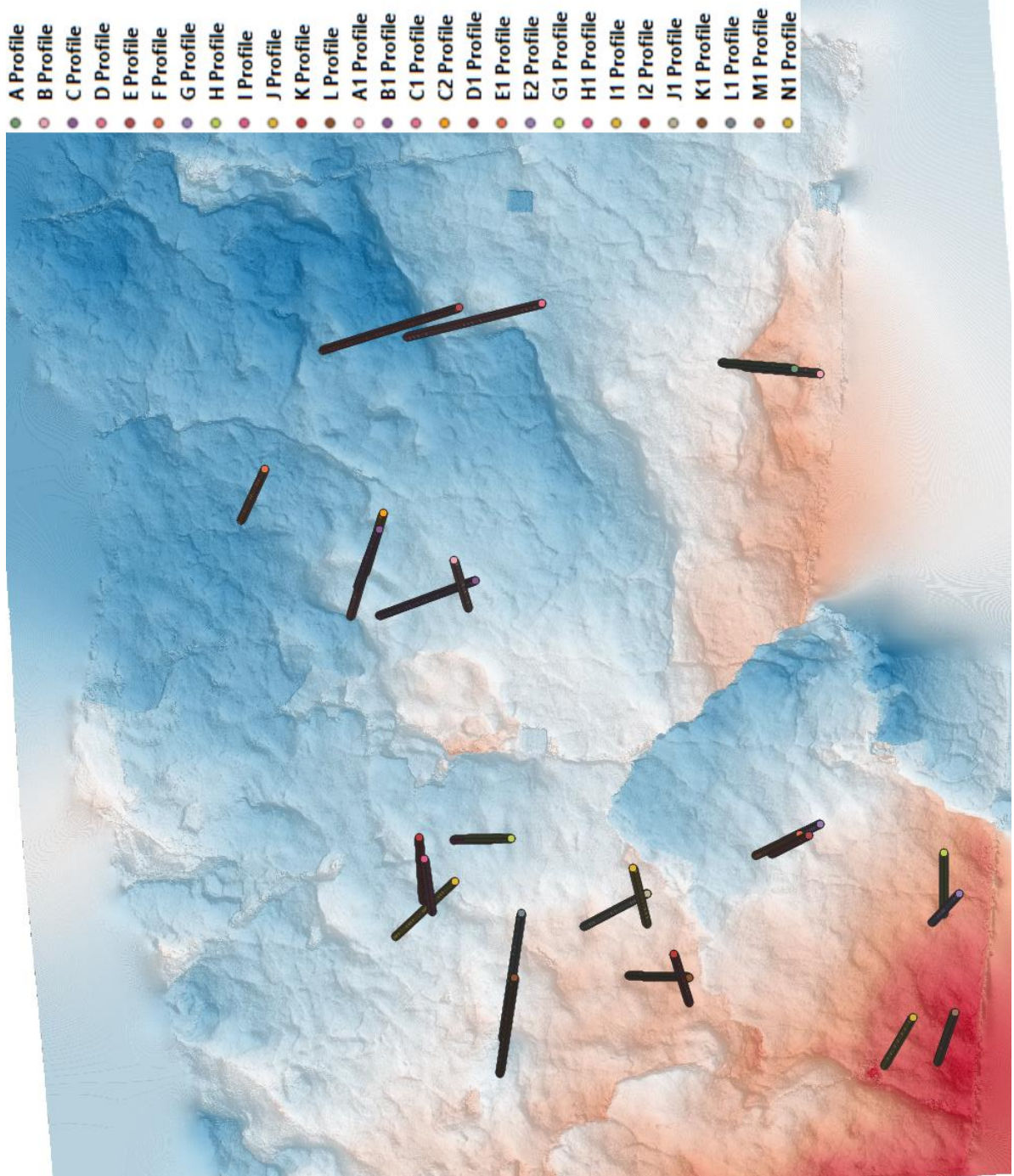
71G019-2 at 71 Gulch – DEM and billow profiles
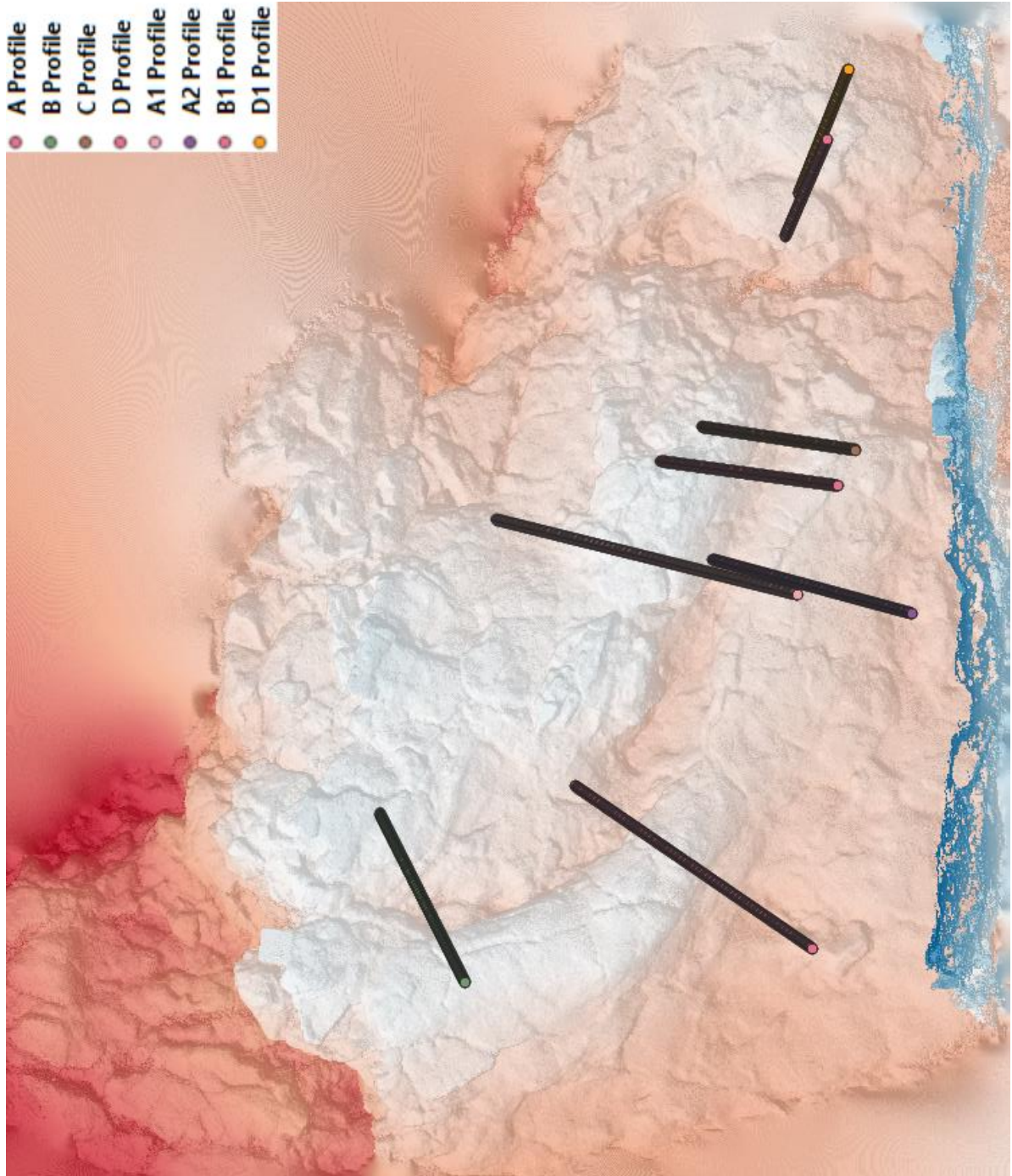
71G032 at 71 Gulch – DEM and billow profiles
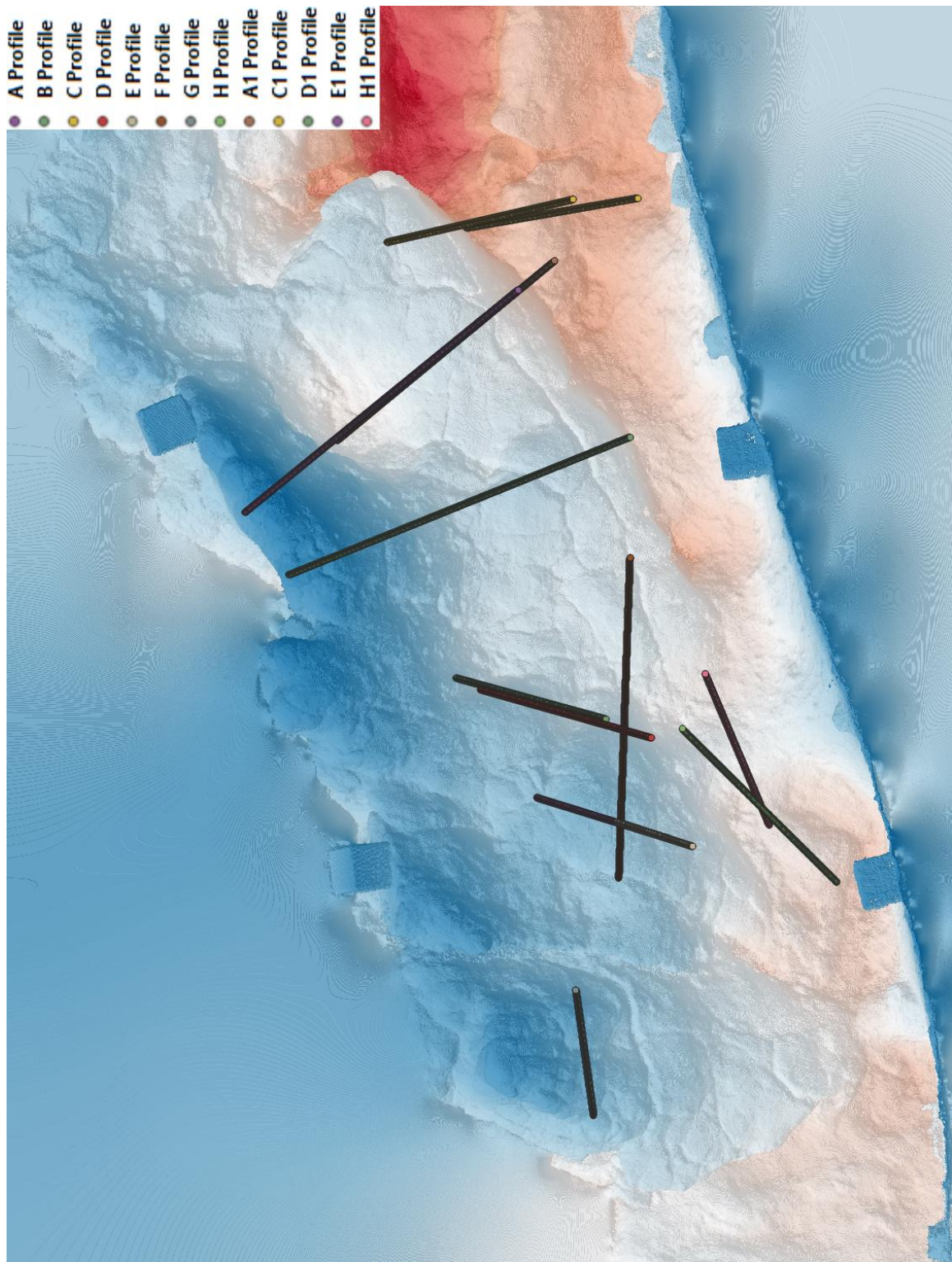
AJG-7101 at 71 Gulch – DEM and billow profiles

A Profile ● B Profile ● C Profile ● D Profile ● E Profile ● F Profile ● G Profile ● H Profile ● A1 Profile ● A2 Profile ● B1 Profile ● C1 Profile ● C2 Profile ● D1 Profile ● E1 Profile ● E2 Profile ● G1 Profile ● I1 Profile ●
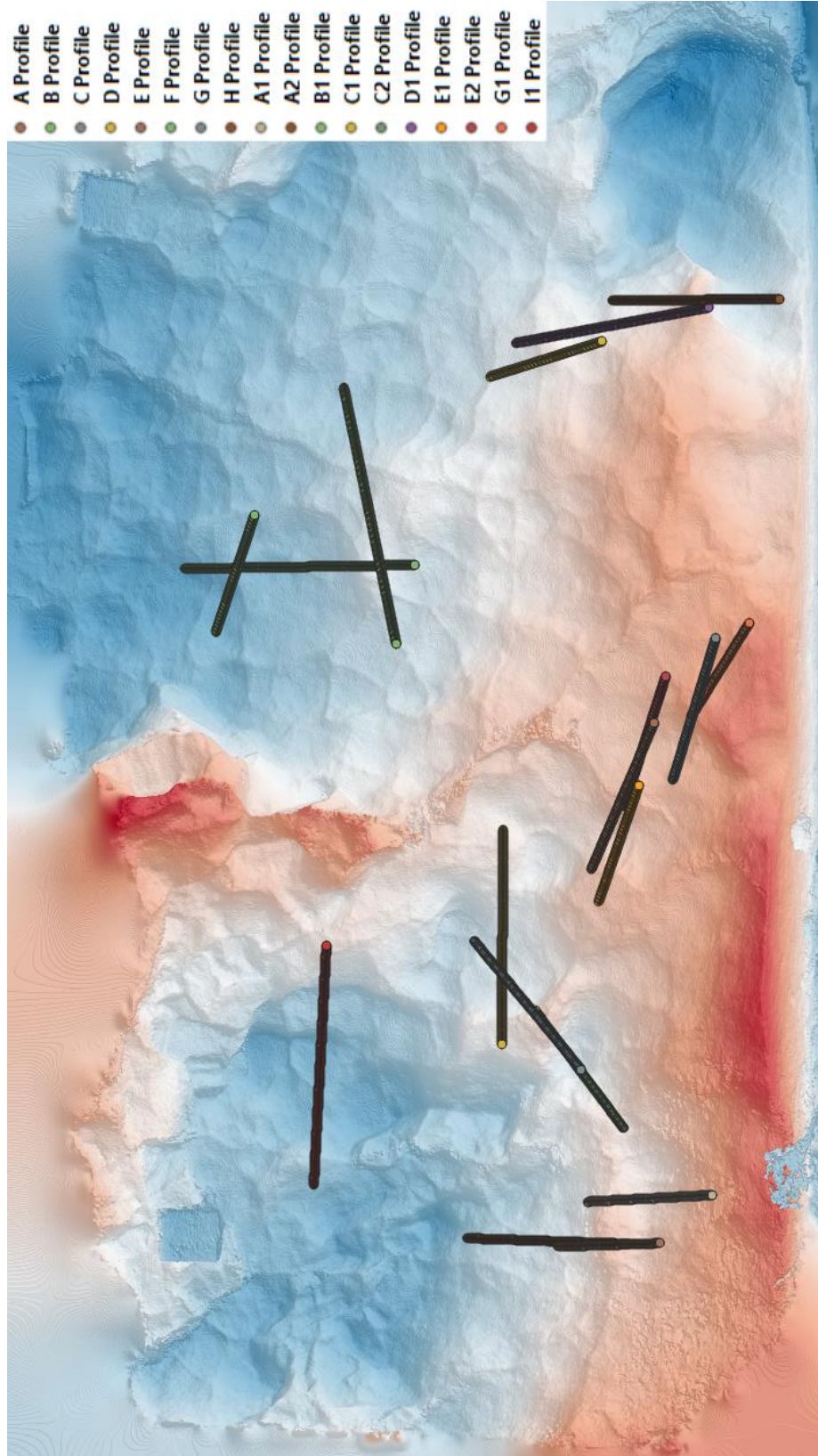
AJG-7102 at 71 Gulch – DEM and billow profiles
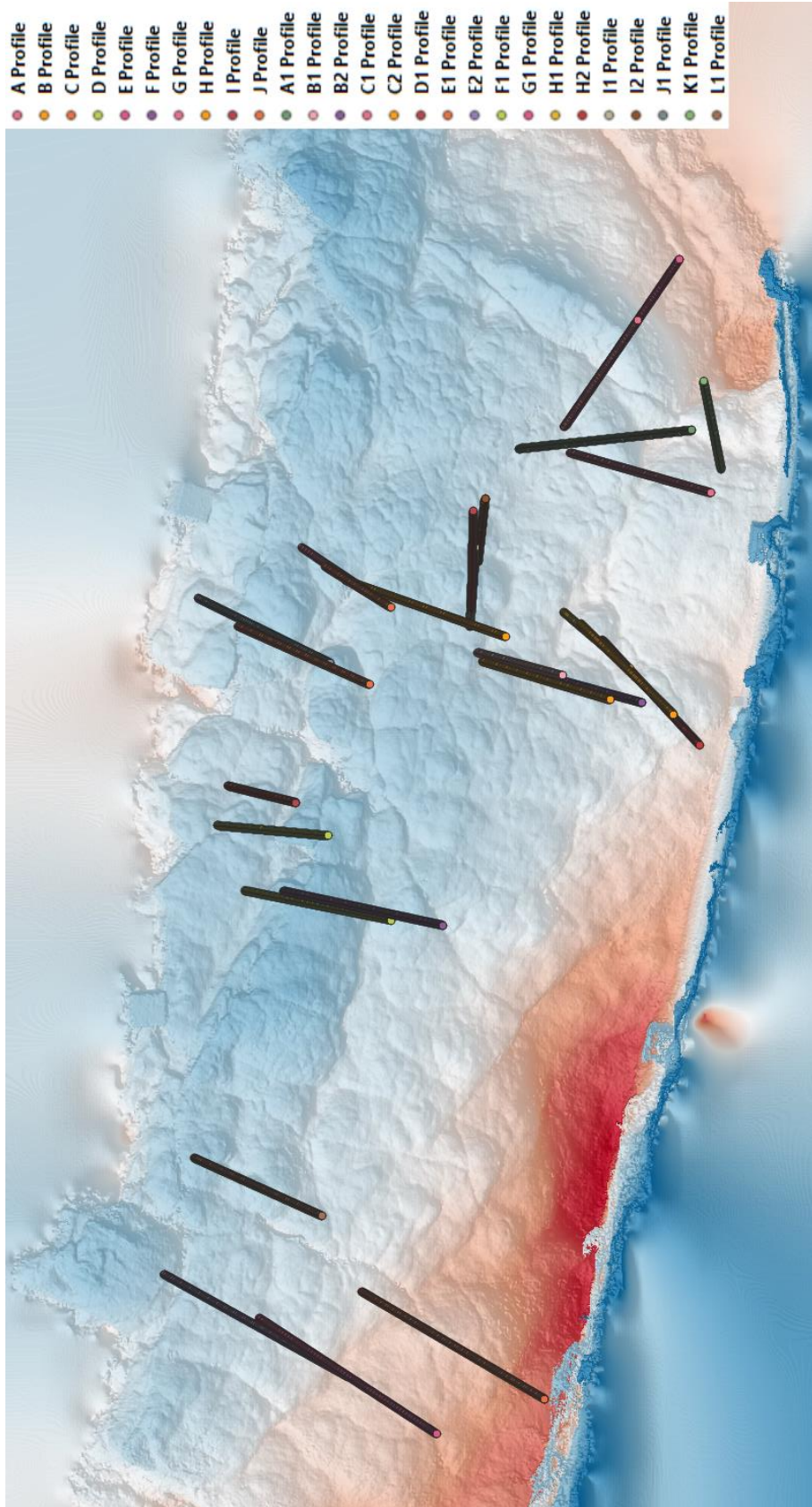
AJG-7103 at 71 Gulch – DEM and billow profiles
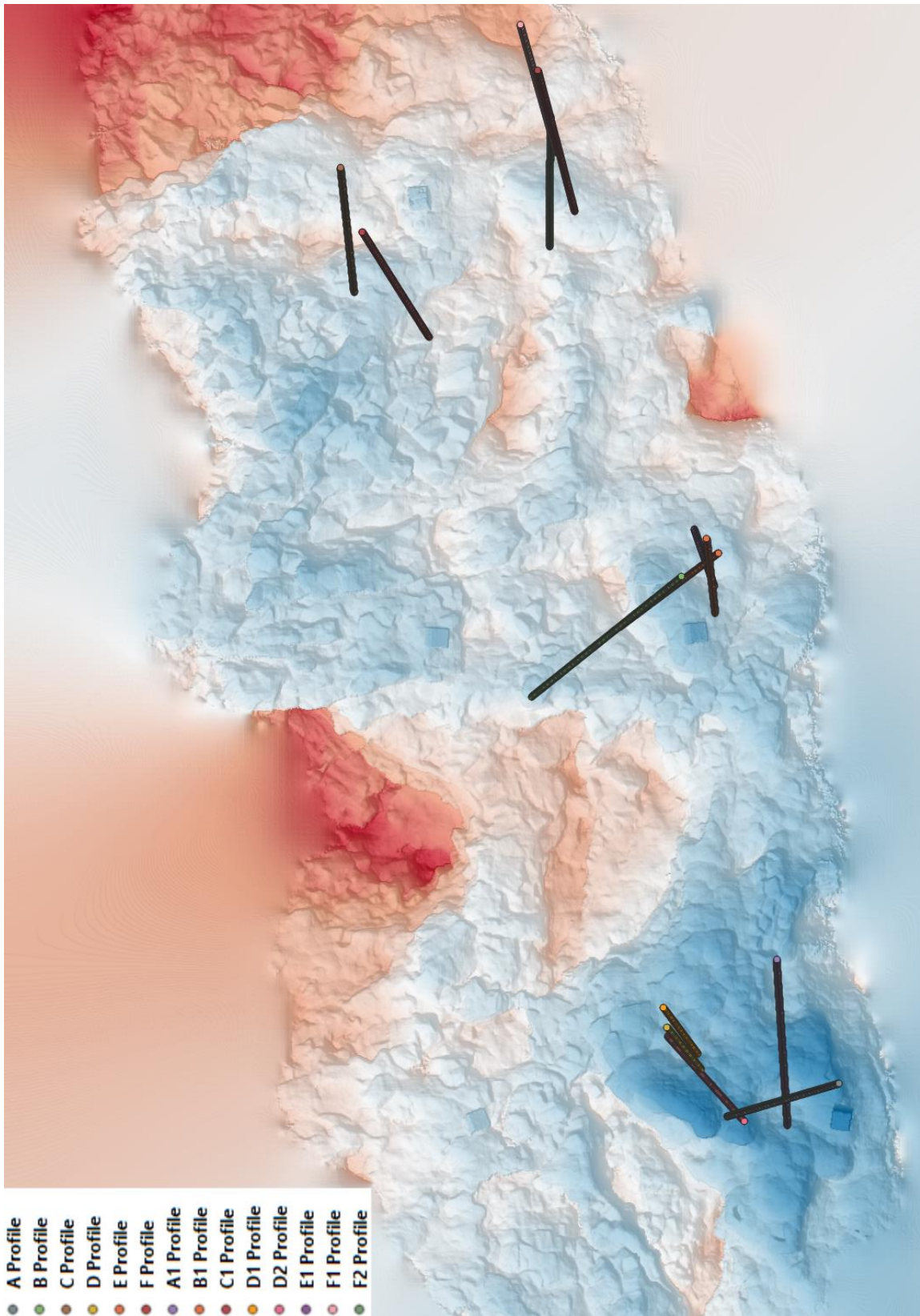
AJG-7104 at 71 Gulch – DEM and billow profiles
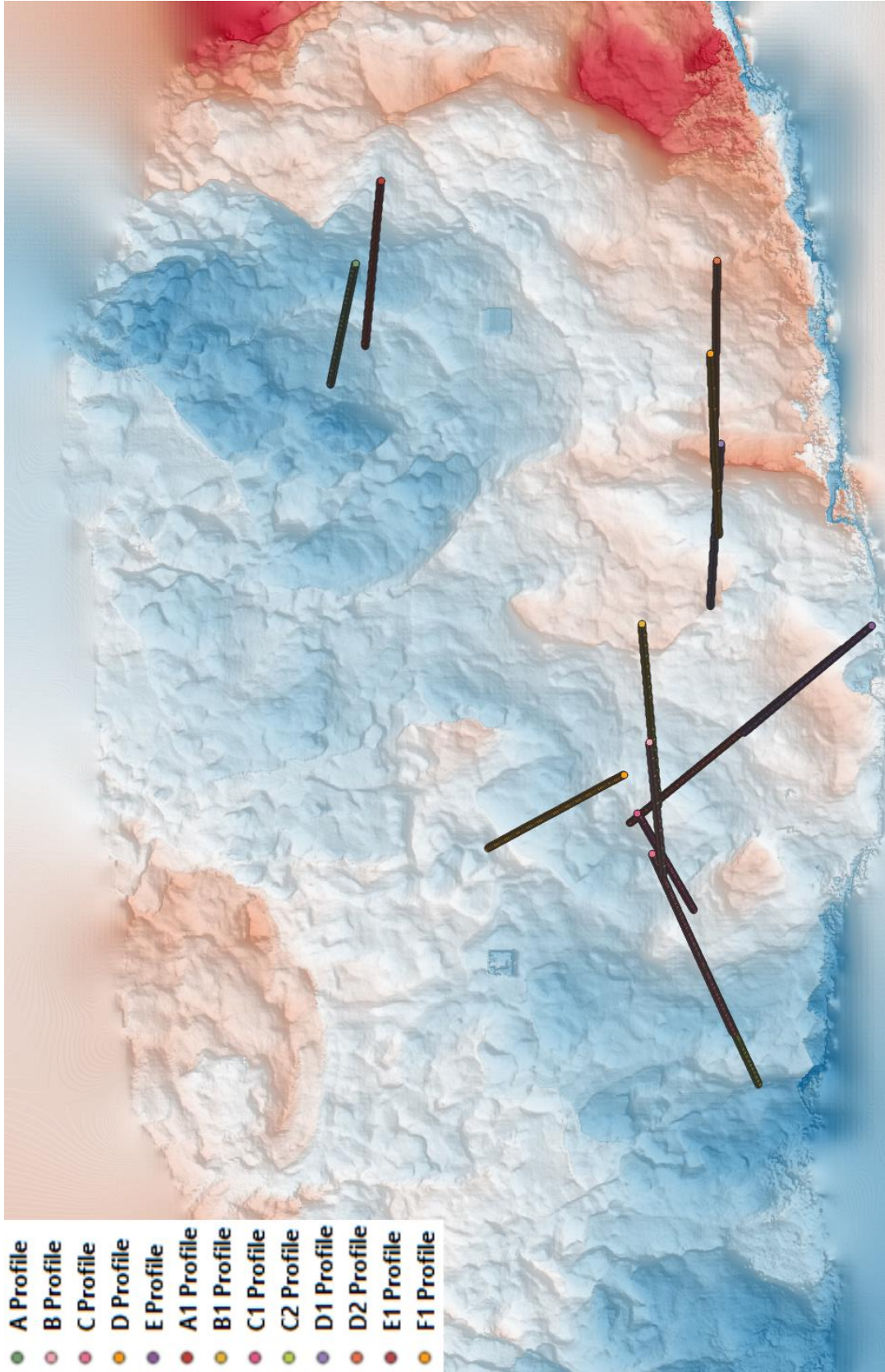
AJG-7105 at 71 Gulch – DEM and billow profiles

REFERENCES

Barker, D.S., 1987. Tertiary alkaline magmatism in Trans-Pecos Texas. Geol. Soc. Spec.

Publ. 30, 415–431. https://doi.org/10.1144/GSL.SP.1987.030.01.20

Befus, K.S., Hanson, R.E., Lehman, T.M., Griffin, W.R., 2008. Cretaceous basaltic

phreatomagmatic volcanism in West Texas: Maar complex at Peña Mountain, Big Bend

National Park. J. Volcanol. Geotherm. Res. 173, 245–264.

https://doi.org/10.1016/j.jvolgeores.2008.01.021

Befus, K.S., Hanson, R.E., Miggins, D.P., Breyer, J.A., Busbey, A.B., 2009. Nonexplosive

and explosive magma/wet-sediment interaction during emplacement of Eocene

intrusions into Cretaceous to Eocene strata, Trans-Pecos igneous province, West Texas.

J. Volcanol. Geotherm. Res. 181, 155–172.

https://doi.org/10.1016/j.jvolgeores.2008.12.017

Bennis, K.L., 2019. Reconstructing the 71 Gulch Eruption: Implications for the Evolution of

Phreatomagmatic Eruptions and Their Products. University of Missouri - Kansas City.

Masters thesis.

Bennis, K.L., Graettinger, A.H., 2020. Basaltic phreatomagmatic fissure at 71 Gulch Part 1:

sediment magma mingling and eruptive behavior. Bull. Volcanol. 82, 1–17.

https://doi.org/10.1007/s00445-020-01416-1

Bonnichsen, B., 1982. The Bruneau-Jarbidge eruptive center, southwestern Idaho, in:

Cenozoic Geology of Idaho: Idaho Bureau of Mines and Geology Bulletin. pp. 237–254.

Bonnichsen, B., Godchaux, M.M., 2002. Late Miocene, Pliocene, and Pleistocene geology of southwestern Idaho with emphasis on basalts in the Bruneau-Jarbidge, Twin Falls, and western Snake River Plain regions. Tecton. Magmat. Evol. Snake River Plain Volcan. Prov. Idaho Geol. Surv. Bull. 30, 233–312.

Bonnichsen, B., Leeman, W.P., Honjo, N., McIntosh, W.C., Godchaux, M.M., 2008. Miocene silicic volcanism in southwestern Idaho: Geochronology, geochemistry, and evolution of the central Snake River Plain. Bull. Volcanol. 70, 315–342. https://doi.org/10.1007/s00445-007-0141-6

Bottinga, Y., Weill, D.F., 1970. Densities of liquid silicate systems calculated from partial molar volumes of oxide components. Am. J. Sci. 269, 169-182. https://doi.org/10.2475/ajs.269.2.169

Brand, B.D., White, C.M., 2007. Origin and stratigraphy of phreatomagmatic deposits at the Pleistocene Sinker Butte Volcano, Western Snake River Plain, Idaho. J. Volcanol. Geotherm. Res. 160, 319–339. https://doi.org/10.1016/j.jvolgeores.2006.10.007

Breyer, J.A., Busbey, A.B., Hanson, R.E., Befus, K.E., Griffin, W.R., Hargrove, U.S., Bergman, S.C., 2007. Evidence for Late Cretaceous volcanism in Trans-Pecos Texas. J. Geol. 115, 243–251. https://doi.org/10.1086/510640

Büttner, R., Dellino, P., La Volpe, L., Lorenz, V., Zimanowski, B., 2002. Thermohydraulic explosions in phreatomagmatic eruptions as evidenced by the comparison between pyroclasts and products from Molten Fuel Coolant Interaction experiments. J. Geophys. Res. Solid Earth 107, ECV 5-1-ECV 5-14. https://doi.org/10.1029/2001jb000511

Casas, D., Pimentel, A., Pacheco, J., Martorelli, E., Sposato, A., Ercilla, G., Alonso, B., Chiocci, F., 2018. Serreta 1998–2001 submarine volcanic eruption, offshore Terceira (Azores): Characterization of the vent and inferences about the eruptive dynamics. J. Volcanol. Geotherm. Res. 356, 127–140. https://doi.org/10.1016/j.jvolgeores.2018.02.017

Chanceaux, L., Menand, T., 2016. The effects of solidification on sill propagation dynamics and morphology. Earth Planet. Sci. Lett. 442, 39–50. https://doi.org/10.1016/j.epsl.2016.02.044

Drazin, P.G., 2015. DYNAMIC METEOROLGY | Kelvin-Helmholtz Instability. In: Encyclopedia of Atmospheric Sciences (Second Edition). Academic Press, pp. 343–346. https://doi.org/10.1016/B978-0-12-382225-3.00190-0

Debone, K.N., 2020. Paleocene basaltic phreatomagmatic volcanic complex in Big Bend National Park, West Texas. Texas Christian University. Masters thesis.

Einarsson, P., Brandsdottir, B., 1980. Seismological evidence for lateral magma intrusion during the July 1978 deflation of the Krafla volcano in NE- Iceland. J. Geophys. - Zeitschrift fur Geophys. 47, 160–165. https://doi.org/10.2172/890964

English, J.M., Johnston, S.T., Wang, K., 2003. Thermal modelling of the Laramide orogeny: Testing the flat-slab subduction hypothesis. Earth Planet. Sci. Lett. 214, 619–632. https://doi.org/10.1016/S0012-821X(03)00399-6

Fink, J.H., Fletcher, R.C., 1978. Ropy pahoehoe: Surface folding of a viscous fluid. J. Volcanol. Geotherm. Res. 4, 151–170. https://doi.org/10.1016/0377-0273(78)90034-3

Godchaux, M.M., Bonnichsen, B., Jenks, M.D., 1992. Types of phreatomagmatic volcanoes in the western Snake River Plain, Idaho, USA. J. Volcanol. Geotherm. Res. 52, 1–25. https://doi.org/10.1016/0377-0273(92)90130-6

Gregg, T.K.P., Fink, J.H., 1995. Quantification of submarine lava-flow morphology through analog experiments. Geology 23, 73–76. https://doi.org/10.1130/0091-7613(1995)023<0073:QOSLFM>2.3.CO;2

Gregg, T.K.P., Fink, J.H., 2000. A laboratory investigation into the effects of slope on lava flow morphology. J. Volcanol. Geotherm. Res. 96, 145–159. https://doi.org/10.1016/S0377-0273(99)00148-1

Griffin, W.R., Foland, K.A., Stern, R.J., Leybourne, M.I., 2010. Geochronology of bimodal alkaline volcanism in the Balcones igneous province, Texas: Implications for Cretaceous intraplate magmatism in the northern Gulf of Mexico magmatic zone. J. Geol. 118, 1–21. https://doi.org/10.1086/648532

Gudmundsson, A., 1984. Formation of dykes, feeder-dykes, and the intrusion of dykes from magma Chambers. Bull. Volcanol. 47, 537–550. https://doi-org.proxy.library.umkc.edu/10.1007/BF01961225

Hanson, R.E., Hargrove, U.S., 1999. Processes of magma/wet sediment interaction in a large-scale Jurassic andesitic peperite complex, northern Sierra Nevada, California. Bull. Volcanol. 60, 610–626. https://doi.org/10.1007/s004450050255

Henry, C.D., McDowell, F.W., 1986. Geochronology of magmatism in the Tertiary volcanic field, Trans-Pecos Texas. Guideb. - Bur. Econ. Geol. Univ. Texas Austin 23, 99–122.

Henry, C.D., Johnathan G. Price, Eric W. James, 1991. Mid-Cenozoic Stress Evolution and Magmatism in the Southern Cordillera, Texas and Mexico: Transition from Continental Arc to Intraplate Extension. J. Geophys. Res. 96, 13,545-13,560.

Hickman, R.G., Varga, R.J., Altany, R.M., 2009. Structural style of the Marathon thrust belt, West Texas. J. Struct. Geol. 31, 900–909. https://doi.org/10.1016/j.jsg.2008.02.016

Hill, J.A., 2014. Complex Eocene-Oligocene hypabyssal intrusive systems associated with basaltic phreatomagmatic vents in the area east of Pena Mountain, Big Bend National Park, Texas. Texas Christian University. Masters thesis

Kano, K., 2002. Middle Miocene volcaniclastic dikes at Kukedo, Shimane Peninsula, SW Japan: Fluidization of volcaniclastic beds by emplacement of syn-volcanic andesitic dikes. J. Volcanol. Geotherm. Res. 114, 81–94. https://doi.org/10.1016/S0377-0273(01)00283-9

Kawachi, Y., Pringle, I.J., 1988. Multiple-rind structure in pillow lava as an indicator of shallow water. Bulletin of Volcanology 50, 161–168. https://doi.org/10.1007/BF01079680

Lavine, A., Aalto, K.R., 2002. Morphology of a crater-filling lava lake margin, the Peninsula tuff cone, Tule Lake National Wildlife Refuge, California: Implications for formation of peperite textures. J. Volcanol. Geotherm. Res. 114, 147–163. https://doi.org/10.1016/S0377-0273(01)00285-2

Leeman, W.P., 1982. Development of the Snake River Plain-Yellowstone Plateau province, Idaho and Wyoming: an overview and petrologic model. Cenozoic Geol. Idaho Idaho Bur. Mines Geol. Bull. 26 26, 155–177.

Lehman, T.M., 1991. Sedimentation and tectonism in the Laramide tornillo basin of West Texas. Sediment. Geol. 75, 9–28. https://doi.org/10.1016/0037-0738(91)90047-H

Lowe, D.G., 2004. Distinctive image features from scale-invariant keypoints. Int. J. Comput. Vis. 60, 91–110. https://doi.org/10.1023/B:VISI.0000029664.99615.94

Malde, H.E., Powers, H.A., 1962. Upper Cenozoic Stratigraphy of Western Snake River Plain, Idaho. Bull. Geol. Soc. Am. 73, 1197–1220. https://doi.org/10.1130/0016-7606(1962)73[1197:UCSOWS]2.0.CO;2

Malde, H.E., 1991. Quaternary geology and structural history of the Snake River Plain, Idaho and Oregon, in: The Geology of North America. Denver, CO, pp. 251–281. https://doi.org/10.1130/dnag-gna-k2.251

Martin, D.M., 2007. The Structural Evolution of the McKinney Hill Laccolith, Big Bend National Park, Texas. Texas Tech University. Texas Tech University. Masters thesis.

Melson, W.G., Thompson, G., 1973. Glassy abyssal basalts, Atlantic sea floor near Saint

    Paul's Rocks: petrography and composition of secondary clay minerals. Geological

    Society of America Bulletin 84, 703–716.

Miggins, D.P., Ren, M., Anthony, E.Y., 2008. Geological, Geochemical, and Geophysical

    Studies by the U.S. Geological Survey in Big Bend National Park, Texas. USGS Circ.

    1397, 93. https://doi.org/10.1130/0016-7606(1973)84<703:GABASF>2.0.CO;2

Németh, K., White, C.M., 2009. Intra-vent peperites related to the phreatomagmatic 71

    Gulch Volcano, western Snake River Plain volcanic field, Idaho (USA). J. Volcanol.

    Geotherm. Res. 183, 30–41. https://doi.org/10.1016/j.jvolgeores.2009.02.020

Németh, K., Kósik, S., 2020. Review of explosive hydrovolcanism. Geosci. 10.

    https://doi.org/10.3390/geosciences10020044

Page, W. R., Turner, K. J., Bohannon, R. G., 2008. Geological, Geochemical, and

    Geophysical Studies by the U.S. Geological Survey in Big Bend National Park, Texas.

    USGS Circular, 1397, pp. 3-13.

Parker, D.F., Ren, M., Adams, D.T., Tsai, H., Long, L.E., 2012. Mid-Tertiary magmatism in

    western Big Bend National Park, Texas, U.S.A.: Evolution of basaltic source regions

    and generation of peralkaline rhyolite. Lithos 144–145, 161–176.

    https://doi.org/10.1016/j.lithos.2012.04.019

Pearce, J.A., 1996. A User's Guide to Basalt Discriminant Diagrams. Geol. Assoc. Canada,

    Short Course Notes.

Peterson, G.L., Hawkins, J.W., 1971. Inclined pipe vesicles as indicators of flow direction in basalts: A critical appraisal. Bull. Volcanol. 35, 369–382. https://doi.org/10.1007/BF02596962

Poole, F.G., Perry, W.J., Madrid, R.J., Amaya-Martinez, R., 2005. Tectonic synthesis of the Ouachita-Marathon-Sonora orogenic margin of southern Laurentia: Stratigraphic and structural implications for timing of deformational events and plate-tectonic model. Spec. Pap. Geol. Soc. Am. 393, 543–596. https://doi.org/10.1130/0-8137-2393-0.543

Poppe, S., Galland, O., Winter, N.J., Goderis, S., Claeys, P., Debaille, V., Boulvais, P., Kervyn, M., 2020. Structural and geochemical interactions between magma and sedimentary host rock: the Hovedøya case, Oslo Rift, Norway. Geochemistry, Geophys. Geosystems 1–22. https://doi.org/10.1029/2019GC008685

Price, J.G., Henry, C.D., Barker, D.S., Parker, D.F., 1987. Alkalic rocks of contrasting tectonic settings in Trans-Pecos Texas, in: Special Paper of the Geological Society of America. pp. 335–346. https://doi.org/10.1130/SPE215-p335

Rowe, T., Cifelli, R.L., Lehman, T.M., Weil, A., 1992. The Campanian Terlingua local fauna, with a summary of other vertebrates from the Aguja Formation, Trans-Pecos Texas. J. Vertebr. Paleontol. 12, 472–493. https://doi.org/10.1080/02724634.1992.10011475

Shaw, H.R., 1972. Viscosities of magmatic silicate liquids; an empirical method of prediction. Am. J. Sci. 272, 870–893. https://doi.org/10.2475/ajs.272.9.870

Shervais, J.W., Shroff, G., Vetter, S.K., Matthews, S., Hanan, B.B., Mcgee, J.J., 2002. Origin and Evolution of the Western Snake River Plain : Implications From Stratigraphy , Faulting , and the Geochemistry of Basalts Near Mountain Home , Idaho. Idaho Geol. Surv. Bull. 343–361.

Skilling, I.P., White, J.D.L., McPhie, J., 2002. Peperite: A review of magma-sediment mingling. J. Volcanol. Geotherm. Res. 114, 1–17. https://doi.org/10.1016/S0377-0273(01)00278-5

Sonder, I., Harp, A.G., Graettinger, A.H., Moitra, P., Valentine, G.A., Büttner, R., Zimanowski, B., 2018. Meter-Scale Experiments on Magma-Water Interaction. J. Geophys. Res. Solid Earth 123, 10,597-10,615. https://doi.org/10.1029/2018JB015682

Stearns, H.T., MacDonald, G.A., 1947. Geology and Ground-Water Resources of the Island of Hawaii, Geographical Review. https://doi.org/10.2307/211144

Sun, S.S., McDonough, W.F., 1989. Chemical and isotopic systematics of oceanic basalts: Implications for mantle composition and processes. Geol. Soc. Spec. Publ. 42, 313–345. https://doi.org/10.1144/GSL.SP.1989.042.01.19

Swirydezuk, K., Larson, G.P., Smith, G.R., 1981. Volcanic ash stratigraphy of the Glenns Ferry and Chalk Hills Formations, western Snake River Plain, Idaho. Moscow, Idaho.

Taisne, B., Tait, S., 2011. Effect of solidification on a propagating dike. J. Geophys. Res. Solid Earth 116, 1–14. https://doi.org/10.1029/2009JB007058

Tiab, D., Donaldson, E.C., 2016. Chapter 2 - Introduction to Petroleum Geology, in: Tiab,
D., Donaldson, E.C. (Eds.), Petrophysics (Fourth Edition). Gulf Professional Publishing,
Boston, pp. 23–66. https://doi.org/https://doi.org/10.1016/B978-0-12-803188-9.00002-4

Turner, K.J., and 11 others, 2011. Geologic map of Big Bend National Park, Texas. U.S.
Geological Survey Scientific Investigations Map 3142 (scale 1:75,000) and pamphlet.

Valentine, G.A., Graettinger, A.H., Sonder, I., 2014. Explosion depths for phreatomagmatic
eruptions. Geophys. Res. Lett. 41, 3045–3051. https://doi.org/10.1002/2014GL060096

White, J.D.L., 1996. Impure coolants and interaction dynamics of phreatomagmatic
eruptions. J. Volcanol. Geotherm. Res. 74, 155–170. https://doi.org/10.1016/S0377-
0273(96)00061-3

White, C.M., Hart, W.K., Bonnichsen, B., Matthews, D., 2002. Geochemical and Sr-isotopic
variations in western Snake River plain basalts, Idaho. Bull. - Idaho Geol. Surv. 30,
329–342.

White, J.D.L., Smellie, J.L., Clague, D.A., 2003. Introduction: A deductive outline and
topical overview of subaqueous explosive volcanism, in: Geophysical Monograph
Series. pp. 1–23. https://doi.org/10.1029/140GM01

White, J.C., Benker, S.C., Ren, M., Urbanczyk, K.M., Corrick, D.W., 2006. Petrogenesis and
tectonic setting of the peralkaline Pine Canyon caldera, Trans-Pecos Texas, USA. Lithos
91, 74–94. https://doi.org/10.1016/j.lithos.2006.03.015

Wilson, L., Head III, J.W., 1981. Ascent and eruption of Basaltic Magma on the Earth and
Moon. J. Geophys. Res. 86, 2971–3001.
https://doi.org.proxy.library.umkc.edu/10.1029/JB086iB04p02971

Wilson, L., Head III, J.W., 2002. Heat transfer and melting in subglacial basaltic volcanic
eruptions: Implications for volcanic deposit morphology and meltwater volumes. Geol.
Soc. Spec. Publ. 202, 5–26. https://doi.org/10.1144/GSL.SP.2002.202.01.02

Winchester, J.A., Floyd, P.A., 1977. Geochemical discrimination of different magma series
and their differentiation products using immobile elements. Chem. Geol. 20, 325–343.
https://doi.org/10.1016/0009-2541(77)90057-2

Wood, S.H., Clemens, D.M., 2002. "Geologic and Tectonic History of the Western Snake
River Plain, Idaho " by Spencer H. Wood, et al. Idaho Geol. Surv. Bull. 30, 69–103.

Zimanowski, B., Büttner, R., Lorenz, V., Häfele, H.G., 1997. Fragmentation of basaltic melt
in the course of explosive volcanism. J. Geophys. Res. B Solid Earth 102, 803–814.
https://doi.org/10.1029/96jb02935

VITA

Aaron Galletly received his Bachelor of Science in Geology from the University of Missouri – Kansas City in 2017. In May of 2020, Aaron graduated from the University of Missouri – Kansas City with his Master of Science in Environmental and Urban Geosciences. While attending the University of Missouri – Kansas City for his graduate studies, he worked as a Graduate Research Assistant and Graduate Teaching Assistant.

Before completing his bachelor's degree, Aaron served as a field assistant for research conducted in Yarbro, Arkansas and San Salvador, Bahamas in 2016. After graduating with his bachelor's degree, Aaron worked as a full-time associate scientist at an environmental consulting and remediation firm in Kansas City, Missouri for two years before transitioning to part-time while working on his Master's. In 2019, Aaron acquired his Missouri Geologist Registrant In-Training license. Before beginning his Master's, Aaron served as a field assistant for research conducted in Diamond Craters, Oregon. While working on his Master's, Aaron conducted field work for one week in Big Bend National Park, Texas and for one week in 71 Gulch, Idaho. He was also accepted to attend the International Volcanological Field School with the University of Alaska – Fairbanks, but the course has been postponed until 2022 due to COVID-19. Aaron has presented his research at GSA 2020 Connects Online (October 2020) and at the North-Central/South-Central Joint Online Section Meeting (April 2021), as well as a virtual talk for the EES 298 class at Wilkes University (Spring 2021).

Aaron is affiliated with the Geological Society of America (GSA) and the Association of Environmental & Engineering Geologists (AEG).